Subcritical and Supercritical Shear Flows in Shallow Waters - Numerical Simulations and Laboratory Experiments

Tao Wang

Doctor of Philosophy

Department of Civil Engineering and Applied Mechanics

McGill University

Montreal, Canada

June 2015

A thesis submitted to McGill University in partial fulfillment of the requirements of the degree of Doctor of Philosophy

DEDICATION

To My Parents

ACKNOWLEDGEMENTS

I would like to express my most sincere appreciation to my research supervisor, Professor Vincent H. Chu, for his continuous support and encouragement. I started to work with Professor Chu when I was an undergraduate student. His impact on me is not only in research investigations but also in personality formation and career development. His extensive knowledge in science, preciseness and diligence have inspired and encouraged me to move up from one stage to the next in my study and career. I just want to share one of his words to motivate me the most: "Doing research is like running one hundred meters. You need to run 0.1s faster to be the champion. Engineering career is like a rally. You have to foresee and get prepared for the long term."

Special appreciation to my friend and colleague Dr. Shooka K. Ghannadi. We have collaborated on the experiments and computer modeling. I have learned a lot through knowledge sharing with her. I would like to thank her suggestions and comments on the preparation of this thesis.

I would like to thank to Mr. John Bartczak for his help in setting up the experimental apparatus in the hydraulics laboratory, and to thank Dr. Lai Wai Tan for her guidance getting me start on my research.

The love and support of my parents have encouraged me to persuit graduate studies and enable me to complete this doctoral thesis.

ABSTRACT

A series of numerical simulations and laboratory experiments has been conducted to gain understanding of high-speed supercritical shear flows in shallow waters. The study of the supercritical flow is to complement the existing knowledge of the flow in subcritical speed. The basic concept is developed in two chapters of thesis by the analysis of unstable shear flow in the form of jets and/or wakes. The fractional rate of growth and the pattern speed of the shear instabilities are determined from the numerical simulations directly using the shallow-water equations, covering a range of Froude number beyond the range that can be determined by the classical method. The direct numerical simulation has delineated the formation of eddy and eddy-shocklet during the nonlinear transition of the instabilities to turbulence, leading to the classification of subcritical, trans-critical and supercritical instabilities in terms of the Froude number.

The challenge in the simulations of the supercritical flows is the need for the numerical scheme to capture the sudden changes in depth and velocity across the hydraulic jumps. The present simulations were conducted using a fifth-order Weighted Essentially Non-Oscillation (WENO) scheme for spatial interpolation. Time integration was by a fourth-order Runge-Kutta method. The accuracy of the scheme is evaluated by grid refinement study in the chapter following the linear and non-linear stability analysis.

The subcritical and supercritical exchanges of mass and momentum are further studied in the laboratory. Dye as tracer was injected into a square basin on the side of an open channel. The concentration of the dye was measured using a video imaging method. The rate of exchanges was monitored by the change of the dye concentration in the basin and was then correlated with the Froude number. The experiments covered both the subcritical and supercritical turbulent flow over a range of Froude numbers varying from Fr = 0.48 to 2.92.

The last shallow shear flow problem is the calculations for the flow resistance in a straight

and meandering open channel occupied by arrays of blocks. The macro resistance to flow is dependent on turbulence and waves around the blocks. The overall macro roughness coefficient is found to depend not only on the size of the macro roughness but also on the channel slope. A new formulation for the drag coefficient of the flow resistance in steep channels is proposed to replace the traditional correlation using the Manning formula.

RÉSUMÉ

Une série de simulations numériques et dexpériences de laboratoire a été menée pour mieux comprendre les écoulements cisaillés supercritiques é haut débit en eaux peu profondes. L'étude de lécoulement supercritique vient compléter les connaissances actuelles de l'écoulement en régime fluvial.

Le concept de base est développé à travers les deux premiers chapitres de la thèse par l-analyse de flux de cisaillements instables tels que les jets et/ou sillages. Le taux fractionnaire de croissance et le modèle de vitesse des instabilités du flux de cisaillement sont déterminés selon les simulations numériques utilisant directement les équations en eaux peu profondes. Ceci permet de couvrir une gamme de nombres de Froude au delá de la plage qui peut être déterminée par la méthode classique. Les simulations numriques directes ont délimits la formation de remous durant la transition non linaire des instabilités vers le régime torrentiel. Ceci a permis la classification dinstabilités sous critiques, transcritiques et supercritiques en fonction du nombre de Froude.

Le défi lors de simulations sous régime torrentiel est de modéliser les changements brusques de profondeur et de vitesse au travers des ressauts hydrauliques. Les simulations ont été réalisées à laide dun schéma WENO (Weighted Essentially Non Oscillatory) du cinquième ordre pour la discrétisation spatiale. Lintégration temporelle fut faite laide dune méthode de Runge Kutta du quatrième ordre. La précision du schéma fut évaluée par létude du raffinement du maillage tel quexpliqué dans le chapitre suivant lanalyse de stabilité linéaire et non-linéaire.

Les échanges de masse et dénergie cinétique en régime sous-critique et supercritique furent étudiés lors dexpériences en laboratoire. Un colorant servant de traceur a été injecté dans un bassin carré sur le côté dun canal. La concentration du colorant a été mesurée en utilisant un procédé d'imagerie vidéo. Le taux d'échange fut mesuré par la variation de la concentration du colorant dans le bassin, et fut ensuite corrélé avec un nombre de Froude.

Les expériences ont été menées à la fois pour un écoulement fluvial et torrentiel sur une plage de nombres de Froude variant de Fr=0.48 à 2.92.

Le dernier problème concernant les écoulements cisaillés en eaux peu profondes est le calcul de la résistance du flux dans un canal ouvert droit et sinueux occupé par des séries de blocs. La macro résistance à l'écoulement dépend de la turbulence et des vagues autour des blocs. Le coefficient global de macro rugosité se trouve à dépendre non seulement de la taille de la macro rugosité mais également de la pente du canal. Une nouvelle formulation pour le coefficient de perte de charge dans les canaux à pente raide est proposée pour remplacer la corrélation traditionnelle utilisant la formule de Manning.

TABLE OF CONTENTS

LIST OF TABLES

LIST OF FIGURES

LIST OF SYMBOLS

Roman Symbols

a	Meander amplitude
a_i	Calibration coefficient
$\frac{a}{h}$	Aspect ratio of the eddy/shocklet
$\tilde{A}_f$	Frontal area
b	Width of the block obstacles
B	Total width of the channel
c	Dye concentration
c_a	Gravity wave speed
c_m	Gravity wave speed
c_o	Initial dye concentration
c_p	Wave pattern speed
c_{qs}	Quasi-state dye concentration
$\bar{c}$	Mean concentration of the dye
$\bar{c}_{max}$	Maximum mean concentration of the dye
$\sqrt{\overline{c'^2}}$	Root mean square fluctuation of the dye concentration
$\sqrt{\overline{c'^2_{max}}}$	Maximum root mean square fluctuation of the dye
C_D	Instant drag coefficient
$\tilde{C}_D$	Average drag coefficient
Co	Courant number
f_x	Friction resistance force in x direction
f_y	Friction resistance force in y direction
F	Volume fraction of fluid
F_D	Instant drag force

$\tilde{F}_D$	Average drag force
Fr	Froude number
$\mathrm{Fr_c}$	Convective Froude number
$\mathcal{F}^{uuh}$	Linear momentum flux in x direction
$\mathcal{F}^{vvh}$	Linear momentum flux in y direction
$\mathcal{F}^{uvh}$	Non-linear momentum flux in x direction
$\mathcal{F}^{vuh}$	Non-linear momentum flux in y direction
g	Gravity constant
g'	Reduced gravity constant
G	Green light intensity of the dye image inside the basin
G_o	Green light intensity of the background inside the basin
G_c	Green light intensity of the dye image outside the basin
G_{oc}	Green light intensity of the background outside the basin
G_x	Driving force in x direction
G_y	Driving force in y direction
h	Water depth
h'	Depth fluctuation
h_o	Upstream depth
h_d	Downstream depth
h_{front}	Depth in front of the block
h_{back}	Depth behind the block
h_s	Depth at the location of hydraulic jump
H	Mean water depth
i	Counter in x direction
j	Counter in y direction
k	Wave number
k_x	Wave number in x-direction

k_{ya}	Wave number in y-direction
K'	Disturbance kinetic energy
ell_s	Length scale associated with SECH profile
L	Length(Width) of the basin
L_s	Length of the sinusoid
Lx	Length of the computational domain in x direction
Ly	Length of the computational domain in y direction
Ma	Mach number
$\mathrm{Ma_c}$	Convective Mach number
N	Number of images or number of grid points
n_{bed}	Manning friction coefficient
n_{macro}	Macro roughness coefficient
p	Percentage of green light reduction
P_k	Order of convergence
q_o	Dye injection rate
q_x	Flow discharge per unit width in x direction
q_y	Flow discharge per unit width in y direction
Q_{qs}	Quasi-state discharge
Q	Total discharge in the system
$\sqrt{\overline{Q'^2}}$	Root mean square fluctuation of the discharge
$\mathcal{R}$	Rate function
S	Stencils
S_o	Channel bottom slope
t	Time
TE	Total energy
u	Flow velocity in x direction
u'	x-velocity fluctuation
U	Mean channel velocity

U_m	Maximum velocity of SECH profile
U_a	Ambient velocity of SECH profile
$\hat{U}_y$	Maximum of the velocity gradient at the inflection point
v	Flow velocity in y direction
v'	y-velocity fluctuation
$\tilde{V}$	Frontal velocity
x	Longitudinal coordinate
y	Lateral coordinate
y_{mean}	Position for half of the maximum mean concentraion
y^+_{rms}	Positive position for half of the maximum root mean square fluctuation of the dye
y^-_{rms}	Negative position for half of the maximum root mean square fluctuation of the dye

Greek Symbols

α	Linear growth rate of the instability
δ	Half width
δ_ω	Vorticity thickness
Δ_o	Jet/wake initial velocity difference
Δt	Time increment
Δx	Grid size in x direction
Δy	Grid size in y direction
Δz	Grid size in vertical direction
$\bar{\Delta}$	Velocity of the equivalent top-hat profile
Γ	Velocity ratio
λ	Wavelength of the channel
λ_x	Wave length in x-direction
λ_{ya}	Wave length in y-direction
μ_1	First moment

μ_2 Second moment

$\bar{\mu}$ Width of the equivalent top-hat profile

ω Wave frequency

ϕ Any variable

ρ Fluid density

τ_a Dye accumulation time

τ_r Dye retention time

θ Wave angle

ζ' Vorticity fluctuation

Superscripts

^{n} Variable at a particular time

$\hat{}$ Interpolated variable/maximum value

* Dimensionless variable

Subscripts

$_c$ The center cell variable value

$_d$ The first downstream cell variable value

$_{dd}$ The second downstream cell variable value

$_u$ The first upstream cell variable value

$_{uu}$ The second upstream cell variable value

$_R$ R event

$_{R'}$ R' event

$_S$ S event

CHAPTER 1

INTRODUCTION

1.1 Preface

The studies of shear instability and turbulence in shallow flows are fundamental to the understanding of exchange processes of shallow flows in the atmosphere, oceans and coastal waters. The depth of these flows is considered to be shallow in comparison with the large horizontal extent of the circulations (Jirka (1994), Chu (2002)). The state of shallow flow is dependent on whether the speed of flow is greater or smaller than the speed of the gravity wave, $\sqrt{gH}$. The dimensionless parameter for relative measure of the speed is the Froude number

$$\mathrm{Fr} = \frac{U}{\sqrt{gH}} \tag{1.1}$$

where g is the gravitational acceleration; U and H are the speed and the depth of the flow. The flow is in a subcritical state when the flow speed is smaller than the wave speed, that is when Froude number $\mathrm{Fr} < 1$, and is in a supercritical state if Froude number $\mathrm{Fr} > 1$. High speed flow in a steep channel is supercritical. Density current of moderate speed also can be supercritical when the speed of the gravity wave is reduced with the reduced gravity. The speed of the internal wave that defines the state of the density current, is equal to $\sqrt{g'H}$, which is a small speed as the reduced gravity $g' = g\Delta\rho/\rho$ is proportional to a small density difference $\Delta\rho$ associated with the density current.

Most of the existing work in shallow-flow turbulence is developed for sub-critical flow (see e.g. Rodi (1993). However, significant transport processes in the atmosphere, oceans and coastal waters often occur in trans-critical and the supercritical states. Sands, gravels and rocks are transported down to the river channel by the supercritical flow during the

flood stage. The transport in density currents is decided in the trans-critical state when the flow changes from subcritical to supercritical state across the shock waves in the form of internal hydraulic jump.

1.2 Thesis Organization

The thesis is based on manuscripts and contains eight chapters. Chapter 1 includes a brief summary of the research problems, literature review, objective and scope of the study. Chapter 2 provides the summary of the governing equations and numerical method. It provides the details of using minimum intervention strategy and WENO interpolation to control numerical oscillations. Chapter 3 studies jet and wake instability problem and presents the results in the linear stage. It points out the existence of the sinuous and varicose mode and the transition between the two modes. The linear growth rate correlates with the convective Froude number for both full jet/wake and half jet/wake. Chapter 4 continues the jet and wake instability calculation into the non-linear stage. This chapter gives a full picture of the development of the instability. The results at time of the maximum rate of change in turbulent kinetic energy and saturation point are presented. Chapter 5 shows the results of convergency study. The degree of accuracy for the direct numerical simulation is given. Chapter 6 is the laboratory study of mass exchange between the main channel and its side basin. Six experiments are conducted focusing for supercritical flow experiments. The Froude number could reach 2.92. Chapter 7 is another application example of study the roughness of a steep open channel and a meandering channel. This chapter indicates the value of Manning friction coefficient may not be a good parameter to describe the total roughness of the channel. The macro roughness coefficient is the overall parameter related to the flow resistance and could be calculated by numerical simulation. Chapter 8 summarizes the conclusions and the contribution of the thesis.

The thesis essentially is a collection of manuscripts and papers prepared by the author. The list of the manuscripts and papers and their relation to chapters in the thesis are as

follows:

Chapter 3:

1. Wang, T., Chu, V.H. Instabilities of Jet and Wake Flow in Shallow Waters at High Froude Number. *Physics of Fluid*, draft for submission, 2015.

Chapter 4:

2. Wang, T., Chu, V.H. Non-linear Transition of Jet/Wake Instability in Shallow Flows. *Physics of Fluid*, draft for submission, 2015.

Chapter 5:

3. Wang, T., Chu, V.H. Instabilities and Nonlinear Transition of High-speed Shear Flow in Shallow Waters. *Proceedings of the 8th International Conference on Computational Fluid Dynamics, Chengdu, Sichuan, China,* 2014.

Chapter 6:

4. Wang, T., Ghannadi, S.K., Chu, V.H. Experimental Study of the Exchange Process Between the Main Flow and its Side Basin. *Proceedings of the 7th International Symposium on Environmental Hydraulics, Singapore, Singapore.* 2014.

5. Wang, T., Ghannadi, S.K., Chu, V.H. Retention of Dye Tracer in Side Basins Exchanging with Subcritical and Supercritical Flows. *Proceedings of the International Conference on Fluvial Hydraulics, River Flow 2010 (ISBN 978-3-939-230-00-7), Volume 2, Braunschweig, Germany, Page 1775-1782.* 2010.

Chapter 7:

6. Wang, T., Chu, V.H. Manning Friction in Steep Open-Channel Flow. *Proceedings of the 7th International Conference on Computational Fluid Dynamics, Big Island, Hawaii, USA.* 2012.

7. Wang, T., Chu, V.H. Macro Resistance to Flow on Steep Channel. *Proceedings of the 3rd International Symposium on Shallow Flows, Iowa City, Iowa, USA*. 2012.

8. Wang, T., Tan, L.W., Chu, V.H. Flood-Waves Simulation by Classical Method of Consistent Transport. *Proceedings of the 6th International Conference on Computational*

Fluid Dynamics (ISBN:978-3-642-17883-2), St. Petersburg, Russia, Page 287-293. 2010.

1.3 Contribution of Authors

The manuscripts of the papers included in this thesis are my original work. The laboratory experiments shown in Chapter 6 are the work in collaboration with Dr. Shooka K. Ghannadi. Professor Vincent H. Chu has supervised the entire research. He has provided guidance and direction of the research and edited all the manuscripts.

1.4 Objective and Scope

The challenge in laboratory and numerical investigations of trans-critical and supercritical flows is the management of waves, and the parameterization for the wave effect. The numerical simulation of the flow has to rely on stable and accurate numerical schemes to capture the depth and velocity discontinuities across the shock waves.

This thesis is to focus on the wave effect on trans-critical and supercritical flow. The basic concept is developed in two chapters of the thesis by the analysis of unstable shear flow in the form of jets and/or wakes. The fractional rate of growth and the pattern speed of the shear instabilities are determined from the numerical simulations directly using the shallow-water equations, covering a range of Froude number beyond the range that can be determined by the classical method of the normal mode approach. The direct numerical simulations delineate the formation of eddy and eddy-shocklet during the nonlinear transition of the instabilities to turbulence, leading to the classification of subcritical, trans-critical and supercritical instabilities in terms of the Froude number. The numerical simulations capture the sudden changes in depth and velocity across the hydraulic jumps using a fifth-order Weighted Essentially Non-Oscillation (WENO) scheme for spatial interpolation. A fourth-order Runge-Kutta method is used for time integration. The accuracy of the scheme is evaluated by grid refinement study in the chapter following the linear and non-linear stability analysis.

The wave effect on subcritical and supercritical flows are also studied in the laboratory. The exchanges of mass and momentum between a side basin and the main flow in an open channel are determined in the laboratory by measuring the dye concentration using a video imaging method.

1.5 Literature Review

The relevant literature related to the present study of the wave effect on shallow-flow turbulence includes three parts: (i) the parameterization of the problem in the study of the stability and its transition to turbulence, (ii) the numerical scheme developed for the solution of the shallow water equations, and (iii) the laboratory experiments to measure the exchanges of mass and momentum in subcritical and supercritical flows.

1.5.1 Parameterization of the Wave Effect

Waves play a central role in the development of a theory of trans-critical and supercritical flow. The pioneering work was due to Lin (1953). He suggested the use of Mach number based on a relative velocity to parameterize for the effect in studying the analogous problem in gas dynamic. This relative-velocity Mach number was subsequently referred to as the convective Mach number and used by Boganoff (1983), Papamoschou & Roshko (1998), Sandham & Reynolds (1990), Vreman et al. (1996) and others to characterize the wave effect on the instability and turbulence. The equivalent dimensionless parameter for the analogous effect in shallow water is the convective Froude number (Pinilla & Chu (2008), Chu (2010), Chu (2014)). Almost all previous studies of the effect were for the problem of the mixing layer which happened to be a special case. The problem of the wave effects for the general flow including the jet-and-wake like flow is to be considered in this thesis for a correct parameterization of the wave effects that is based on a pattern velocity c_p and the generalized convective Froude number as follows:

$$\mathrm{Fr_c} = \frac{c_p - U_a}{c} \tag{1.2}$$

where $c = \sqrt{gH}$ is the gravity-wave speed and U_a is the ambient velocity in the free stream. The wave speed is the speed of the sound and the dimensionless number is the convective Mach number $\mathrm{Ma_c}$ for the analogous problem in gas dynamic. For the mixing layer, $c_p = (U_1 + U_2)/2$, $U_a = U_2$, hence the expression $\mathrm{Fr_c} = (U_1 - U_2)/\sqrt{gH}$ or $\mathrm{Ma_c} = (U_1 - U_2)/c$ is used in most existing works. We shall see that the velocity difference across the mixing layer, $(U_1 - U_2)$, is not necessary to be the correct velocity scale for the wave effect when more general problems such as the jets and the wakes are examined in subsequent chapters in this thesis.

1.5.2 Shock Capturing Numerical Schemes

Various shock capturing schemes have been developed for the solutions of the shallow water equations and the similar equations for the analogous problem in gas dynamics. Early numerical methods were developed for the hyperbolic equations. Exact and approximate solutions were often based on the method of characteristics. These include the works of Stoker (1957), Carrier and Greenspan (1958), Shen and Meyer (1963), Henderson (1966) and Wu (2005). The method of characteristics also has been used to solve the shallow water equations. The most popular such numerical method is the Riemann solver. The subsequent solvers developed to solve the Riemann problem include Godunov (2008), Roe (1981), van Leer (1979), LeVeque (2002) and Toro (1999). These solvers are effective in capturing the discontinuities across shock waves. However, using the classical method of finite volume could obtain equally accurate and stable results in capturing the shock waves. The key to apply the classical finite volume method is to compute the fluxes by different schemes. The schemes have to incorporate flux limiters by adjusting the face values to ensure numerical stability. The flux limiters are described in the works of Dick (2009), Stelling and Duinmeijer (2003), Guinot (2003), Dodd (1998), and Leonard (1988, 1979). The recent development of the minimal intervention strategy (MIS) by Pinilla et al. (2010) is employed to manage the numerical oscillations in the classical finite volume (CFV) to obtain numerical solution of the

shallow water equations. Only the missing variables on the face are needed for flux limiting and such intervention has to be minimal to ensure interpolation accuracy. Jiang and Shu (1996), Shu (1998),and Shu (2009) have introduced the weighted essentially non-oscillatory (WENO) scheme for interpolation for higher-order accuracy and stability. The numerical methods to solve the shallow water equations using the WENO scheme are given in Chapter 2 of this thesis.

1.5.3 Jet and Wake Instability

Most of the previous works on wave effect were developed from the study of shear flow with a hyperbolic-tangent (TANH) profile. These include the study of the analogous problem in gas dynamics by Sandham and Reynolds (1990) and the more recent work by Ghannadi (2015). The classical approach to solve the instability problem is to use the normal mode approach. The instability of the flow is determined from the eigenvalues of the linearized equations. Instability analysis of the shear flow included the work of Michalke (1964) and Sandham and Reynolds (1990). Betchov and Criminale (1966) had studied the profile of jet and wake and derived the growth rate at the limiting case when $\mathrm{Fr_c} = 0$ by the normal mode approach. Lessen, Fox and Zien (1965) studied the instability of inviscid compressible jets and wakes and found that these flows are more unstable as the wave-propagation angle relative to the main flow became larger. Freund et al. (2000) simulated a perfectly expanded turbulent jet at Mach number 1.92. Ray et al. (2009) computed phase velocities and linear instability of compressible asymmetric jets at different Mach numbers and found good correlation to the experiments. In the cases of high Mach numbers, the instability problem is always associated with the generation of gravity waves. The work included Mack (1990), Lee et al.(1991), Vreman et al. (1996), Avital et al. (1998), Balmforth (1999), Ghidaoui and Kolyshkin (1999), Kolyshkin and Ghidaoui (2002). Tachie and Balachandar (2000) studied shallow wakes on smooth and rough surfaces in a laboratory. They measured the mean velocity profile, velocity fluctuation and half width of the wake

at small Froude number. Peltier et al. (2014) conducted experimental study of the shallow meandering jet and found the relation of the shape factor and Froude number. Chen et al. (1990) performed three-dimensional simulations and found the stability curve for a range of Mach numbers. Chen et al (1990) concluded the effect of varying the relative phase difference between a fundamental instability mode and its subharmonic controlled the evolution of a wake. The numerical simulation had indicated the reduction in wake growth rate at high Mach numbers. The influence of increasing Mach number is stabilizing, resulting in reduced growth rates for both antisymmetric and symmetric modes of the wake. Chu et al. (1991) had computed the flow with a SECH velocity profile with two modes of oscillation, the sinuous mode and the varicose mode for antisymmetrical and symmetrical disturbances, respectively. The stability characteristics for these two modes were investigated and correlated with bed friction.

1.5.4 Experiment on Exchange Between the Main Channel and Side Basin

The early experimental studies focusing on the flow exchange with surroundings were done in the area of gas dynamics. Rossiter (1964) conducted wind tunnel experiments on the flow over cavities for Mach Number (Ma) from 0.4 to 1.2. East (1966) conducted rectangular cavity experiment to find frequency of the flow oscillations. Tam and Block (1978) proposed the process of cavity oscillations for acoustic feedback and normal-mode resonance for Mach number from 0.05 to 0.4. Forestier et al.(2003) extended the study to high-subsonic speed at Ma = 0.8. The transverse exchanges of mass across the subcritical shear flows in rivers are relatively well understood. Many previous experimental investigations have been conducted. Almost all the experiments are performed at the subcritical state for Froude number below 0.5. The studies of the subcritical flow exchanges include the works of Alavian and Chu (1985), Tamai et al. (1986), Booij (1989), Knight and Shiono (1990), Babarutsi and Chu (1991), Lambert and Sellin (1996), Altai and Chu (1997), Uijttewaal and Booij (2000) and van Prooijen et al.(2005). Alavian and Chu (1985) used a mixing-length approach to conclude

the importance of mixing layer width in the momentum exchange. Tamai et al. (1986) studied and visualized the existance of eddies in the shear layer at the interface between the main channel and the floodplain. Booij (1989) and Altai and Chu (1997) showed the basin concentration followed a first-order decaying equation from experimental observation. Knight and Shiono (1990) added the effect of channel bottom slope in their study. Babarutsi and Chu (1991) studied the confinement and friction effect. Lambert and Sellin (1996) also used the mixing-length approach but corresponded the water depth to the exchange. Uijttewaal and Booij (2000) showed the development of the turbulent mixing layers was affected by the shallowness of the flow and the growth rate of the mixing-layer width decreased with the channel bottom friction. Van Prooijen et al. (2005) concluded the momentum exchange was dominated by the horizontal coherent structures and the bottom turbulence but secondary circulation played a minor role. The most recent experimental work uses particle image velocimetry (PIV) and particle tracking velocimetry (PTV) to measure the velocity field in two or three dimensions. Those work includes Uijttewaal et al. (2001), Weitbrecht et al.(2002, 2008), McCoy et al.(2007) and Constantinescu et al.(2009).

CHAPTER 2

NUMERICAL METHOD

Direct numerical simulations are performed to study the jet and wake instability problem and macro roughness problem. Since supercritical flows are always associated with wave generation and radiation, a wave capturing scheme is needed to capture the shock waves. The challenges in numerical modeling have been in the capturing of the shock-wave front where the flow changes from supercritical to subcritical and in the advancing front where water hits the boundaries or obstacles. Computations may collapse as a consequence of numerical instability when the depth of water becomes negative at these fronts. The artificial numerical oscillations have to be suppressed for long-term computational stability. A stable and robust hydrodynamic routing model would be needed to determine the water depth and velocity. This chapter will explain how to resolve the governing equations, the Shallow Water Equations(SWE) in two dimensional space.

2.1 Shallow Water Equations

Shallow Water Equations are a simplified form of the full Navier-Stokes equations in incompressible flows. The equations apply in the situations for whih the horizontal length scale is much larger than the vertical length scale. Therefore, the vertical velocity component is negligible in the calculation. The x and y components of the velocity are represented by their depth average values. The general form of the shallow water equations are:
continuity equation:

$$\frac{\partial h}{\partial t} + \frac{\partial q_x}{\partial x} + \frac{\partial q_y}{\partial y} = 0 \tag{2.1}$$

x-momentum equation:

$$\frac{\partial q_x}{\partial t} + \frac{\partial}{\partial x}\left(\frac{q_x^2}{h}\right) + \frac{\partial}{\partial y}\left(\frac{q_x q_y}{h}\right) = -\frac{1}{2}g\frac{\partial h^2}{\partial x} - f_x + G_x \tag{2.2}$$

y-momentum equation:

$$\frac{\partial q_y}{\partial t} + \frac{\partial}{\partial x}\left(\frac{q_x q_y}{h}\right) + \frac{\partial}{\partial y}\left(\frac{q_y^2}{h}\right) = -\frac{1}{2}g\frac{\partial h^2}{\partial y} - f_y + G_y \tag{2.3}$$

where h = depth, g = gravitational acceleration, q_x, q_y = x- and y-component of flow rate per unit width. f_x, f_y = channel bottom friction forces. G_x, G_y= driving forces. $\frac{\partial}{\partial x}\left(\frac{q_x^2}{h}\right)$ in the x-momentum equation and $\frac{\partial}{\partial y}\left(\frac{q_y^2}{h}\right)$ in the y-momentum equation refer as the linear term. $\frac{\partial}{\partial y}\left(\frac{q_x q_y}{h}\right)$ in the x-momentum equation and $\frac{\partial}{\partial x}\left(\frac{q_x q_y}{h}\right)$ in the y-momentum equation refer as the nonlinear advection term. The momentum fluxes are defined as the following and will be calculated to balance the mass in each control volume.

$$\frac{q_x^2}{h} = \mathcal{F}^{uuh}, \quad \frac{q_y^2}{h} = \mathcal{F}^{vvh}, \quad \frac{q_x q_y}{h} = \mathcal{F}^{uvh}, \quad \frac{q_y q_x}{h} = \mathcal{F}^{vuh} \tag{2.4}$$

2.2 Shallow Water Equations Discretization

The SWE are solved by the finite volume(FV) method. The computational domain is divided into a number of square computational meshes as shown in Figure 2–1. The center of each control volume defines the nodal value of the water depth as shown in open circle. The arrows in the figure represent the flow entering and leaving the control volume. The flux of each control volume is calculated by tracking the change of mass and momentum. The mesh is staggered meaning the control volumes for the water depth, the x and y components of the velocity are not defined at the same place as demonstrated in Figure 2–2. The meshes of $u_{(i,j)}$ and $v_{(i,j)}$ are one half position in front of the mesh of $h_{(i,j)}$ in the direction of the flow.

The discretization of the shallow water equations is required to obtain the solutions by direct numerical method. The control volume of the continuity equation is shown in Figure

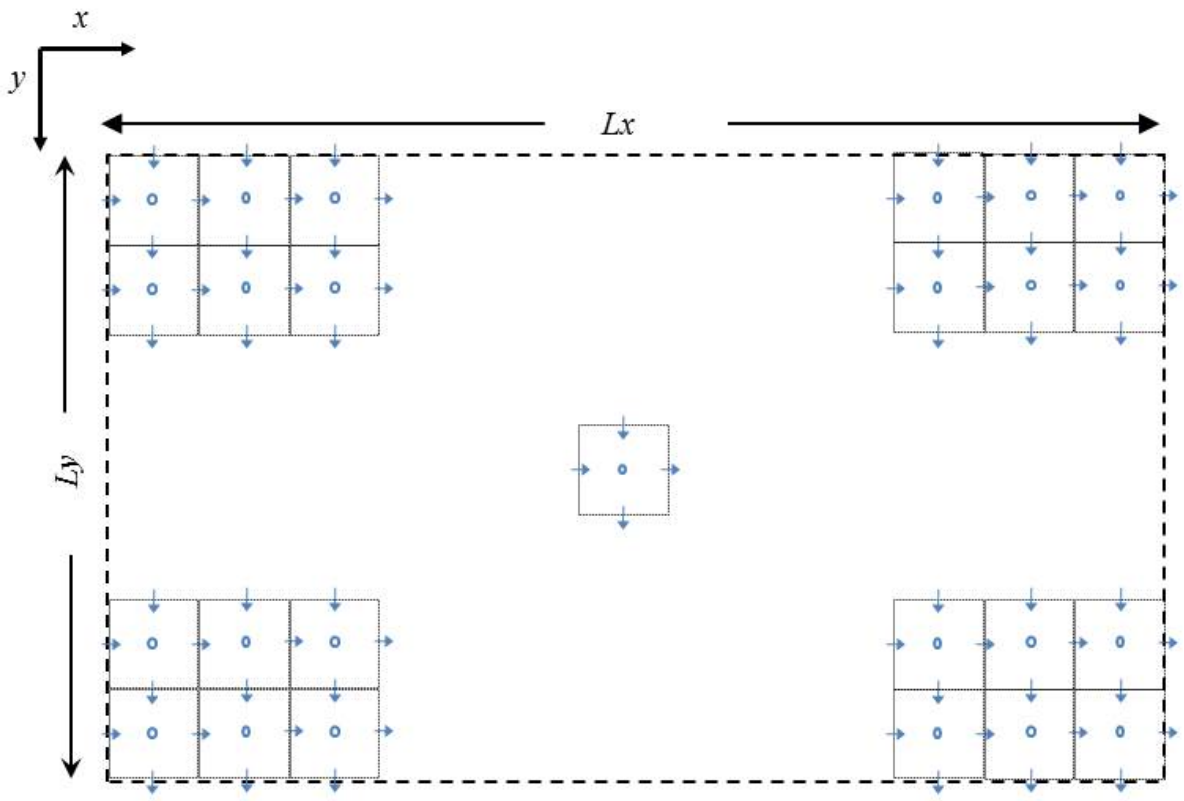

Figure 2–1: Discretize of computation domain into control volumes

2–3 and the continuity equation is discretized as

$$\frac{h_{i,j}^{n+1} - h_{i,j}^{n}}{\Delta t} + \frac{(q_x)_{i+1,j}^{n} - (q_x)_{i,j}^{n}}{\Delta x} + \frac{(q_y)_{i,j+1}^{n} - (q_y)_{i,j}^{n}}{\Delta y} = 0 \tag{2.5}$$

The superscript ^{n} represents a variable value at time t and $^{n+1}$ is the same variable value after Δt second.

The control volume of the flow per unit width in x direction q_x is shown in Figure 2–4. Using the momentum fluxes $\mathcal{F}^{uuh}$ and $\mathcal{F}^{uvh}$, the x-momentum equation can be discretized as

$$\frac{(q_x)_{i,j}^{n+1} - (q_x)_{i,j}^{n}}{\Delta t} + \frac{\mathcal{F}_{i+\frac{1}{2},j}^{uuh} - \mathcal{F}_{i-\frac{1}{2},j}^{uuh}}{\Delta x} + \frac{\mathcal{F}_{i,j+\frac{1}{2}}^{uvh} - \mathcal{F}_{i,j-\frac{1}{2}}^{uvh}}{\Delta y} = -g\frac{h_{i,j}^{n} - h_{i-1,j}^{n}}{\Delta x} - f_x + G_x \tag{2.6}$$

Similarly, The control volume of flow per unit width in y direction q_y is shown in Figure 2–5. Using the momentum fluxes $\mathcal{F}^{vvh}$ and $\mathcal{F}^{vuh}$, the y-momentum equation is discretized to

$$\frac{(q_y)_{i,j}^{n+1} - (q_y)_{i,j}^{n}}{\Delta t} + \frac{\mathcal{F}_{i,j+\frac{1}{2}}^{vvh} - \mathcal{F}_{i,j-\frac{1}{2}}^{vvh}}{\Delta y} + \frac{\mathcal{F}_{i+\frac{1}{2},j}^{vuh} - \mathcal{F}_{i-\frac{1}{2},j}^{vuh}}{\Delta x} = -g\frac{h_{i,j}^{n} - h_{i,j-1}^{n}}{\Delta y} - f_y + G_y \tag{2.7}$$

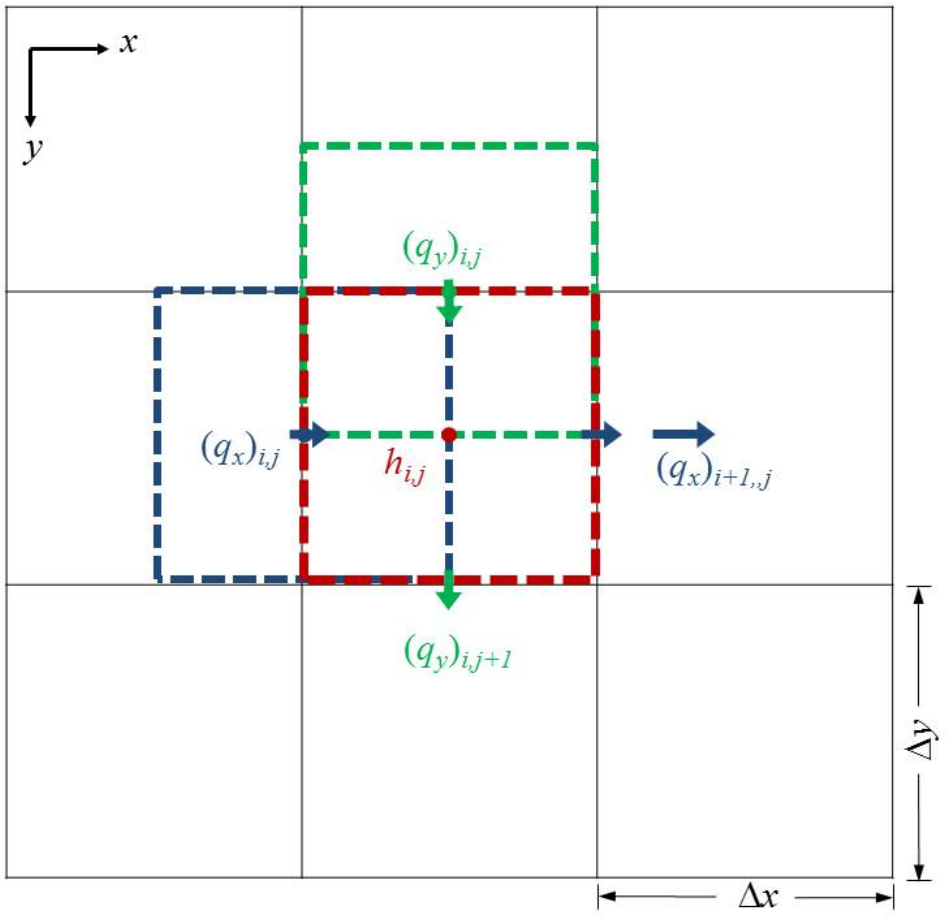

Figure 2–2: Staggered grid showing the positions of $h_{(i,j)}$, $(q_x)_{(i,j)}$ and $(q_y)_{(i,j)}$

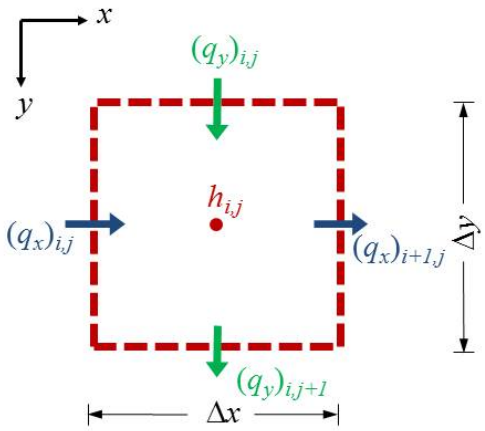

Figure 2–3: Control volume for continuity equation

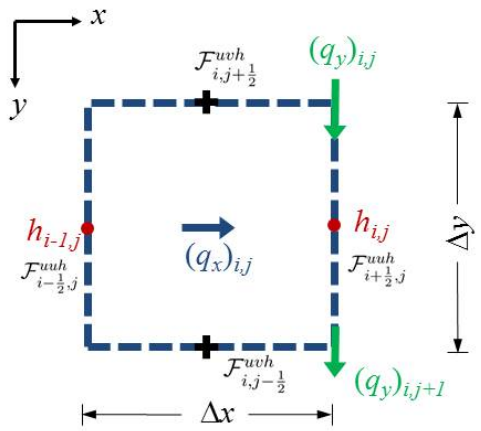

Figure 2–4: Control volume for x-momentum equation

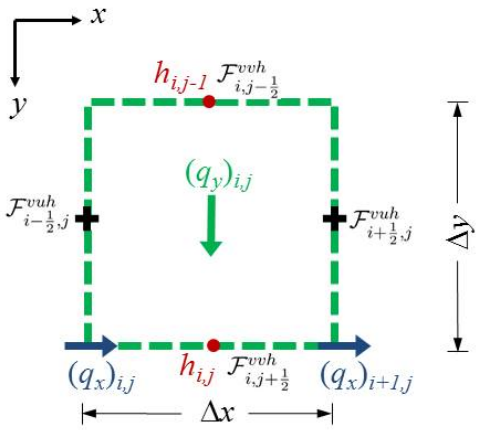

Figure 2–5: Control volume for y-momentum equation

2.3 4^{th} Order Runge-Kutta for Time Integration

The fourth-order Runge-Kutta explicit method is employed for the time integration. Knowing a variable value ϕ^n at the previous time $t = n$, four iterations are performed first to find the intermediate variable value in each iteration.

$$\begin{aligned}
\phi^{1st} &= \mathcal{R}(\phi^n)\Delta t \\
\phi^{2nd} &= \mathcal{R}(\phi^n + \frac{1}{2}\phi^{1st})\Delta t \\
\phi^{3rd} &= \mathcal{R}(\phi^n + \frac{1}{2}\phi^{2nd})\Delta t \\
\phi^{4th} &= \mathcal{R}(\phi^n + \phi^{3rd})\Delta t
\end{aligned}$$

Finally, the variable value for the next time step ϕ^{n+1} is determined by the formula below.

$$\phi^{n+1} = \phi^n + \frac{1}{6}(\phi^{1st} + 2\phi^{2nd} + 2\phi^{3rd} + \phi^{4th}) \tag{2.8}$$

The Runge-Kutta method updates variables h, q_x, and q_y with time. In shallow water equations, the rate functions $\mathcal{R}(\phi) = (\mathcal{R}_h,\ \mathcal{R}_{q_x},\ \mathcal{R}_{q_y})$ are determined by expressing the continuity and momentum equations in the finite difference form as the following:

$$\begin{aligned}
\mathcal{R}_h &= \frac{\Delta h_{i,j}}{\Delta t} = -\frac{(q_x)_{i+1,j} - (q_x)_{i,j}}{\Delta x} - \frac{(q_y)_{i,j+1} - (q_y)_{i,j}}{\Delta y}, \\
\mathcal{R}_{q_x} &= \frac{\Delta (q_x)_{i,j}}{\Delta t} = -\frac{\mathcal{F}^{uuh}_{i+\frac{1}{2},j} - \mathcal{F}^{uuh}_{i-\frac{1}{2},j}}{\Delta x} - \frac{\mathcal{F}^{uvh}_{i,j+\frac{1}{2}} - \mathcal{F}^{uvh}_{i,j-\frac{1}{2}}}{\Delta y} + (f_x)_{i,j} - (G_x)_{i,j}, \\
\mathcal{R}_{q_y} &= \frac{\Delta (q_y)_{i,j}}{\Delta t} = -\frac{\mathcal{F}^{vuh}_{i+\frac{1}{2},j} - \mathcal{F}^{vuh}_{i-\frac{1}{2},j}}{\Delta x} - \frac{\mathcal{F}^{vvh}_{i,j+\frac{1}{2}} - \mathcal{F}^{vvh}_{i,j-\frac{1}{2}}}{\Delta y} + (f_y)_{i,j} - (G_y)_{i,j}.
\end{aligned}$$

2.4 Minimum Intervention to Control Numerical Ocsilations

The fluxes defined in the momentum equations are defined at the faces of q_x and q_y control volumes. Therefore, interpolation is required to estimate the fluxes by the nodal values of q_x and q_y. The interpolation scheme has to converge to certain accuracy as well as maintain numerical stability. The quadratic upstream interpolation for convective kinematics (QUICK) by Leonard (1980) is used for the initial estimation of the face value ϕ_f by using three adjacent nodal values. The three nodal values are denoted as the upstream node ϕ_U, the central node ϕ_C and the downstream node ϕ_D. The QUICK interpolation formula is

$$\phi_f = -\frac{1}{8}\phi_U + \frac{3}{4}\phi_C + \frac{3}{8}\phi_D \tag{2.9}$$

The QUICK scheme is third-order accurate. However, it is oscillatory by producing numerical oscillations where instability occurs. The flux limiter is required to maintain long term computational stability. The flux limiter is implemented in the computational scheme to adjust the face values without affecting the overall mass and momentum conservations. But it affects the accuracy of the interpolation at the discontinuities by locally switching from a

third-order scheme to a first order or second-order scheme. Therefore, the adjustment should be made minimum when intervention is absolutely needed (Bouhairie and Chu (2009)). Flux limiter is applied only to q_x as q_x is updated using the x-momentum equation, and only to q_y as q_y is updated using the y-momentum equation. The initial estimation of the face value ϕ_f is computed first using the base scheme. Then, an auxiliary variable named the downwind weighting factor (DWF) is computed by the formula below:

$$\mathrm{DWF} = \frac{\phi_\mathrm{f} - \phi_\mathrm{D}}{\phi_\mathrm{D} - \phi_\mathrm{C}} \tag{2.10}$$

Leonard and Mokhtari (1990) introduced the normalized variable, $\tilde{\phi}$ as

$$\tilde{\phi} = \frac{\phi - \phi_U}{\phi_D - \phi_U} \tag{2.11}$$

The estimation is monotonic if the value of the normalized variable is between 0 and 1. Another normalized variable θ is defined as the following and the DWF formula in monotonic and non-monotonic regions for different flux limiters are presented in Table 2–1.

$$\theta = \frac{\tilde{\phi}_C}{(1 - \tilde{\phi}_C)} \tag{2.12}$$

Finally, the face value ϕ_f is recomputed by Equation 2.13 using the new DWF value.

$$\hat{\phi} = \mathrm{DWF}\phi_D + (1 - \mathrm{DWF})\phi_C \tag{2.13}$$

2.5 WENO Scheme to Control Numerical Oscillations

The minimum intervention strategy shown in the previous section involves flux limiter to control numerical oscillations. The method lowers the order of interpolation accuracy to the first in the location of discontinuity. This method works generally well in the application problems such as flow across the mountains stream. In certain theoretical problems such as simulation of turbulent mixing layer and acoustic waves, the solution requires higher orders of accuracy at the discontinuities therefore a higher order interpolation scheme is needed.

Table 2–1: DWF formula in monotonic and non-monotonic regions

Discretization scheme	$\tilde{\phi}_C < 0$ non-monotonic	$0 < \tilde{\phi}_C < 1$ monotonic	$\tilde{\phi}_C > 1$ non-monotonic
QUICK		$0.375 + 0.125\theta$	
van Leer	0	$\tilde{\theta}_C$	0
MinMod	0	$\min(0.5\theta,\ 0.5)$	0
MUSCL	0	$\min(\theta,\ 0.25 + 0.25\theta,\ 1)$	0
UMIST	0	$\min(\theta,\ 0.375 + 0.125\theta,\ 1)$	0
SMART	0	$\min(2\theta,\ 0.375 + 0.125\theta,\ 1)$	0
Superbee	0	$\max[\min(\theta,\ 0.5),\ \min(0.5\theta,\ 1)]$	0
ULTRA-QUICK I	0.5θ	$\min[(\frac{1}{\mathrm{Co}} - 1)\theta,\ 0.375 + 0.125\theta,\ 1]$	0.5
ULTRA-QUICK II	0	$\min[(\frac{1}{\mathrm{Co}} - 1)\theta,\ 0.375 + 0.125\theta,\ 1]$	0

Harten et al. (1987) had developed the Essentially Non-Oscillatory (ENO) scheme to obtain piecewise-smooth solutions at discontinuities by a nonlinear adaptive procedure. Based on the ENO scheme, Jiang and Shu (1996), Shu (1998) ,and Shu (2009) had further developed the Weighted Essentially Non-Oscillatory (WENO) scheme. The WENO scheme uses five points to perform interpolation and it is fifth-order of accuracy in general. At regions where rapid change in depth and velocity occur, the WENO scheme reduces to third-order to manage the spurious numerical oscillations that are initiated at the discontinuities. As explained in Shu (2009), the procedure of WENO interpolation to find the face value ϕ_f involves five nodal values in a stencil shown in Figure 2–6. The two cell values upstream are ϕ_{uu} and ϕ_u and the three cell values downstream are denoted as ϕ_c, ϕ_d, and ϕ_{dd}. The face value ϕ_f is estimated by a linear combination of the three third-order interpolations after dividing these five points into three stencils. The interpolation formulations for the stencils are:

$$\phi_{1f} = \frac{1}{3}\phi_{uu} - \frac{7}{6}\phi_u + \frac{11}{6}\phi_c \tag{2.14}$$

$$\phi_{2f} = -\frac{1}{6}\phi_u + \frac{5}{6}\phi_c + \frac{1}{3}\phi_d \tag{2.15}$$

$$\phi_{3f} = \frac{1}{3}\phi_c + \frac{5}{6}\phi_d - \frac{1}{6}\phi_{dd} \tag{2.16}$$

ϕ_{1f}, ϕ_{2f}, and ϕ_{3f} are third-order approximations. The final approximation of ϕ_f is the convex combination of the three third-order approximations by introducing the weight factors, γ_j:

$$\phi_f = \gamma_1\phi_{1f} + \gamma_2\phi_{2f} + \gamma_3\phi_{3f} \tag{2.17}$$

The combination would be fifth-order accurate if the weighting factors are

$$\gamma_1 = \frac{1}{10}, \gamma_2 = \frac{3}{5}, \text{ and } \gamma_3 = \frac{3}{10} \tag{2.18}$$

The face value ϕ_f now becomes

$$\phi_f = \frac{1}{30}\phi_{uu} - \frac{13}{60}\phi_u + \frac{47}{60}\phi_c + \frac{9}{20}\phi_d - \frac{1}{20}\phi_d \tag{2.19}$$

The essentially non-oscillatory solution of the WENO interpolation is to choose the nonlinear weight function ω_j and let

$$\phi_f = \omega_1\phi_{1f} + \omega_2\phi_{2f} + \omega_3\phi_{3f} \tag{2.20}$$

The selection of ω_j has to ensure the smoothness of the function in the stencils. If the function ϕ is smooth in the entire region, then $\omega_j \simeq \gamma_j$. If ϕ has a discontinuity in the stencil S_j, then $\omega_j \simeq 0$. The choice of ω_k depends on the smoothness factors β_j. ω_k is then calculated by:

$$\beta_1 = \frac{13}{12}(\phi_{uu} - 2\phi_u + \phi_c)^2 + \frac{1}{4}(\phi_{uu} - 4\phi_u + 3\phi_c)^2 \tag{2.21}$$

$$\beta_2 = \frac{13}{12}(\phi_u - 2\phi_c + \phi_d)^2 + \frac{1}{4}(\phi_u - \phi_d)^2 \tag{2.22}$$

$$\beta_3 = \frac{13}{12}(\phi_c - 2\phi_d + \phi_{dd})^2 + \frac{1}{4}(3\phi_c - 4\phi_d + \phi_{dd})^2 \tag{2.23}$$

Using these smooth indicators, the nonlinear weight function of ω_k are calculated as

$$\omega_k = \frac{\tilde{\omega}_k}{\tilde{\omega}_1 + \tilde{\omega}_2 + \tilde{\omega}_3} \quad \text{with} \quad \tilde{\omega}_k = \frac{\gamma_k}{(\epsilon + \beta_k)^2} \tag{2.24}$$

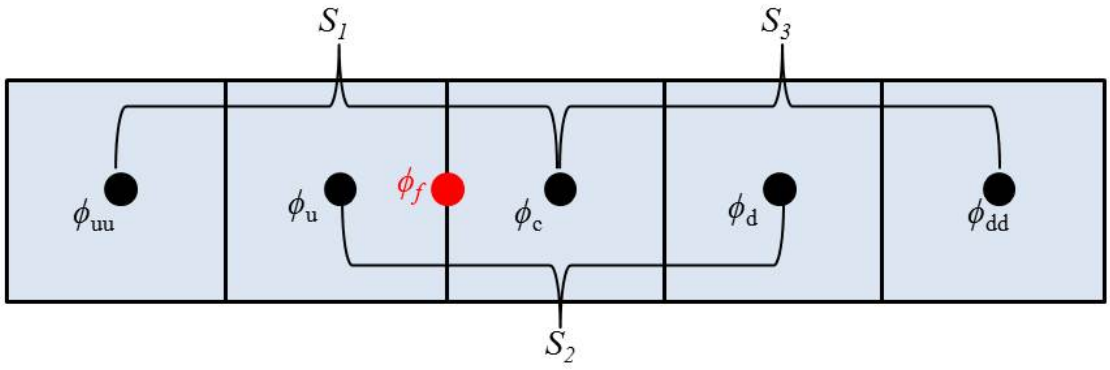

Figure 2–6: Three subsets of stencils S_1, S_2 and S_3 and their relation to the five points used in the 5th-order WENO interpolation scheme

ϵ is a small positive number to avoid dividing zero at denominator. $\epsilon = 10^{-6}$ for most of the cases.

CHAPTER 3

JET/WAKE INSTABILITY IN SHALLOW WATERS

3.1 Introduction

The shallow water is a medium to which waves are admissible. The instability of a shear flow in shallow water produces waves. The presence of waves on the other hand affects the instability of a shear flow in the medium. The classical analysis of the shear-flow instability relies primarily on the method of the normal-mode and the evaluation of the eigenvalue of the mode. In this paper, the instability of jet and wake flows in the presence of the waves is studied directly from numerical simulations. Previous studies of the wave effect on shear-flow instabilities were mostly conducted for the analogous problem of the instability in gases - which also is a medium that admits waves. Sandham and Reynolds (1991) conducted the stability calculations using the normal mode approach in a base flow with the hyperbolic tangent (TANH) velocity profile for the ideal gas up to Mach number of $\mathrm{Ma_c} = 1.2$.

The jet and wake instability is complex due to the existence of a sinuous mode and a varicose mode. It is more complex comparing with the mixing layer because the convective velocity of the jet and wake instability is not fixed but dependent on the Froude number or the Mach number of its analogous problem in gases. Chen et al. (1989) and Chen et al. (1990) investigated the wake instability in gases with a Gaussian base velocity profile up to a free stream Mach number of 7 - that is the equivalent of a convective Mach number of 2.1. In this paper, the instability of the jet and wake flows in shallow waters with a hyperbolic secant (SECH) base velocity profile is analysed using the direct method of numerical simulations without making the assumption of the normal mode covering a wide range of convective Froude number varying from 0.06 to 5.6. A highly accurate numerical scheme

by WENO interpolation scheme ((Shu (1998), Shu (2009), Karimpour and Chu (2015)) is employed for the direct numerical simulations using 128, 256 and 512 grid points over one wave length. Accurate results were obtained from refinement of the grid to find convergent solution with less than one percent of numerical error (Wang and Chu (2014)). The calculations for the instability were conducted first in the half jet/wake restricting the instability to varicose mode. The simulations for the full jet/wake define the instability in the subcritical, trans-critical and supercritical range of the convective Froude number. In the trans-critical range, the instability involves both modes - first in varicose mode which is then followed by the sinuous mode. The co-existence of both modes is a process that could not be described by the classical method of the normal mode.

3.2 Direct Numerical Simulation

The shallow-water equations for the direct numerical solutions for the depth h, the velocity components u and v and discharge components $q_x = uh$ and $q_y = vh$ are:

$$\frac{\partial h}{\partial t} + \frac{\partial q_x}{\partial x} + \frac{\partial q_y}{\partial y} = 0 \tag{3.1}$$

$$\frac{\partial q_x}{\partial t} + u\frac{\partial q_x}{\partial x} + v\frac{\partial q_x}{\partial y} = -gh\frac{\partial h}{\partial x} \tag{3.2}$$

$$\frac{\partial q_y}{\partial t} + u\frac{\partial q_x}{\partial x} + v\frac{\partial q_y}{\partial y} = -gh\frac{\partial h}{\partial y} \tag{3.3}$$

where h = flow depth, (q_x, q_y) = x- and y-components of the depth-averaged flow rates, g = gravitational acceleration, (u, v) = x- and y-components of the flow velocity. The discretization of h, q_x, and q_y is on a staggered grid. The discretization of the domain is explained in details in Pinilla et al. (2010). A fourth-order Runge-Kutta method is employed for the time integration. In the staggered grid, q_x and q_y in the momentum equations are not defined at the same location as the water depth h. Interpolation is needed for the face values in a computational cell. Flux limiter is applied only to q_x when q_x is updated using the x-momentum equation, and only to q_y when q_y is updated using the y-momentum equation.

The base flow of the jet/wake has a constant depth $h = H$ and a SECH velocity profile

$$U(y) = U_a + (U_m - Ua)\,\mathrm{sech}^2\frac{y}{\ell_s} \tag{3.4}$$

The maximum velocity U_m occurs at the centerline while the velocity in the ambient is U_a. The base flow as shown in Figure 3–1 is in the form of jet as the ambient velocity U_a is in the same direction as the jet velocity U_m. However, the same SECH profile would become the deficit of the velocity in a wake if the ambient velocity U_a is reversed with a negative value.

The length scale of the SECH velocity profile is ℓ_s. The depth of the base flow is H. The dimensionless parameters are the velocity ratio Γ and jet/wake Froude number Fr respectively defined as follows:

$$\Gamma = \frac{U_m - U_a}{U_m + U_a} \quad \text{and} \quad \mathrm{Fr} = \frac{U_m - U_a}{c_m + c_a} \tag{3.5}$$

in which c_m and c_a are speeds of the gravity waves. In base flow of constant depth, $c_m = c_a = c = \sqrt{gH}$. The maximum of the velocity gradient at the inflection point of the SECH profile is $\hat{U}_y$. The vorticity thickness defined by this gradient at the inflection is $\delta_\omega = (U_m - U_a)/\hat{U}_y$. The relation between the length scales for the profile is $\ell_s = 4\sqrt{3}\,\delta_\omega/9$. The inflection point of the sech profile is located at $\tanh(y_i/\ell_s) = 1/\sqrt{3}$. The corresponding relative velocity at the inflection point is $U_i - U_a = 2(U_m - U_a)/3$. Figure 3–1 delineates the computation domain for the simulation.

Periodic boundary conditions are imposed over one wave length λ_x in the longitudinal direction. The width of the computation domain in the lateral direction is $6\lambda_x$ for most calculations presented in this paper. For incompressible flows that are not admissible to waves, the instability problem associated with the SECH profile has been analyzed previously by Betchov and Criminale Jr (1966), Chu et al. (1991), Maslowe (1991), Balmforth and Piccolo (2001), Bouchut et al. (2011), Mack (1990) and Kennedy and Chen (1998). The classical method to solve the linear instability problem is the normal mode approach

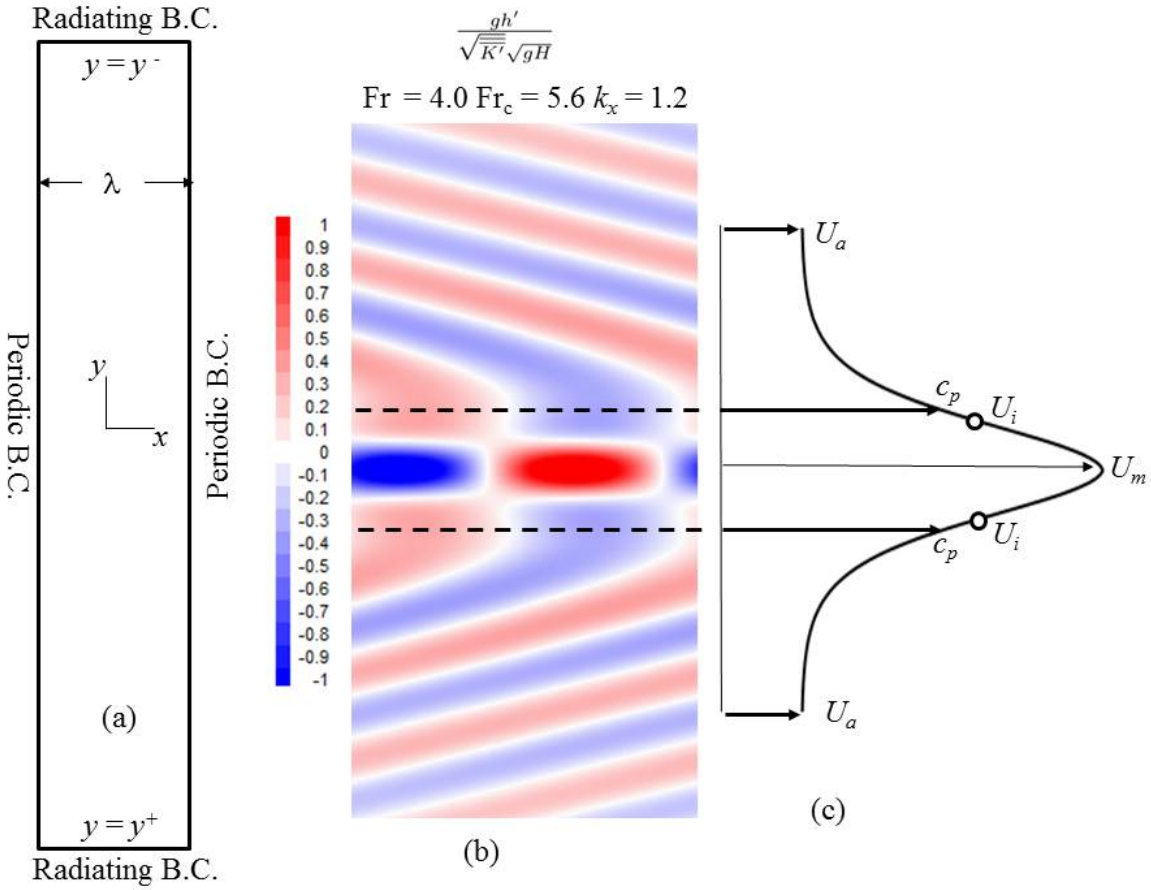

Figure 3–1: (a) Computational domain over one wave length λ_x in the longitudinal direction and from $y = y^-$ to y^+ in the lateral direction for full jet simulations. (b) Depth $gh'/(\sqrt{\overline{\overline{K'}}}\sqrt{gH})$ on $x - y$ plane showing the pattern of the instablility that moves with a velocity c_p in x-direction. c) Hyperbolic secant (SECH) base velocity profile for full jet simulations.

(NMA). In the NMA, the fractional rate of growth is assumed to be constant so that the eigenvalues may be determined from the governing ordinary differential equations. This requirement for the constant fractional rate of growth is restrictive that the method cannot find all the instabilities that emit waves. The additional difficulty of the classical method is the requirement of the method to match the asymptotic solution at the radiating boundary, so that the waves can escape without reflection. The time step used in the numerical simulation was selected so that the Courant number Co $= (\Delta t/\Delta x)\text{Max}[\sqrt{gh}, |u|] = 0.2$. For computational efficiency, most of the present DNS were conducted with a non-zero ambient velocity $U_a = -0.5(U_m - U_a)$. Extensive numerical experiments have shown that the nature of the instability is only dependent on the velocity difference $(U_m - U_a)$ but not on the free stream ambient velocity U_a. Therefore, the shear instability for the jets is the same as the wakes of the same convective Froude number. The Froude numbers considered in the present simulations are in the range varying from Fr $= (U_m - U_a)/[2\sqrt{gH}] = 0.05$ to 4.0. The waves escape without reflection at the lateral boundary $y = y^- = -3\lambda_x$ and $y = y^+ = 3\lambda_x$. The radiation boundary conditions are

$$v = -\sqrt{\frac{g}{h}}(h - H) \quad \text{at} \quad y = y-, \quad v = \sqrt{\frac{g}{h}}(h - H) \quad \text{at} \quad y = y+ \tag{3.6}$$

A small disturbance to the depth of water equal to $h' = 2\ell_s * 10^{-6} \sin(2\pi\ell_s/\lambda_x)$ from $y = -\lambda_x/64$ to $\lambda_x/64$ is made to the initially still water.

3.3 Fractional Rate of Growth and Pattern Speed

In an unstable shear flow, all components of the small disturbance h', u' and v' grow exponentially. These include the disturbance kinetic energy $K' = \frac{1}{2}(u'^2 + v'^2)$. In the classical stability analysis, the solution is obtained assuming the normal mode for h', u' and v' as follows:

$$[h', u', v'] = [\hat{h}(y), \hat{u}(y), \hat{v}(y)] \exp ik_x(x - c_T t) \tag{3.7}$$

The imaginary part of the c_T - determined as an eigenvalue in the classical method - is equal to the fractional growth rates

$$\Im(c_T) = \frac{1}{h'}\frac{dh'}{dt} = \frac{1}{u'}\frac{du'}{dt} = \frac{1}{v'}\frac{dv'}{dt}, \tag{3.8}$$

In the present analysis of the instability, this fractional growth rate is directly determined from the numerical simulation by evaluating the average of the kinetic energy $\overline{\overline{K'}}$ and then the fractional growth rate:

$$\alpha = \frac{1}{\sqrt{\overline{\overline{K'}}}}\frac{d\sqrt{\overline{\overline{K'}}}}{dt} = \frac{d\left[\ln\sqrt{\overline{\overline{K'}}}\right]}{dt} \tag{3.9}$$

The averages of the K' are obtained by first integrating from $x = 0$ to λ_x and subsequently from $y = y^-$ to $y = y^+$:

$$\overline{K'}(y,t) = \frac{1}{\lambda_x}\int_o^{\lambda_x} K'dx, \quad \overline{\overline{K'}}(t) = \frac{1}{\delta_\omega}\int_{y^-}^{y^+} \overline{K'}dy \tag{3.10}$$

The real part of the c_T in the normal mode Equation 3.7 is the pattern speed c_p. The pattern velocity c_p is determined from the space-and-time cross correlation of the simulation data. Figure 3–1 shows a wave pattern at one instant of time. The pattern moves in the longitudinal x-direction with a pattern speed c_p. With proper normalization, this wave pattern is unchanged in a moving coordinate following the motion of the pattern. The depth fluctuation gh' and the kinetic energy $\sqrt{\overline{\overline{K'}}}$ grow exponentially at the same rate. The dimensionless variable $gh'/[\sqrt{\overline{\overline{K'}}}\sqrt{gH}]$ that defines the pattern, is a function of the lateral coordinate y and the moving coordinate $\xi = x - c_p t$.

Figure 3–2 shows examples of the simulations and how the fractional rate of growth α is determined. The column of the left-hand side shows the images for the y-component of the velocity fluctuations v' on the y-x plane. The lines in the semi-logarithmic plots in the middle column relates the $\ln(\overline{\overline{K'}})$ versus time $t\hat{U}_y$. The slopes of these lines according to Equation 3.9, are the fractional growth rate α shown on the right-hand column of the figure. For subcritical instability (Fr = 0.5), the fractional growth rate α is perfectly constant

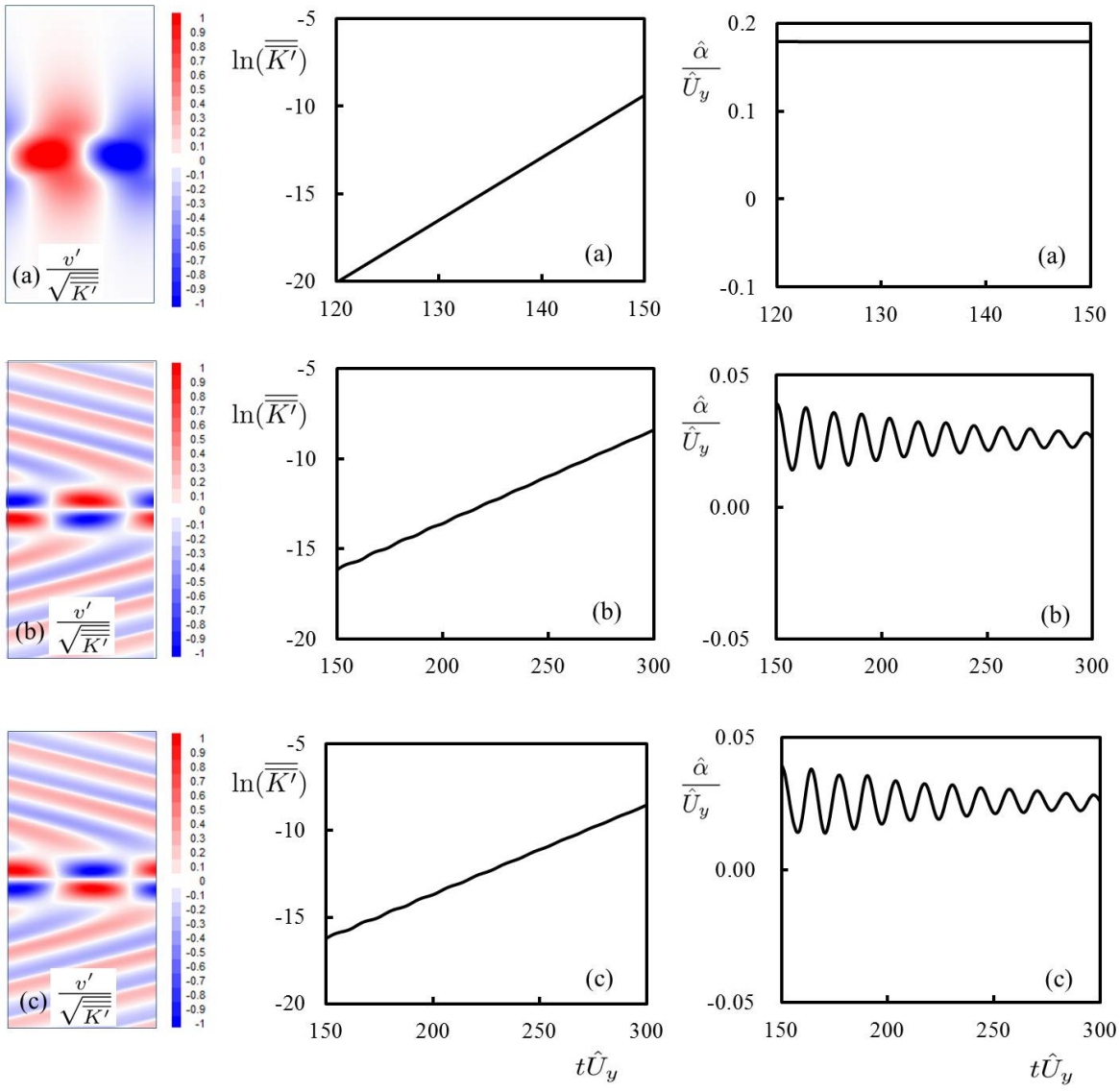

Figure 3–2: Three iconic examples showing the v' pattern on the y-x plane (left), the disturbance kinetic energy on a semi-logarithmic scale (middle), and the fractional growth rate α (right): (a) Sinuious mode of a subcritical wake Fr = 0.5, $\mathrm{Fr_c}$ = 0.6, k_x = 1.0, U_a = -0.5, (b) Varicose mode of a supercritical wake Fr = 4.0, $\mathrm{Fr_c}$ = 5.6, k_x = 1.2, U_a = -0.5. (c) Varicose mode of a supercritical jet Fr = 4.0, $\mathrm{Fr_c}$ = 5.6, k_x = 1.2, U_a = 0.5.

during the linear stage of the instability's development as shown in part (a) of the figure. For supercritical instability (Fr = 4.0), the fractional rate α is not constant but is modulating about an average value as shown in (b) and (c). Despite the modulation, consistent linear structure is maintained as the amplitude of the disturbance is amplified by millions of time.

3.3.1 Convective Froude Number

The SECH velocity profile may represent the base flow of either a jet or a wake dependent on the magnitude and direction of the ambient velocity U_a. The case in Figure 3–2 (b) is the flow profile of a wake where the ambient velocity $U_a = -0.5(U_m - U_a)$. The case in (c) on the other hand is the profile of a jet where $U_a = 0.5(U_m - U_a)$. Extensive numerical experiments have shown that there are no detectable difference between the jets and wakes as they both have the same fractional rate α and the same pattern speed $(c_p - U_a)$. A jet with a positive U_a is the same as a wake with a negative U_a. Therefore from now on, we shall not make distinction between the jets and the wakes and refer to the shear flow as jet/wake. The numerical experiments also have validated the theory by Lin (1953) and Sandham and Reynolds (1991), who suggested the use of velocity $(U_m - U_a)$ to define the convective Mach number to describe the mixing layer in gases. In the mixing layer, the pattern velocity is fixed and is independent of the Froude number (or the Mach number in the analogous gas-dynamic problem). In the jet/wake, the pattern velocity $(c_p - U_a)$ depends on the dimensionless number. Therefore, the convective Froude number $\mathrm{Fr_c}$ is defined based on the pattern velocity $(c_p - U_a)$:

$$\mathrm{Fr_c} = \frac{c_p - U_a}{\sqrt{g\overline{H}}} \tag{3.11}$$

The relevant dimensionless parameter for the classification of the instability is the convective Froude number. The instability is classified as subcritical if $\mathrm{Fr_c} < 1$ and as supercritical if $\mathrm{Fr_c} > 1$. The convective Froude number $\mathrm{Fr_c}$ is to be distinguished from the jet/wake Froude number Fr defined previously in Equation 3.5. The numerical simulations are conducted by specifying a range of jet/wake Froude number varying from Fr = 0.05 to 4.0 and a range of

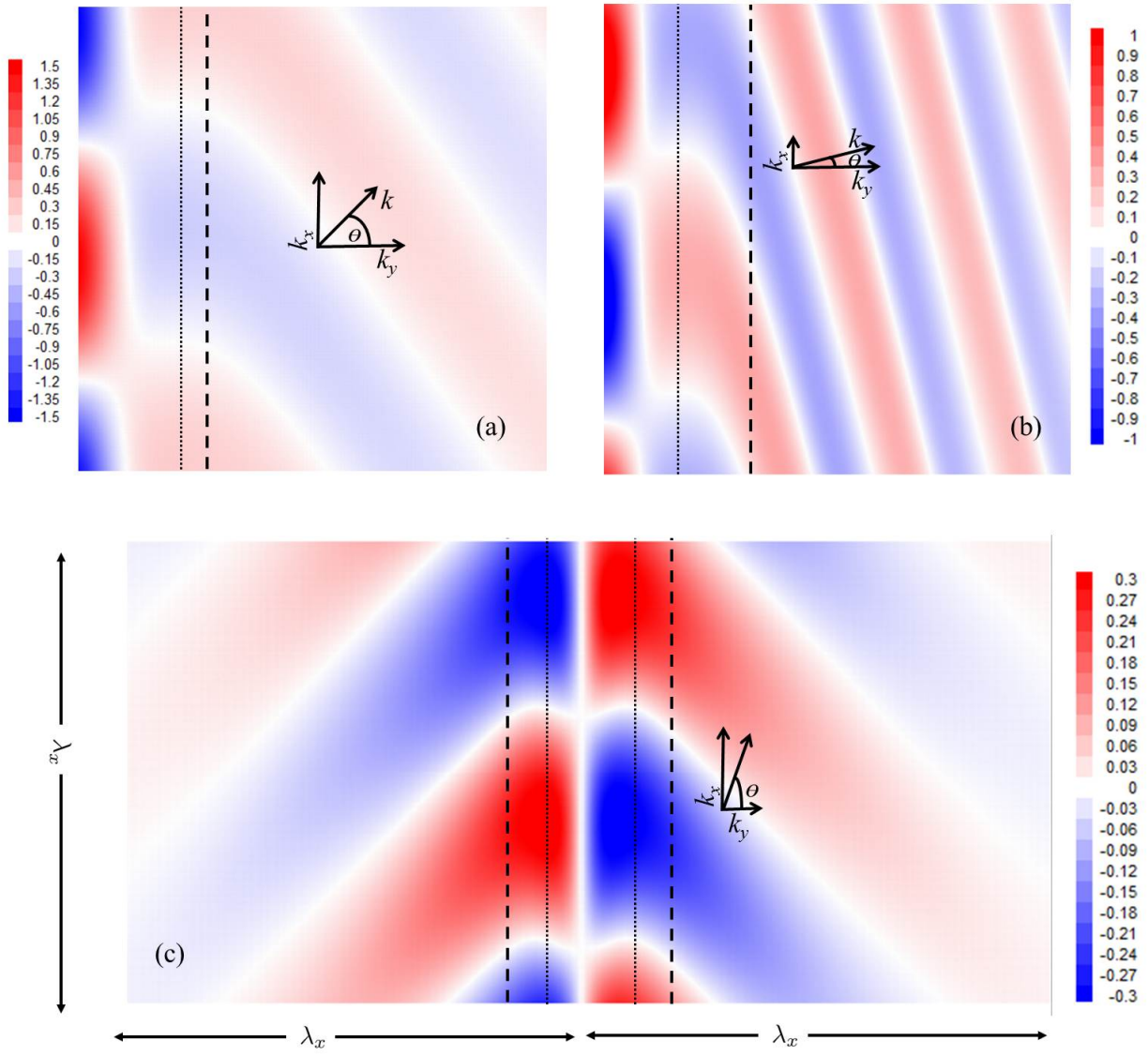

Figure 3–3: Images of the free-surface elevation profiles $gh'/(\sqrt{\overline{\overline{K'}}}\sqrt{gH})$ on the y-x plane that show the waves on the two sides of the returning surface; (a) supercritical half jet/wake with $\mathrm{Fr} = 2.4$, $\mathrm{Fr_c} = 2.8$ and $k_x = 1.2$, (b) supercritical half jet/wake with $\mathrm{Fr} = 4.0$, $\mathrm{Fr_c} = 5.6$ and $k_x = 1.2$, and (c) supercritical full jet/wake with $\mathrm{Fr} = 1.6$, $\mathrm{Fr_c} = 2.0$ and $k_x = 0.5$. The dashed line marks the location of the returning surface where $U = \sqrt{gH}$. The thin dot-dot line marks the location where $U = c_p$.

x-component of wave number varying from $k_x = 2\pi\ell_s/\lambda_x = 0$ to 2.8. The fractional growth rate α and pattern speed c_p are the parameters that are evaluated for each simulation. The convective Froude number are determined once c_p is evaluated. The dependence of the key parameters such as α and c_p, on the Fr, $\mathrm{Fr_c}$ and k_x will be given in the subsequent sections.

The mode of the oscillations is observed in the images on the left-hand side of Figure 3–2 to be either sinuous or varicose depending on whether the v' is symmetrical or antisymmetrical, respectively. For the sinuous mode, v' is maximum at the centerline as shown in (a) of the images on the left-hand side of Figure 3–2. For the varicose mode, v' is zero at the centerline as shown in (b) and (c) of the images.

3.3.2 Direction of the Waves

Beside the symmetry and antisymmetry, the images on the left-hand column of Figure 3–2 also show the direction of the waves. The pattern of the waves depends on the convective Froude number. The direction of the waves is only in the longitudinal x-direction in subcritical instability as shown in (a) of the images. The wave direction can be in both x- and y-directions in supercritical instability as shown in (b) and (c). Additional examples of the waves are shown in Figure 3–3 (a) and (b) for the half jet/wake for Fr = 2.4 and 4.0, respectively. The demarcation between regions of waves of different directions is the returning surface - shown as the dashed line in the figure - where the local current speed U matches the wave speed $\sqrt{gH}$. In the free stream outside of the jet/wake where $U \simeq U_a$, the wave length is λ_{ya} and the wave number is $k_{ya} = 2\pi/\lambda_{ya}$. For the waves inside the returning surface, the wave number is k_x. For waves outside the returning surface in the free stream where $U \simeq U_a$, the wave number is $k = \sqrt{k_x^2 + k_{ya}^2}$. The direction angle θ for the waves in the free stream therefore is

$$\sin\theta = \frac{k_x}{k} = \frac{k_x}{\sqrt{k_x^2 + k_{ya}^2}} \tag{3.12}$$

in which k_x is specified while k_{ya} is determined from the simulation. Further explanation of the returning surface as a demarcation line between regions of waves of different directions

will be given in the subsequent sections.

3.4 Stability Diagram for Half Jet/Wake

The simulations have been carried out for half jet/wake and full jet/wake for a range of different $\mathrm{Fr_c}$ and k_x. The half jet/wake is an artificial mean of producing the varicose mode of oscillations by imposing a solid boundary at the centerline, that is to set $v' = 0$ at $y = 0$. The images in Figure 3–3 (a) and (b), are examples of the varicose mode in the half jet/wake. The images in Figure 3–3 (c) shows the example of the sinuous mode in full jet/wake. The varicose mode of the half jet/wake is to be examined first. The sinuous mode and the varicose mode of the full jet/wake will be considered in the subsequent section.

Figure 3–4 shows two distinctively different kinds of varicose mode. The dimensionless pattern speed $(c_p - U_a)/(U_m - U_a)$ as shown in (c) is either greater than two-third or smaller than two-third depending on whether the instability is subcritical or supercritical, that is

$$\frac{(c_p - U_a)}{(U_m - U_a)} > \frac{2}{3} \text{ for Fr} < 1, \quad \frac{(c_p - U_a)}{(U_m - U_a)} < \frac{2}{3} \text{ for Fr} > 1 \tag{3.13}$$

The dimensionless relative speed at the inflection point of the SECH profile is equal to the two-third of $(U_m - U_a)$. The fractional growth rate α for the subcritical instability also is distinctly different from the rate for the supercritical instability. As shown in (a) of the figure for subcritical instability, α decreases with the increase of Fr. For the supercritical instability on the other hand, α increases with the increase of Fr. The dashed line in Figure 3–4 (a) and (b) delineated the results obtained by Betchov and Criminale Jr (1966) for the limiting case when $\mathrm{Fr} \to 0$ - that is when the wave speed in the medium is infinitely large. The trend of this limiting case obtained by Betchov and Criminale Jr (1966) is clearly consistent with the present simulations.

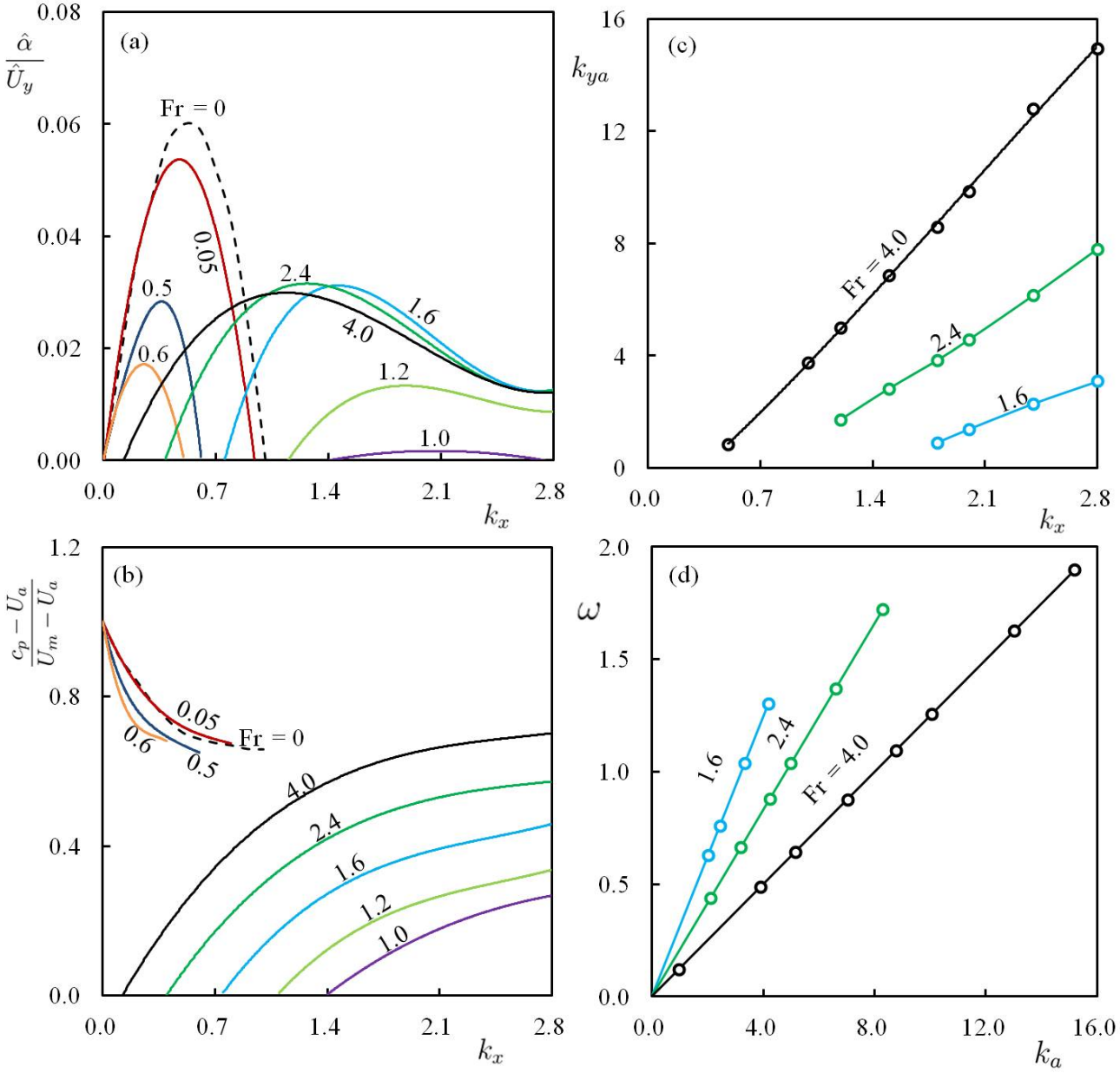

Figure 3–4: Stability diagram for the half jet/wakes; (a) the fractional rate α, (b) the dimensionless pattern phase speed $(c_p - U_a)/(U_m - U_a)$, (c) The y-component of the wave number in the ambient free stream $k_y a$ and (d) the wave frequency ω.

3.4.1 Oblique Waves Direction and Frequency

Oblique waves are observed in the supercritical instability when the relative pattern speed is greater than the speed of the surface wave, that is when the convective Froude number $(c_p - U_a)/\sqrt{gH} > 1$. The direction of these oblique waves in the ambient free stream where $U \simeq U_a$ is defined by the component of the wave number in the ambient free stream $k_{ya} = 2\pi/\lambda_{ya}$. The simulation data for the dependence of this k_{ya} on Fr and k_x obtained for the simulations for the supercritical instability are shown in Figure 3–4 (c). The simulation data for the dependence of wave frequency ω on Fr and k_x are shown in Figure 3–4 (d). The data of k_{ya} in (c) define the oblique angle of the waves which will be explained further in a subsequent section. The simulation data agree well with the dispersion relation $\omega/k_a = \sqrt{gH}$, which is shown as the lines shown in Figure 3–4 (d).

3.5 Simulations for the Full Jet/Wake

The mode of oscillations of the full jet/wake can be sinuous or varicose. It also can be both sinuous and varicose at different time in a simulation. The direct numerical simulations have provided various aspects of the instability - not all are available from the solution of the eigenvalue problem in the normal mode approach. The stability diagram in Figure 3–5 summarizes four key parameters that have been obtained from the simulations of the full jet/wake. These include (a) the fractional growth rate α, (b) the pattern speed c_p, (c) the component k_{ya} of the wave number in the free stream and (d) the wave frequency ω. The fractional rate α is determined by the increase in the disturbance's kinetic energy as explained in the previous sections. The pattern speed c_p, the wave number k_{ya} and the wave frequency ω are determined from the simulations by tracking features of the time-variation profiles and the spatial-variation profiles. The direct numerical simulation results are consistent with the classical results by Betchov and Criminale Jr (1966) which are shown in Figure 3–5 (a) and (b) as dashed line for the limit case of the incompressible medium when Fr $\to 0$. One remarkable of the instability is the change of mode from varicose to sinuous mode in

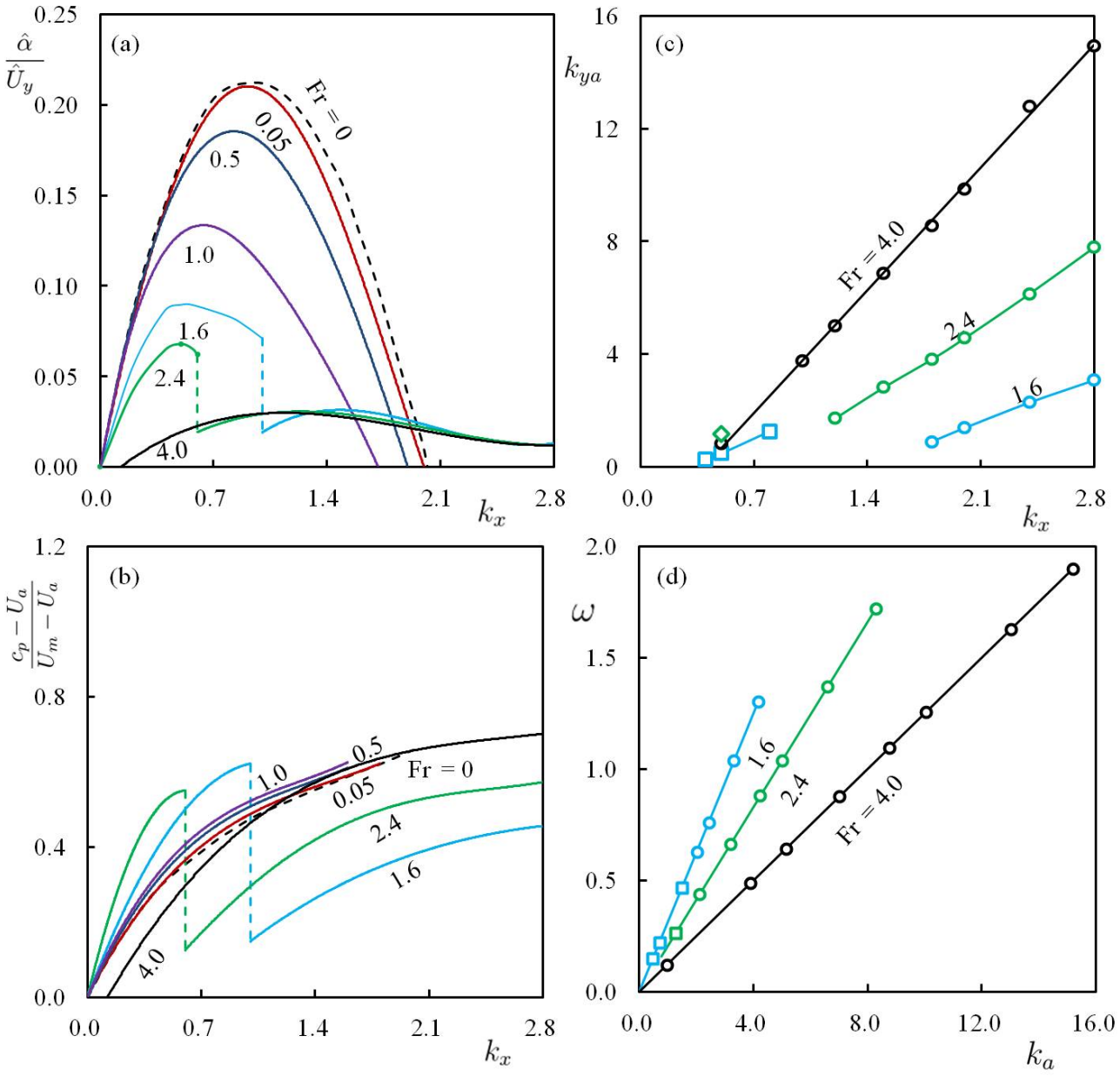

Figure 3–5: Stability diagram for the full jet/wakes; (a) the fractional rate α, (b) the dimensionless pattern phase speed $(c_p - U_a)/(U_m - U_a)$, (c) The y-component of the wave number in the ambient free stream $k_y a$ and (d) the wave frequency ω.

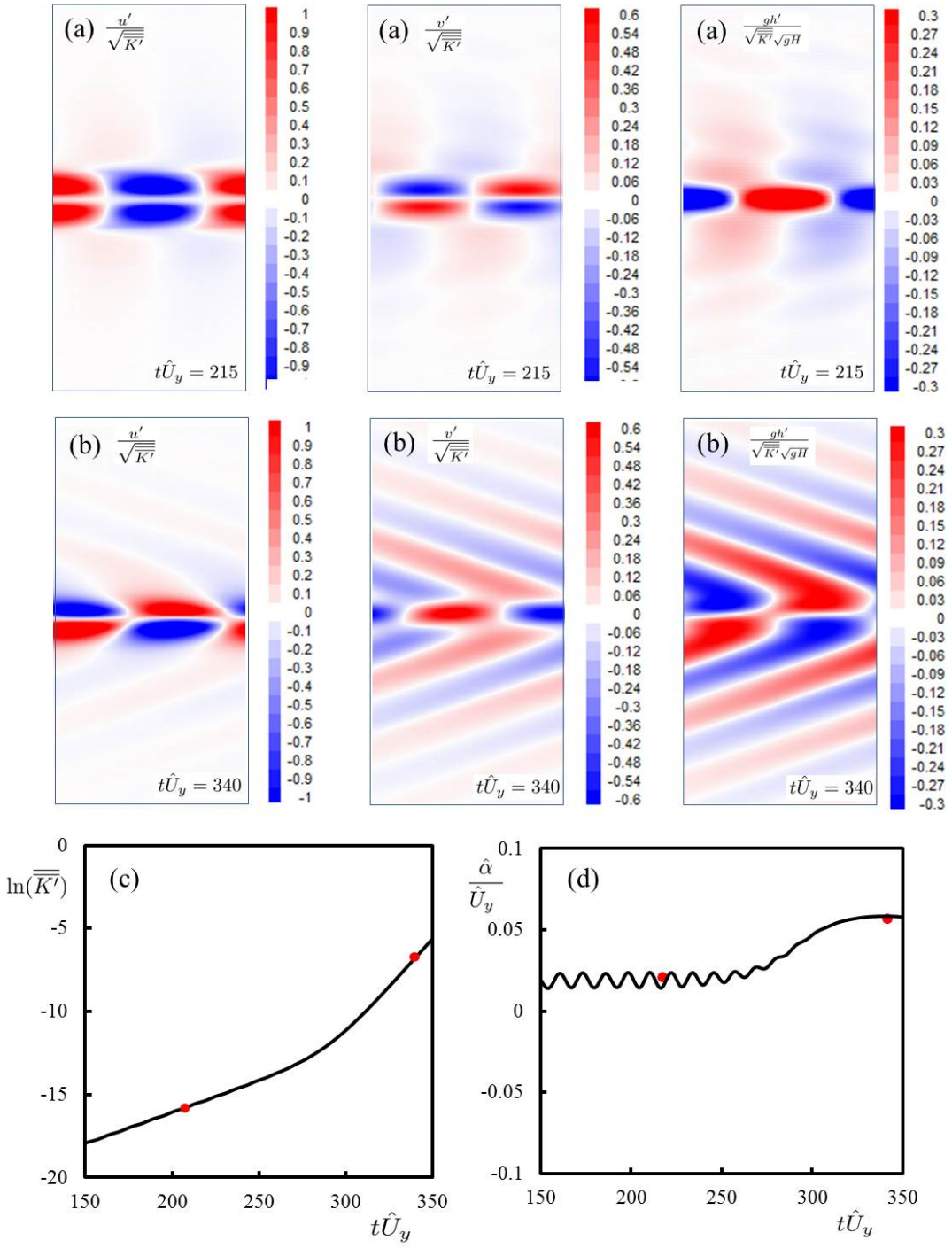

Figure 3–6: Change from varicose mode to sinuous mode in the development of the instability for Fr = 2.8, $\mathrm{Fr_c} = 3.4$, $k_x = 0.5$. (a) The varicose mode of the velocity and depth fluctuation patterns on the y- and x-plane in the first stage at time $t\hat{U}_y = 215$. (b) The sinuous mode in the second stage at time $t\hat{U}_y = 340$. (c) The growth of the disturbance's kinetic energy with time on a semi-logarithmic scale. (d) The fractional rate of the growth in the two stages.

the development of the instability. Figure 3–6 shows an example of such development for the jet/wake with a Froude number of Fr = 2.8 and wave number $k_x = 0.5$. The development of this instability is first in varicose mode of oscillations as shown in part (a) of the figure for time $t\hat{U}_y = 215$, and then changes to sinuous mode as shown in (b) for time $t\hat{U}_y = 340$. The amplitude of the instability grows first at a lower rate and then at a higher rate as shown in (c) and (d) of the figure. In the varicose stage of its development from the time $t\hat{U}_y =$ 150 to 250, the fractional growth rate is oscillatory modulating about an averaged value of about $\overline{\alpha} \simeq 0.015$. In the sinuous stage later in the development from the time $t\hat{U}_y = 300$ to 350, the fractional growth rate is the significant higher value of $\overline{\alpha} \simeq 0.055$. The co-existence of the two modes of different fractional rates in the development of this instability at the jet/wake Froude number of the Fr = 2.8 - and other instability in the trans-critical range of the jet/wake Froude number Fr = 1.0 to 2.8 - is remarkable. This is the kind of instability that could not be determined by the classical method of the normal mode because the implicit in the normal mode approach is the assumption that the fractional rate of the growth is one constant value independent of time.

3.6 Maximum Rate of Growth

The fraction rate of growth α is a function of the wave number k_x and the Froude number Fr as shown in Figure 3–4 and Figure 3–5. For each Froude number Fr, a maximum growth rate $\hat{\alpha}$ is found to occur at a wave $\hat{k}_x$. This maximum rate is most significant as the instability is amplified selectively over the entire range of the wave numbers. Figure 3–7 shows the property of the waves that is selected for the maximum growth. The development of the full jet at the selected maximum rate of the growth is denoted by the solid symbols in the figure. At low Froude number, the oscillations of the full jet/wake follow the sinuous mode as denoted by the solid-square symbol in the figure. At sufficiently large Froude number when Fr > 2.8 or when $\mathrm{Fr_c} > 3.3$, only the varicose mode is possible. This varicose mode in the development of the full jet for the selected maximum rate is denoted in the figure by

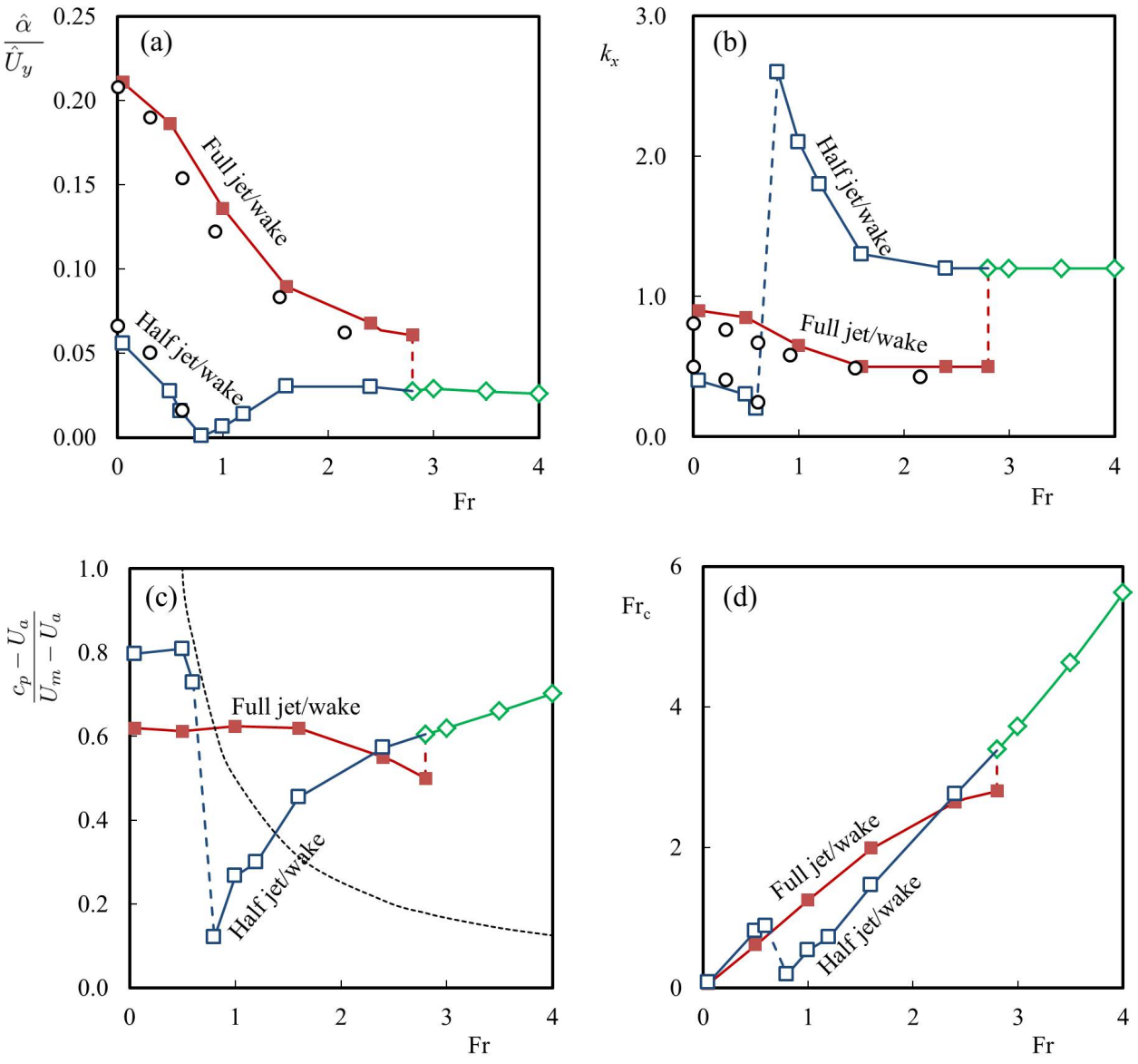

Figure 3–7: The summary plot of (a) the maximum growth rate, (b) the corresponding wave number, (c) the pattern speed and (d) the convective Froude number, against Froude number for both full jet/wake and half jet/wake. The solid symbols are full jet/wake simulations and the open symbols are half jet/wake simulations. The circular symbols are results from Chen et al. (1990). The square symbols are $Fr_c < 3.4$. The diamond symbols are for jet/wake in varicose mode. The dashed line in (c) marks the wave speed $\sqrt{gH}$.

the empty-diamond symbol. The maximum fractional rate of the growth $\hat{\alpha}$ is reduced with the Froude number from a value of about 0.21 in the limit of zero Froude number to a value of about 0.02. This trend is consistent with the previous simulation results by Chen et al. (1990) denoted by the circular symbol. On the whole, the pattern speed of the wave $(c_p - U_a)$ shown in (c) of the figure is between 0.6 to 0.7 time of the velocity across the jet/wake. This pattern speed not coincidentally is approximately equal to the flow at the inflection point of the SECH profile where the shear rate is maximum. The relation between the convective Froude number - which defines the nature of the stability - and the jet/wake Froude number is given in (d) of the figure. The convective Froude number is initially approximately equal to the Froude number. The value relative to jet/wake Froude number increase by 40 %, that is $\mathrm{Fr_c} = 1.4\mathrm{Fr}$ when the jet/wake Froude number increases to a value of $\mathrm{Fr} = 4.0$.

3.7 Waves Pattern across the Returning Surface

The pattern of the wave motion in the instability therefore is closely related to the location of the returning surface where the velocity of the profile U matches the wave velocity $\sqrt{gH}$. Figure 3–8 shows the profile of the waves on the two sides across the returning surface. The dashed line marks the location of the returning surface. The thin dot-dot line is where the velocity U is equal to the pattern velocity c_p. For subcritical instability as shown in the examples in the top row of Figure 3–8, the amplitude of waves decays monotonically away from the shear flow as $y \to \pm\infty$. For supercritical instability, the decay is not monotonic but is associated with radiation of waves from the shear flow. Figure 3–9 (a) shows how these waves may be initiated due to the generating source that moves with a velocity equal to the pattern velocity $(c_p - U_a)$. At supercritical speed when $(c_p - U_a) > \sqrt{gH}$ - that is when $\mathrm{Fr_c} > 1$ - the wave front would have an oblique angle given by

$$\sin\theta = \frac{\sqrt{gH}}{(c_p - U_a)} \tag{3.14}$$

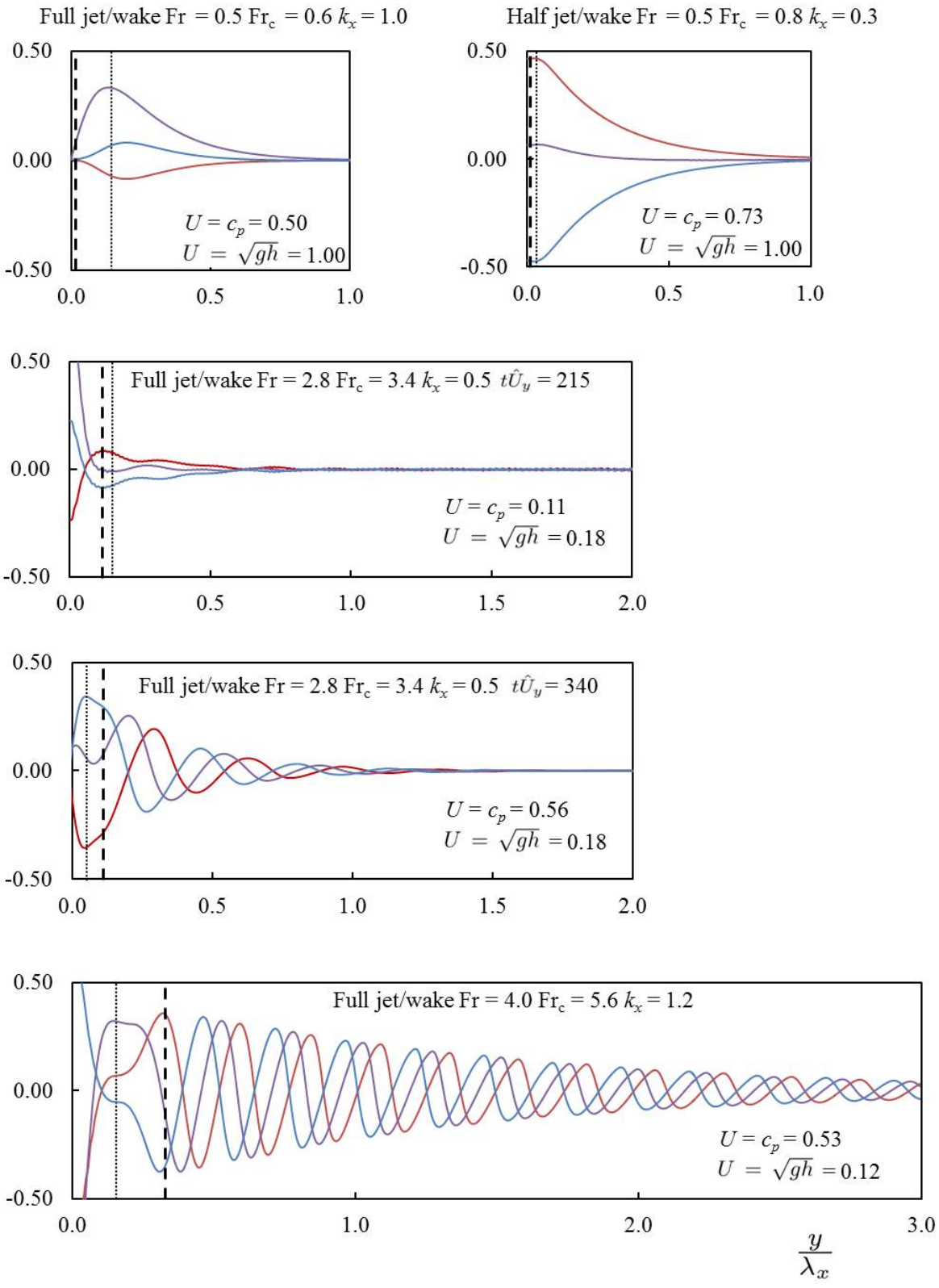

Figure 3–8: Profiles of $gh'/(\sqrt{\overline{\overline{K'}}}\sqrt{gH})$ showing the wave propagation for Fr = 0.5 , 2.8 and 4.0. The red line is located at position $x = 1/4\lambda_x$. The purple line is located at position $x = 1/2\lambda_x$. The blue line is located at position $x = 3/4\lambda_x$

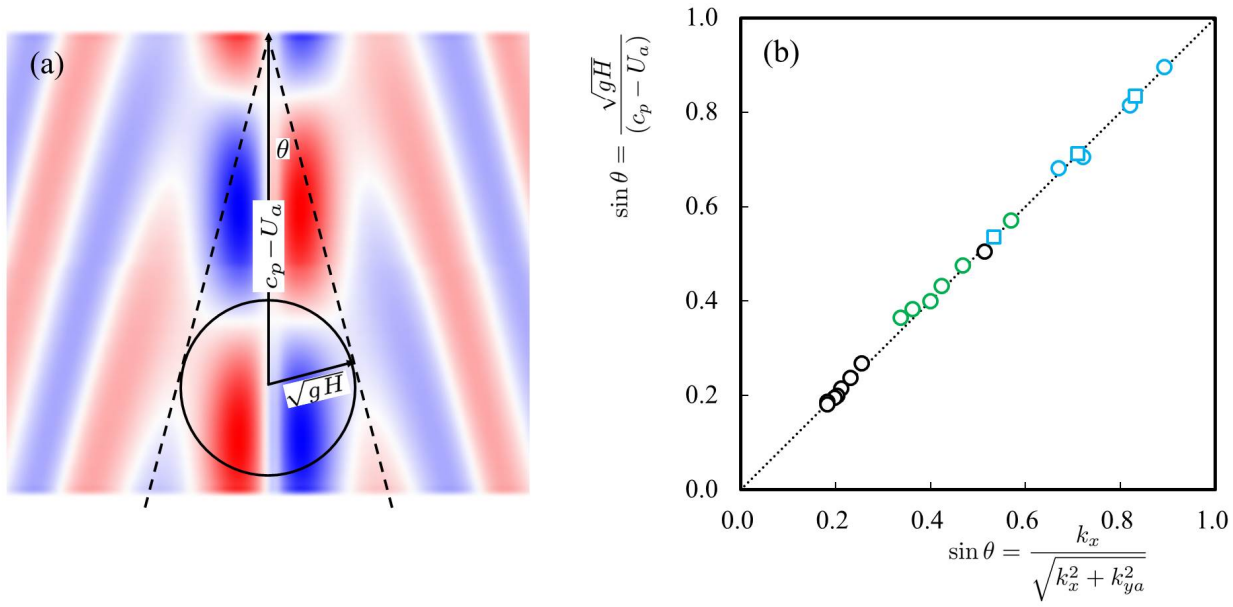

Figure 3–9: (a) Radiation of the waves from the instability that are moving forward in the longitudinal direction with the velocity $c_p - U_a$ for Fr = 4.0 and $k_x = 1.2$. The dash line shows the Froude lines. (b) The computation of the wave angles in two different methods for Fr =1.6, 2.4 and 4.0. The circular symbols are from half jet/wake simulation and the square symbols are from full jet/wake simulation.

The $\sin\theta$ evaluated using this formula that is Equation 3.14 for all simulations of the supercritical instability is plotted against the other $\sin\theta$ evaluated using Equation 3.12 in Figure 3–9 (b). The evaluation of the angle θ for all simulations based on these two equations has produce the same results. The c_p in Equation 3.14 is determined from the simulation completely independent of the determination of k_{ya} used in Equation 3.12. The agreement in the oblique-wave angles obtained between the two methods therefore supports the hypothesis that the oblique waves outside the returning surface are generated by the moving source.

3.8 Summary and Conclusion

The direct numerical simulation of the shear instability with a SECH based velocity profile has determined the fractional growth rate and the pattern of wave development. Some of the parameters such as the linear growth rate of the supercritical flows associated with the instability but can not be determined by the classical analysis using the normal

mode. The calculations for the jet/wake instability associated with the SECH profile have covered a range of convective Froude number from 0.06 to 5.6 (Froude number from 0.05 to 4.0). The dominant mode of the instability is the sinuous modes when the convective Froude number is small. The instability changes to varicose mode when the convective Froude number exceeds a critical value of about 3.4. These calculations of shear instability for the SECH velocity profile are most significant in the study of high-speed currents whether they are free-surface flow in open channels or density current in density stratified flow. The simulations for the instability are presented in the paper for the small amplitude waves when the nonlinear terms in the governing equations are negligible. The subsequent finite development of the instability for studying the transition to turbulence is to be reported in a companion publication.

CHAPTER 4

NON-LINEAR TRANSITION OF JET/WAKE INSTABILITY IN SHALLOW FLOWS

4.1 Introduction

The study of shear instability and its transition to turbulence in shallow flows are fundamental to the understanding of the circulations in the atmosphere, oceans and coastal waters. The depth of these flows are considered to be shallow in comparison with the large horizontal extent of the circulations (Jirka (1994), Chu (2002)). Waves can affect significantly the turbulent exchanges across the shallow shear flow particularly in flows with large Froude number (Chu (2010)). Despite the ubiquitous presence of the surface gravity waves in steep channels and the interfacial waves in gravity currents, relevant literature of the wave effect is mostly found in the studies of analogous problem in gas dynamics. The studies of the dilation effect in gas dynamics have revealed the exchange processes to depend on Mach number. Early evidence of the effect on turbulence was consider by Bradshaw (1977). Experimental studies by Papamoschou and Roshko (1988), Elliott and Samimy (1990) and Rossmann et al. (2002) have identified the convective Mach number as the parameter and reported the reduction of mixing rate with the convective Mach number. Chen et al. (1990), Mack (1990), Sandham and Reynolds (1991), Vreman et al. (1996), and Pantano and Sarkar (2002) among others have conducted numerically simulations to show the similar reduction of the turbulence exchanges with the increase in value of the convective Mach number. There are clear evidences that the structure of the turbulence is modified by the presence of shock waves. The intriguing effect due to shock wave presence on turbulence has been associated with the formation of eddy (Lee et al. (1991)). Closely analogous effect of the gravity waves

on the turbulent exchanges in shallow waters is expected as the governing shallow-water equations are similar in form to the gas dynamic equations (Liggett (1994)).

In this paper, the transition of instability to turbulence is considered for the jet/wake shallow flows with a hyperbolic-secant (SECH) velocity profile as shown in Figure 4–1. The numerical simulations start with a small perturbation to the base flow. The transition to turbulence begins when the amplitude of the disturbance has grown sufficiently large to modify the mean flow. The role of the waves on the transition is examined for a wide range of initial Froude number varying from Fr = 0.05 to 4.0. The simulation data are analysed for the formation of the eddy in shear flow of small Froude number and the formation of eddy-shocklet - that involves shock waves - in shear flow of sufficiently large Froude number. The present simulations for the transition of the jet/wake instability to turbulence are complementary to a companion paper dealing with the linear problem when the amplitude of the disturbance is negligible in the development of the instability.

4.2 Direct Numerical Simulation

The simulations for the depth h, the velocity components u and v and discharge components $q_x = uh$ and $q_y = vh$ in the shallow flows are based on the shallow-water equations:

$$\frac{\partial h}{\partial t} + \frac{\partial q_x}{\partial x} + \frac{\partial q_y}{\partial y} = 0 \tag{4.1}$$

$$\frac{\partial q_x}{\partial t} + u\frac{\partial q_x}{\partial x} + v\frac{\partial q_x}{\partial y} = -gh\frac{\partial h}{\partial x} \tag{4.2}$$

$$\frac{\partial q_y}{\partial t} + u\frac{\partial q_x}{\partial x} + v\frac{\partial q_y}{\partial y} = -gh\frac{\partial h}{\partial y} \tag{4.3}$$

where h = flow depth, (q_x, q_y) = x- and y-components of the depth-averaged flow, g = gravity, (u, v) = x- and y-components of the flow velocity. The discretization of h, q_x, and q_y is on a staggered grid. The discretization of the grid is explained in Pinilla et al. (2010) and Karimpour and Chu (2015). A fourth-order Runge-Kutta method is employed for the time integration. In the staggered grid, q_x and q_y in the momentum equations are not defined

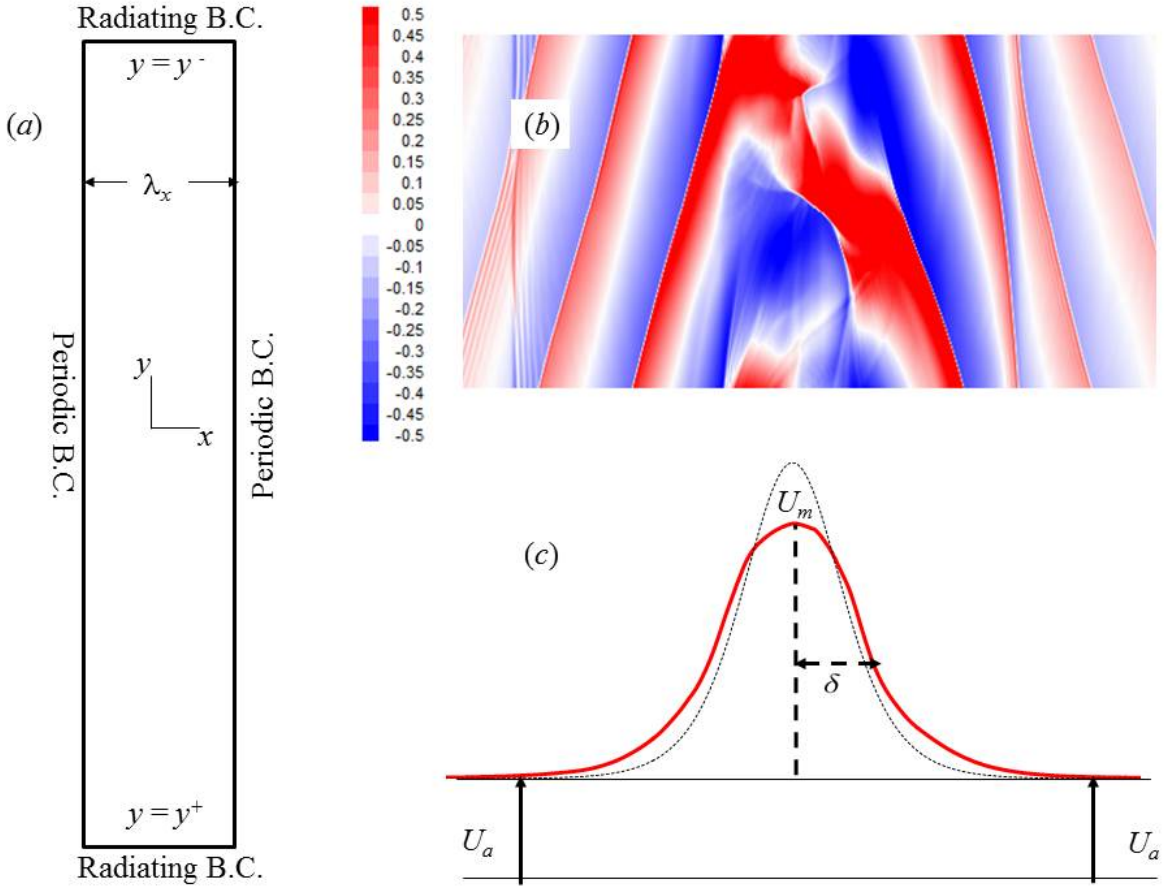

Figure 4–1: (a) Computational domain with periodic boundary conditions over one wavelength λ_x in the longitudinal direction and radiating boundary conditions at $y = y^-$ to y^+. (b) Water depth fluctuations $gh'/(\sqrt{\bar{K}'}\sqrt{gH})$ for Fr =4.0 $k_x = 1.2$. (c) Mean velocity profile with maximum velocity U_m and half width δ.

at the same location as the water depth h. Interpolation is needed for the face values in a computational cell. Flux limiter is applied only to q_x as q_x is updated using the x-momentum equation, and only to q_y as q_y is updated using the y-momentum equation.

The base flow of the jet/wake has a constant depth $h = H$ and a SECH velocity profile

$$U - U_a = \Delta_o \operatorname{sech}^2 \frac{y}{\ell} \tag{4.4}$$

where U_a is the ambient velocity and $(U - U_a)$ is the velocity relative to the ambient; Δ_o is the velocity scale and ℓ the length scale of the profile. The velocity gradient at the inflection point of the SECH profile is $\hat{U}_y$. It defines the vorticity thickness $\delta_\omega = \Delta_o/\hat{U}_y$, which is equal to $9\ell/(4\sqrt{3})$. The inflection point is located at $y_i = \tanh(y_i/\ell) = 1/\sqrt{3}$, where the relative velocity is $\Delta_i = 2\Delta_o/3$. The sketch in Figure 4–1 shows the jet in a co-flow with an ambient velocity U_a in the direction of the jet velocity. The same SECH profile would become the velocity deficit of a wake if the ambient velocity U_a is reversed with a negative value. Numerical experiments have shown that the instability is dependent on the Δ_o and ℓ, but is not dependent on the ambient velocity U_a. The shear instability for the jets therefore is the same as the wakes of the same convective Froude number. We shall not distinguish a jet from a wake and consider the jet/wake instability and transition to depend only on the Froude number

$$\mathrm{Fr} = \frac{\Delta_o}{c_m + c_a} \tag{4.5}$$

in which c_m and c_a are speeds of the gravity waves. For the base flow of constant depth H, the speeds are $c_m = c_a = c = \sqrt{gH}$. Periodic boundary conditions are imposed over one wave length λ_x in the longitudinal direction. The width of the computation domain in the lateral direction is $6\lambda_x$ for the calculations presented in this paper. The instability of the shear flow with the SECH profile has been analyzed previously by Betchov and Criminale Jr (1966), Chu et al. (1991) and Maslowe (1991) for non-dilating medium that does not admit waves using the classical normal mode approach (NMA). The time step used in the direct numerical simulation (DNS) was selected so that the Courant number $\mathrm{Co} = (\Delta t/\Delta x)\mathrm{Max}[\sqrt{gh}, |u|] =$

0.2. For computational efficiency, the present DNS was conducted with a negative ambient velocity $U_a = -0.5\Delta_o$. The Froude numbers considered in the present simulations are in the range varying from Fr = 0.05 to 4.0. The waves escape without reflection at the lateral boundary $y = y^- = -3\lambda_x$ and $y = y^+ = 3\lambda_x$. The radiation boundary conditions are

$$v = -\sqrt{\frac{g}{h}}(h - H) \;\text{ at }\; y = y-, \quad v = \sqrt{\frac{g}{h}}(h - H) \;\text{ at }\; y = y+ \tag{4.6}$$

The perturbation to the initially still waters is a small depth disturbance equal to $h' = 2\ell_s * 10^{-6} \sin(2\pi\ell_s/\lambda_x)$ over a small region from $y = -\lambda_x/64$ to $\lambda_x/64$ close to the jet/wake's centerline. The disturbances eventually grow to finite amplitude which modified the mean velocity profile to be deviated from the initial SECH profile.

4.3 Mean Velocity Profiles

The mean velocity $U(y,t)$ as a function of y and time t, is calculated from the simulations by averaging over the wave length λ_x:

$$U(y,t) = \int_o^{\lambda_x} u(x,y,t)\,dx, \quad V(y,t) = \int_o^{\lambda_x} v(x,y,t)\,dx = 0 \tag{4.7}$$

Due to symmetry in the boundary condition, the V component is zero. The deviations from the mean velocity therefore are $u' = u - U$ and $v' = v$. The deviation from the mean depth H is $h' = h - H$. Two parameters are introduced to define this relative mean velocity. They are the first moment μ_1 and the second moment μ_2 as follows:

$$\mu_1 = \int_{-\infty}^{+\infty} \frac{U - U_a}{\Delta_o} dy, \quad \mu_2 = \int_{-\infty}^{+\infty} \frac{(U - U_a)^2}{\Delta_o^2} dy \tag{4.8}$$

The width and velocity of the equivalent top-hat velocity profile of the same volume excess flux and momentum excess flux are:

$$\bar{\mu} = \frac{\mu_1^2}{\mu_2}, \quad \bar{\Delta} = \frac{\mu_2}{\mu_1}\Delta_o \tag{4.9}$$

where $\bar{\Delta} = \overline{U} - U_a$ is the velocity of the top-hat relative to the ambient velocity.

4.3.1 Sub-critical, Trans-critical and Supercritical Flows

Simulations were conducted for jet/wake flows of eight different Fr-k_x pairs: (a) Fr = 0.05, $k_x = 1.0$; (b) Fr = 0.5, $k_x = 1.0$; (c) Fr = 1.0, $k_x = 0.8$; (d) Fr = 1.6, $k_x = 0.5$; (e) Fr = 2.4, $k_x = 0.5$; (f) Fr = 3.0, $k_x = 1.2$; (g) Fr = 3.5, $k_x = 1.2$; (h) Fr = 4.0, $k_x = 1.2$. The wave number $k_x = 2\pi/\lambda_x$ is selected for the most unstable wave length λ_x associated with the maximum rate of growth. Figure 4–2 shows mean velocity profiles (solid lines) and the equivalent top-hat profiles (dashed lines) for the eight flow cases (a), (b), (c), (d), (e), (f), (g) and (h), each at three different times associated with the key events that occur at times $t = t_R$, $t = t_{R'}$ and $t = t_S$. We shall discuss the results by referring the transition as sub-critical for the first three flow cases (a), (b) and (c), as trans-critical for the flow cases (d) and (e), and as supercritical for the last three flow cases (f), (g) and (h). This classification as sub-critical, trans-critical and supercritical is related to the wave effect on the transition to be explained subsequently in the later sections.

4.3.2 R-event, R'-event and S-event

Figure 4–3 shows the time series of the disturbance's kinetic energy $\overline{\overline{K'}}$, the top-hat width $\bar{\mu}$, the top-hat velocity $\bar{\Delta}$, the normalized spreading rate $(d\bar{\mu}/dt)/\bar{\Delta}$, and the total energy dissipation (TE-TE$_o$)/$(\bar{\mu}\lambda_x H\overline{\overline{K'}})$ that define the key events: R, R' and S. The disturbance's kinetic energy shown in the first row of the figure is obtained by averaging over the computational domain as follows:

$$\overline{\overline{K'}} = \frac{1}{\bar{\mu}} \int_{y^-}^{y^+} [\frac{1}{\lambda_x} \int_o^{\lambda_x} \frac{1}{2}(u'^2 + v'^2)dx]\ dy \tag{4.10}$$

The time series of the width $\bar{\mu}$ and velocity $\bar{\Delta}$ of the top-hat profiles are shown in the second and third rows. The normalized spreading rate shown in the fourth row of Figure 4–3 is $(d\bar{\mu}/dt)/\bar{\Delta}$. The total energy dissipation spreading rate (TE-TE$_o$)/$(\bar{\mu}\lambda_x H\overline{\overline{K'}})$ is shown in

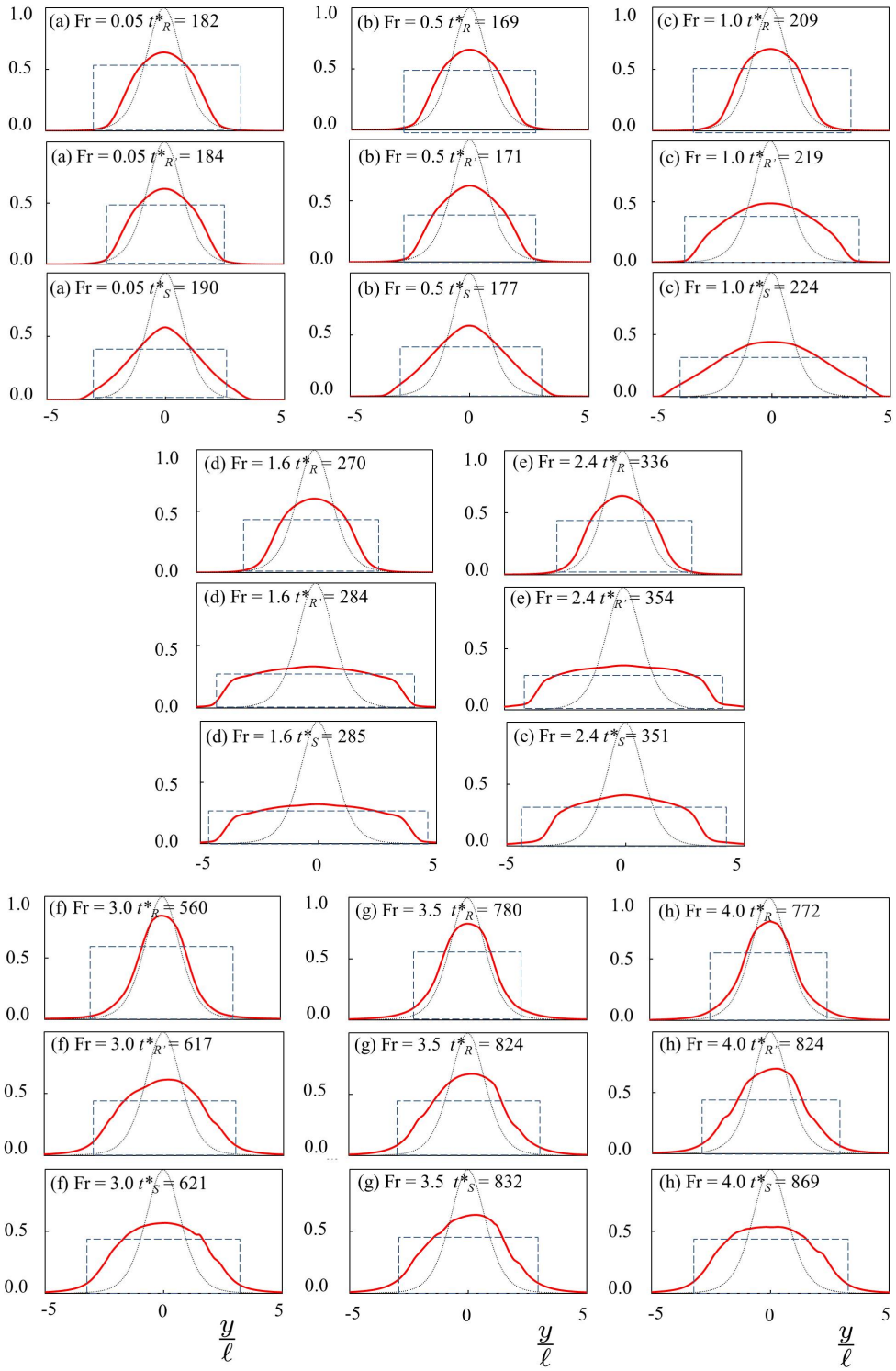

Figure 4–2: Mean velocity profiles $(U - Ua)/\Delta_o$ (solid red lines) at time $t = t^*_R$, $t = t^*_{R'}$ and time $t = t^*_S$ for the initial Froude number (a) Fr = 0.05, (b) Fr = 0.5, (c) Fr = 1.0, (d) Fr = 1.6, (e) Fr = 2.4, (f) Fr = 3.0, (g) Fr = 3.5, (h) Fr = 4.0. The equivalent top-hat profiles are defined by the dashed lines. The initial un-perturbed SECH profile is denoted by the thin dot-dot lines.

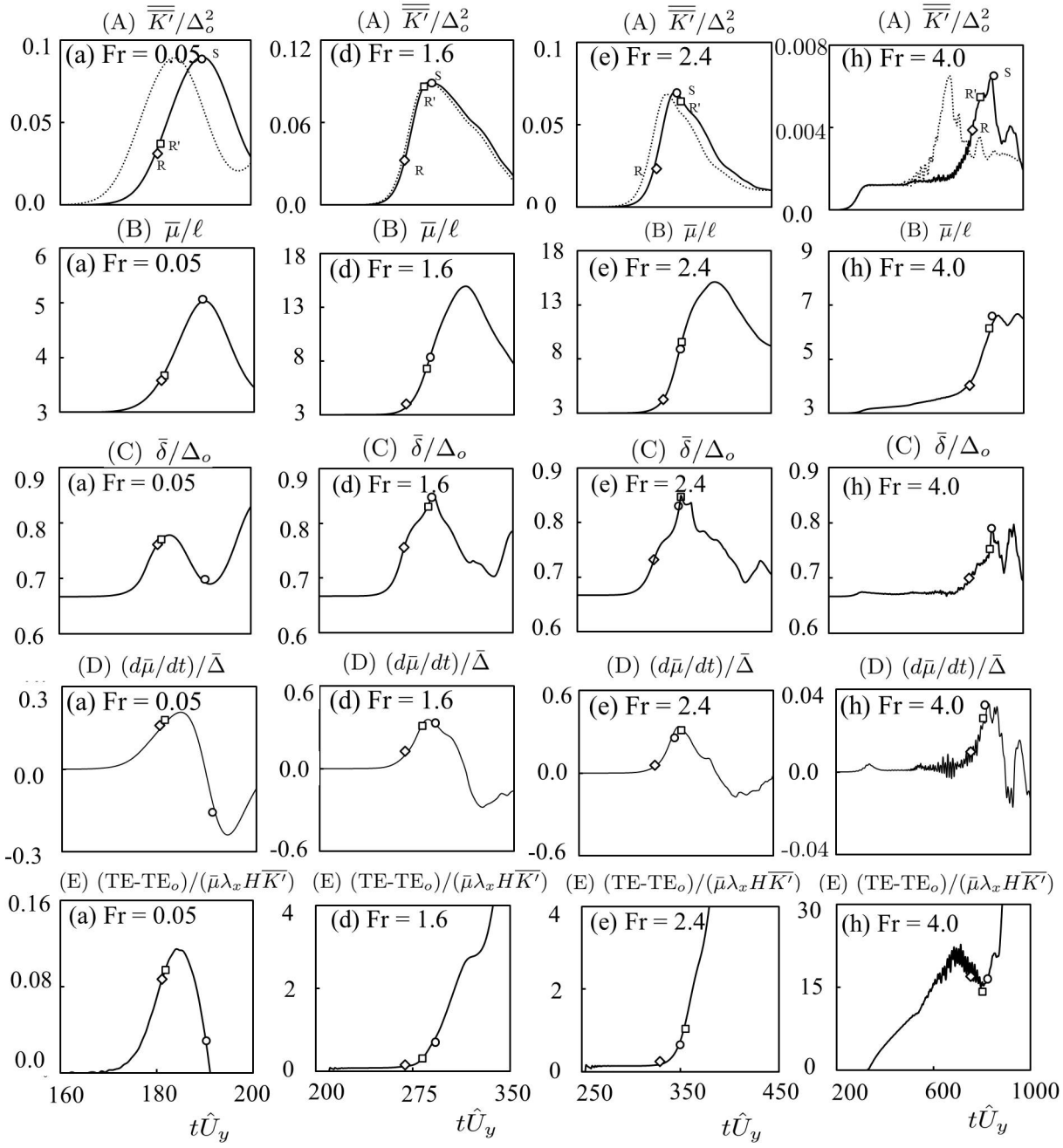

Figure 4–3: Time series of the disturbance's kinetic energy $\overline{\overline{K'}}/\Delta_o^2$ (top row), the top-hat width $\overline{\mu}/\ell$ (2nd row), the top-hat velocity $\bar{\delta}/\Delta_o$ (3rd row), the spreading rate $(d\bar{\mu}/dt)/\bar{\Delta}$ (4th row) and the total energy dissipation (TE-TE$_o$)/($\bar{\mu}\lambda_x H\overline{\overline{K'}}$) (bottom row) for the initial Froude number (a) Fr = 0.05, (d) Fr = 1.6, (e) Fr = 2.4, and (h) Fr = 4.0. The open-diamond symbol marks the R-event, the open-square symbol for the R'-event and the circle symbol for the S-event. The dash line in the top row was obtained from the simulation cases of $U_a = 0.5$.

the last row of Figure 4–3. The kinetic energy rises rapidly during the transition. The key events as marked in the figure are the R-event that occurs at the time $t = t_R$ when the increase of the kinetic energy is most rapidly. The R'-event, at time $t = t_{R'}$, occurs when the width $\overline{\mu}$ increases most rapidly. The S-event occurs at time $t = t_S$ when the disturbance kinetic energy reaches its first saturation peak. For the sub-critical transition (a) Fr = 0.05, and the supercritical transition (h) Fr = 4.0, the R-event and R'-event are occurring at about the same time. The occurrence of the events in the trans-critical range in (d) and (e), is different. For (d) Fr = 1.6 and (e) Fr = 2.4, the occurrence of the R'-event is delayed to a time almost the same as the S-event. The delay is just one of many aspects that distinguish the trans-critical transition from the sub-critical and supercritical transition.

The mean profiles of the three events R, R' and S and the dimensionless time associated with these events ${t^*}_R = t_R\hat{U}_y$, ${t^*}_{R'} = t_{R'}\hat{U}_y$ and ${t^*}_S = t_S\hat{U}_y$, are arranged in group of three as shown in Figure 4–2 for each Froude number and wave number pair (a) to (h). From top to bottom, the width of the flows for each Froude number is observed to increase rapidly with time during the transition from ${t^*}_R$ to ${t^*}_{R'}$ and then to ${t^*}_S$. The mean profiles (red solid lines) and its equivalent top-hat profiles (dashed lines) are to be compared with the initial SECH profile (thin dot-dot lines). The half-width δ is defined at the lateral position $y = \delta$ where the relative mean velocity $(\overline{U} - U_a)$ is equal to one-half of its maximum $\bar{\Delta} = (U_m - U_a)$. The width and velocity of the equivalent top-hat profile are $\overline{\mu}$ and $\bar{\Delta}$. Figure 4–4 (A) shows the dependence of the length-scale ratios $\delta_R/\overline{\mu}_R$ and $\delta_{R'}/\overline{\mu}_{R'}$ on the Froude number for the eight flow cases (a) to (h); the subscripts R and R' denote the time of the event at $t = t_R$ and $t = t_{R'}$, respectively. The velocity difference across the jet/wake initially equal to $\Delta_o = (U_m - U_a)$ is reduced to $\bar{\Delta}_R$ and $\bar{\Delta}_{R'}$. The result is the proportional reduction of the Froude number to Fr_R and $\mathrm{Fr}_{R'}$. Figure 4–4 (B) shows the reduced values of these Fr_R and $\mathrm{Fr}_{R'}$ which are smaller in value compared with the initial value of Fr, and are in much smaller fraction for the trans-critical transition. We see from this figure why the case (d) Fr = 1.6 and the case (e) Fr = 2.4 are in the trans-critical range because the Froude numbers,

Fr_R and $\mathrm{Fr}_{R'}$, are close to the value of unity for the critical flow.

4.3.3 Subcritical, Trans-critical and Supercritical Transitions

The profiles in the trans-critical range of (d) Fr = 1.6 and (e) Fr = 2.4 are to be distinguished from those in the subcritical cases (a) (b) (c) and supercritical cases (f) (g) (h). The width of the mean profile increases with time from $t = t_R$ to $t = t_{R'}$ and then to $t = t_s$. The most rapid of the changes in width occurs between time $t = t_R$ and $t = t_{R'}$. In Figure 4–4 (C), the rates $d\delta_R/dt$ and $d\delta_R/dt$ are correlated with the Froude number Fr. The rate for the subcritical transitions (a) (b) and (c) is

$$\frac{1}{\Delta_R}\frac{d\delta_R}{dt} \simeq \frac{1}{\Delta_{R'}}\frac{d\delta_{R'}}{dt} \simeq 0.1 \quad \text{for} \quad \mathrm{Fr}_R < 1 \tag{4.11}$$

The rate in the trans-critical cases (d) and (e) is

$$\frac{1}{\Delta_R}\frac{d\delta_R}{dt} \simeq 0.09 \quad \text{for} \quad \mathrm{Fr}_R < 1, \frac{1}{\Delta_{R'}}\frac{d\delta_{R'}}{dt} \simeq 0.3 \sim 0.4 \quad \text{for} \quad \mathrm{Fr}_{R'} < 1 \tag{4.12}$$

For the supercritical transitions (f) (g) and (h), the rate is

$$\frac{1}{\Delta_R}\frac{d\delta_R}{dt} \simeq \frac{1}{\Delta_{R'}}\frac{d\delta_{R'}}{dt} \simeq 0.01 \sim 0.03 \quad \text{for} \quad \mathrm{Fr}_R < 1, \tag{4.13}$$

which is almost an order of magnitude smaller than the values of 0.1 of subcritical flow. We see that the normalized spreading rate is significantly greater for the trans-critical transition when the Froude numbers Fr_R and $\mathrm{Fr}_{R'}$ are close to the value of unity. The trans-critical spreading rate is 50% to 100% greater compared with the subcritical rate, and is an order of magnitude greater than the supercritical rate. We do not have yet a good explanation for the greater rate. This increase in the spreading rate of the trans-critical transition is consistent with the disturbance's kinetic energy shown in Figure 4–4 (D). Indeed, and that is not coincidence, the increase in the spreading rate is closely correlating with the intensifying disturbance's kinetic energy in the same range of Froude number.

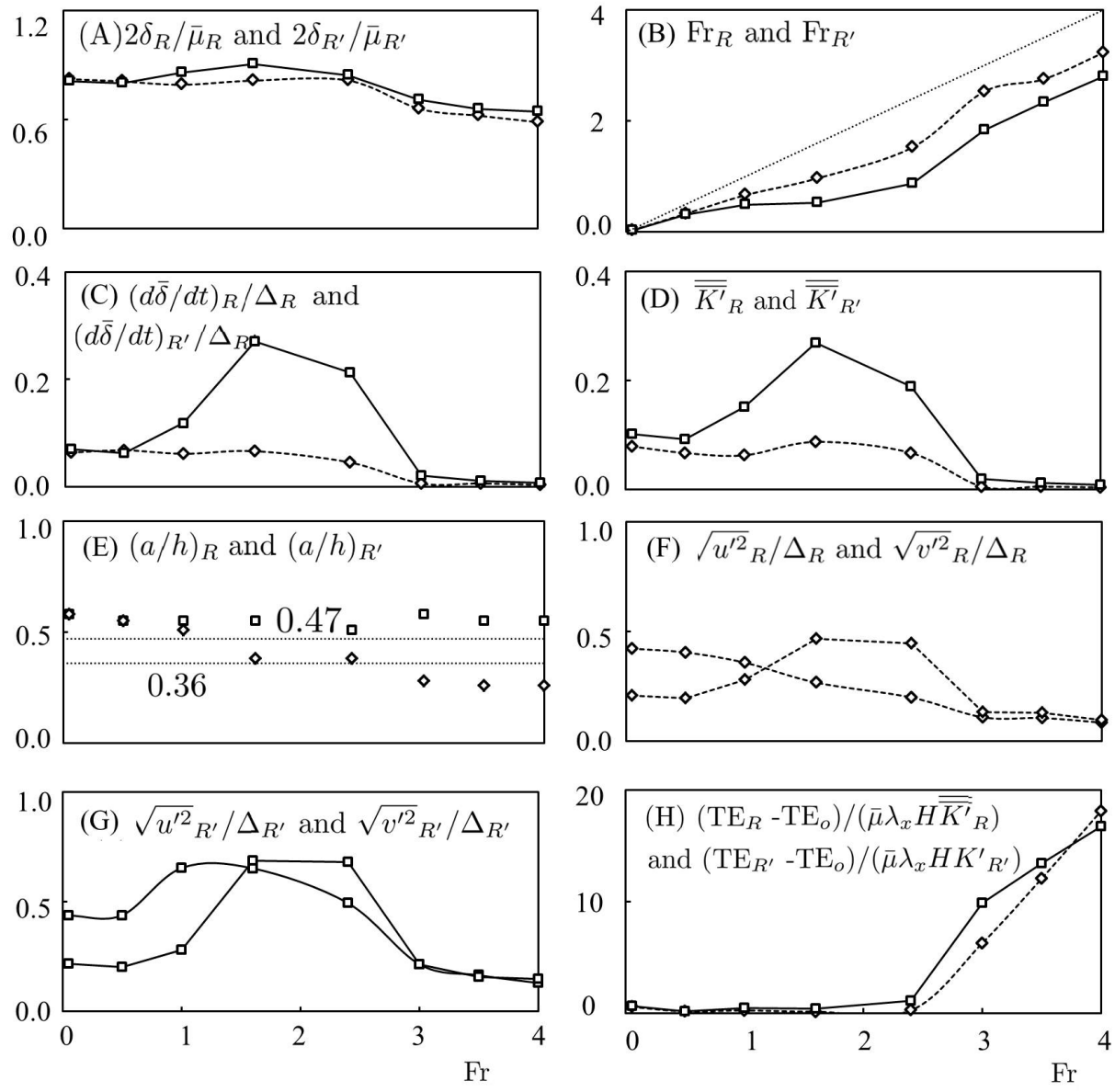

Figure 4–4: (A) width ratios, $2\delta_R/\bar{\mu}_R$ and $2\delta_{R'}/\bar{\mu}_{R'}$, (B) Froude numbers, Fr_R and $\mathrm{Fr}_{R'}$, (C) normalized spreading rates, $(d\bar{\delta}/dt)_R/\Delta_R$ and $(d\bar{\delta}/dt)_{R'}/\Delta_{R'}$, (D) disturbance's kinetic energies, $\overline{\overline{K'}}_R$ and $\overline{\overline{K'}}_{R'}$, (E) aspect ratios of the vortex streets, $(a/h)_R$ and $(a/h)_{R'}$, (F) rms values of u' and v' at the R-event, $\sqrt{u'^2}_R/\Delta_R$ and $\sqrt{v'^2}_R/\Delta_R$, (G) rms values of u' and v' at the R'-event, $\sqrt{u'^2}_{R'}/\Delta_{R'}$ and $\sqrt{v'^2}_{R'}/\Delta_{R'}$, (H) total energy dissipation, $(\mathrm{TE}_R - \mathrm{TE}_o)/(\bar{\mu}\lambda_x H\overline{\overline{K'}}_R)$ and $(\mathrm{TE}_{R'} - \mathrm{TE}_o)/(\bar{\mu}\lambda_x H\overline{\overline{K'}}_{R'})$. The diamond symbol denotes the R-event and the square symbol the R'-event. The dashed lines in (E) marks the 95% confidence interval for the aspect ratio of the mountain-wake vortex streets determined by Young and Zawislak (2006).

4.4 Vorticity Patterns

The distinction between the transitions, subcritical, trans-critical and supercritical transitions, is more clear on inspection of Figure 4–5. The pattern of the vorticity fluctuations $\zeta' = (\partial_x v' - \partial_y u')$ on the y-x plane are shown in the figure for the initial Froude number of (a) Fr = 0.05, (b) Fr = 0.5, (c) Fr = 1.0, (d) Fr = 1.6, (e) Fr = 2.4, (f) Fr = 3.0, (g) Fr = 3.5, (h) Fr = 4.0 at the dimensionless times ${t^*}_R = t_R \hat{U}_y$, ${t^*}_{R'} = t_{R'} \hat{U}_y$ and ${t^*}_S = t_S \hat{U}_y$. The subcritical transition (a) (b) (c) is the roll up of vorticity to form eddies that has definable vorticity center. The alternating positive and negative vorticity pattern is qualitatively similar to the Kármán vorticity street. The aspect ratio of the cross-stream and along-stream spacing of vortices for the subcritical cases is in the range between $a/h = 0.58$ and 0.26 as shown in Figure 4–4 (E). These values are remarkably consistent with the mean values of 0.42 and the 95% confidence values between 0.36 and 0.47, found in the island-wake vortex streets by Young and Zawislak (2006). The von Karman's invicid theory gives this aspect ratio a value of 0.28. The aspect ratios for supercritical transitions (f) (g) (h) are estimated although the vortex street is no longer discernible for these cases with the higher Froude number of Fr = 3.0, 3.5 and 4.0 when waves are interfering the organization of the vorticity to form the eddies. The island-wake vortex streets described by Young and Zawislak (2006) are essentially two-dimensional shear flow. The vertical motion of the island wakes is constrained by the density stratification in the atmosphere. The scale of the horizontal motion in the wake is large compared with the depth. The island wakes therefore are shallow flows and probably are dependent on some form of densimetric Froude number in a similar manner as in the eddies produced in the present simulations using the shallow water equations.

4.5 RMS Velocity Fluctuations

Figure 4–6 shows the root-mean-square (rms) of the velocity fluctuations $\sqrt{u'^2}/\Delta$ (solid lines) and $\sqrt{v'^2}/\Delta$ (dashed lines) at time $t = t_R$, $t = t_{R'}$ and time $t = t_S$. At low Froude number for the cases (a) (b) and (c), the jet/wake is dominated by the sinuous mode of

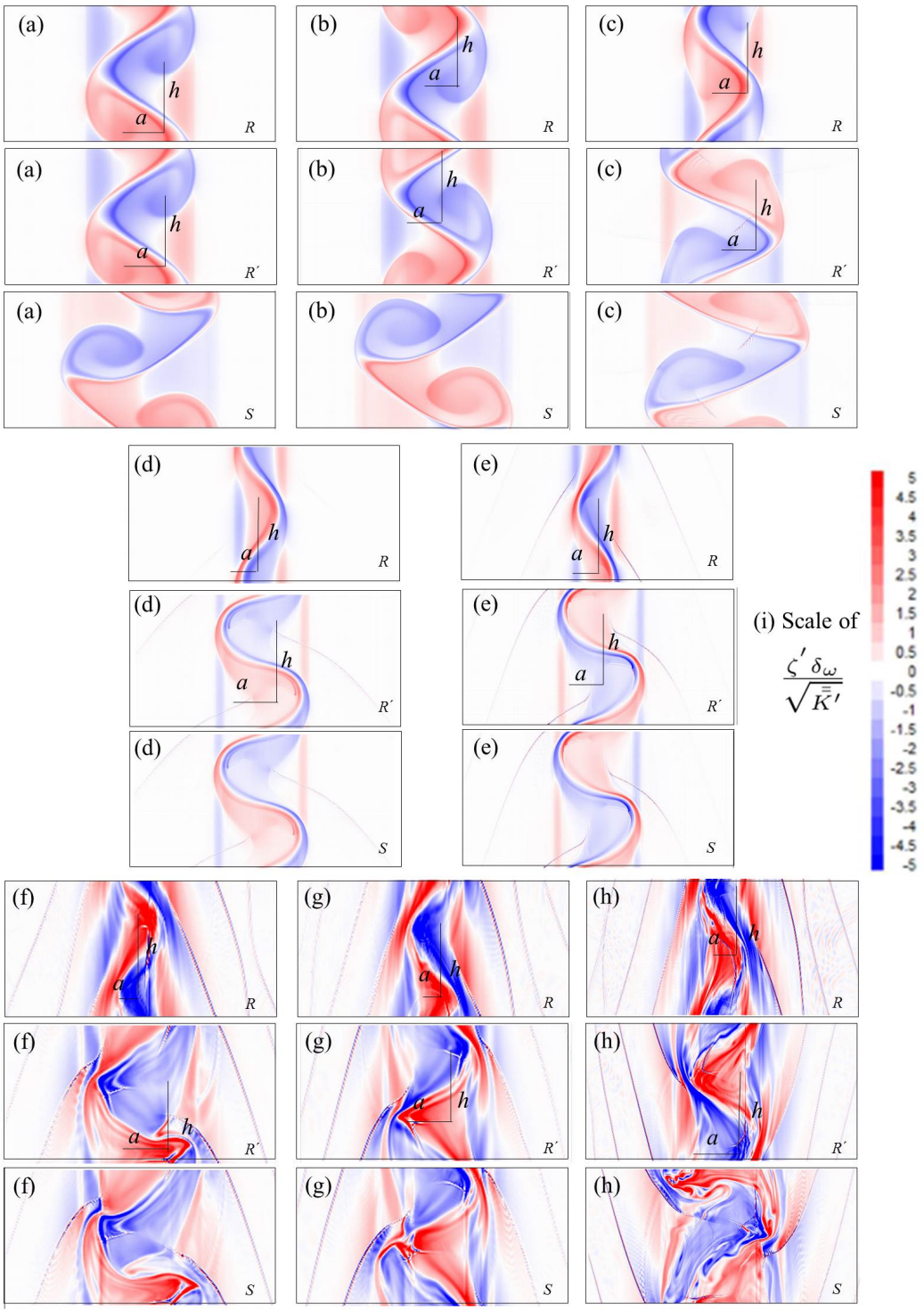

Figure 4–5: Patterns for vorticity fluctuations $\zeta^{'}\delta_\omega/\sqrt{\overline{K'}}$ on the y-x-plane for the initial Froude number (a) Fr = 0.05, (b) Fr = 0.5, (c) Fr = 1.0, (d) Fr = 1.6, (e) Fr = 2.4, (f) Fr = 3.0, (g) Fr = 3.5, (h) Fr = 4.0 at time $t^*_R = t_R\hat{U}_y$, $t^*_{R'} = t_{R'}\hat{U}_y$ and $t^*_S = t_S\hat{U}_y$. Scales for the normalized variables are given in (i). The aspect ratio of the cross-stream and along-stream spacing of vortices a/h and its dependence of the Froude number are summarized in Figure 4–4(E).

oscillations. The significantly greater value of the lateral component $\sqrt{v'^2}/\Delta$ compared with the longitudinal component $\sqrt{u'^2}/\Delta$ is due to the meandering of the jet/wake from side to side. The varicose mode progressively becomes more important at higher Froude number. The relative role of the two rms components $\sqrt{u'^2}/\Delta$ and $\sqrt{v'^2}/\Delta$, and their dependence on the Froude number is shown in Figure 4–4 (F) for the R-event and (G) for the R'-event. Again, the intensification of the fluctuations is observed in the trans-critical flow cases of (d) and (e). The fluctuation intensities are much reduced for the supercritical flow cases (f), (g) and (h) with higher Froude number.

4.5.1 Laboratory Experiments - Shallow Jets

Laboratory experiments for the jet/wake flows are rare. The turbulent plane jet experiments in shallow waters by Giger et al. (1991), Dracos et al. (1992) and Jirka (1994) are relevant comparisons with the simulations carried out for small Froude number. Figure 4–7 shows the longitudinal rms velocity profiles across the jet that correlates the $\sqrt{u'^2}/\Delta$ with y/δ. The diamond, triangle and square symbols are the laboratory data obtained by Giger et al. (1991). The solid line is the present simulation for (a) Fr = 0.05 with a Froude number comparable to the laboratory experiment. The small-scale turbulence from the secondary instability - which is part of the fully developed turbulent flow in the laboratory - can not be reproduced from the present numerical simulation. The simulation rms velocity fluctuation profiles therefore are not expected to be exactly comparable to the laboratory data. However, the simulation profile in Figure 4–7 is consistent, in the sense that the laboratory data have similar shape of the twin peaks. Most remarkably, the peak value of $\sqrt{u'^2}/\Delta \simeq 0.2$ in the simulated profile is equal to the peak observed in the corresponding laboratory profiles. Another aspect of the shallow jet is its spreading rate. The spatial rate of the half-width δ from the laboratory experiment of Dracos et al. (1992) is approximately $d\delta/dx \simeq 0.1$. Assuming an advection velocity of the dominant eddies to be $dx/dt = 0.7\Delta$, the spatial

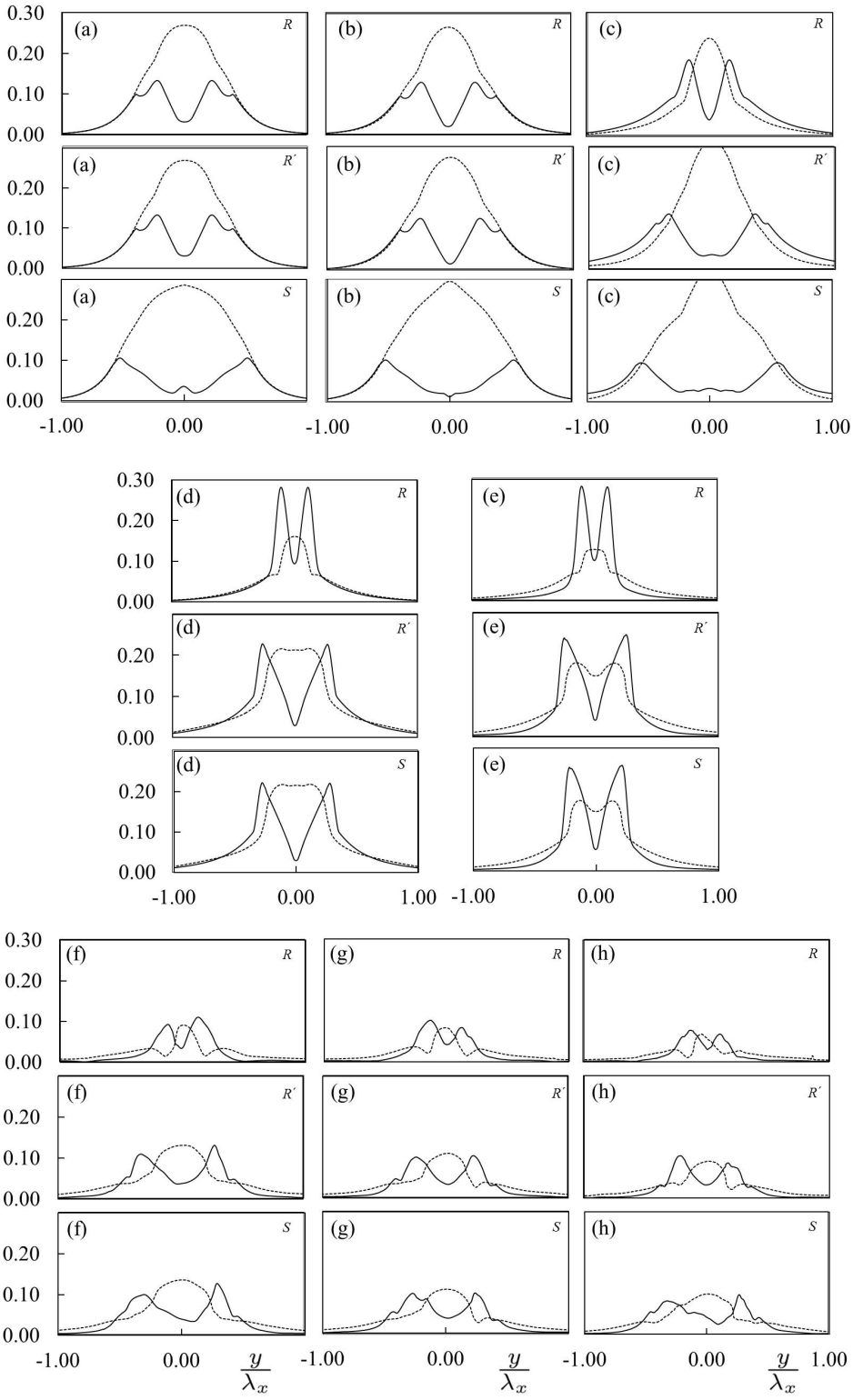

Figure 4–6: Mean profile for the rms values of $\sqrt{u'^2}/\Delta_o$ (solid lines) and $\sqrt{v'^2}/\Delta_o$ (dashed lines) at time $t = t_R$, $t = t_{R'}$ and time $t = t_S$ for the initial Froude number (a) Fr = 0.05, (b) Fr = 0.5, (c) Fr = 1.0, (d) Fr = 1.6, (e) Fr = 2.4, (f) Fr = 3.0, (g) Fr = 3.5, (h) Fr = 4.0.

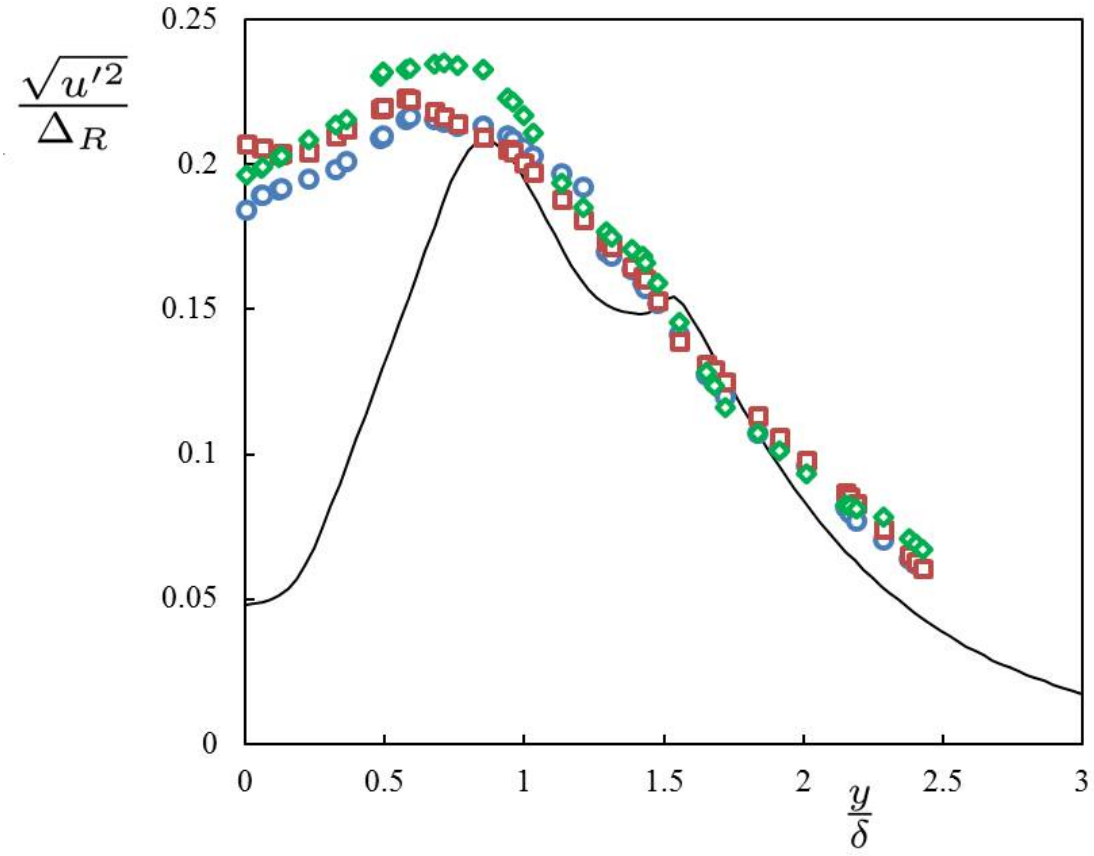

Figure 4–7: The rms profiles of the shallow jet - laboratory data compared with the simulation of the subcritical transition (a) Fr = 0.05 and $k_x = 1.0$, at time $t = t_R$ (solid line). The square symbols are at $X/H = 10$; the circular symbols are at $X/H = 14$; the diamond symbols are at $X/H = 18$ from laboratory experiment in Giger et al. (1991).

spreading rate is then estimated to have the temporal rate as follows:

$$\frac{d\delta}{dt} = \frac{d\delta}{dx}\frac{dx}{dt} \simeq 0.1 \times 0.7\Delta = 0.07\Delta \tag{4.14}$$

This estimated temporal rate from the laboratory experiments with a small Froude number is comparable to the spreading rate during the transition shown in Figure 4–4 (C).

4.6 Wave Effect and Energy Dissipation

Figure 4–8 shows the free-surface elevation fluctuation profiles at the three time event R, R' and S. These profiles are functions of x and y. The dimensionless depth fluctuations $\frac{gh'}{\sqrt{\bar{\bar{K'}}}\sqrt{gH}}$ are plotted versus y/λ_x for $x = 1/4\lambda_x$, $x = 1/2\lambda_x$,$x = 3/4\lambda_x$,and $x = \lambda_x$. Sudden changes in depth in the form of shock waves (hydraulic jumps) are observed in the trans-critical flow (d) and (e) and supercritical flow (f) (g) and (h), when the convective Froude number is greater than the value of unity. The wave radiation away from the transition is particularly prominent in the supercritical flow. These shock waves of significant amplitude with sudden change in depth and velocity are observed to radiate away from the transitions. The local energy dissipation and the radiation of the wave energy from the shock waves are calculated from the simulations. The total energy include the energy of the mean flow, over the entire computational domain is

$$\mathrm{TE} = \int_{\mathrm{y^-}}^{\mathrm{y^+}} \int_{\mathrm{o}}^{\lambda_\mathrm{x}} (\frac{1}{2}u^2 + \frac{1}{2}v^2 + \frac{1}{2}gh)h \; dxdy \tag{4.15}$$

This mimus the initial energy associated with the SECH profile, (TE-TE$_o$), is the energy losses due to local dissipation and radiation. The dimensionless variable for the energy losses relative to the disturbance kinetic produced is (TE-TE$_o$)/($\bar{\mu}\lambda_x H\overline{\overline{K'}}$). The time series of this energy losses is shown in the last row in Figure 4–3. Figure 4–4 (H) shows the dependence of this energy losses, associated with the R-event and R'-event, on the Froude number. The losses is negligible for the sub-critical flow case but is huge for supercritical flow. For the supercritical flow (h) Fr = 4.0, the work needed for the energy losses are about 18 time greater

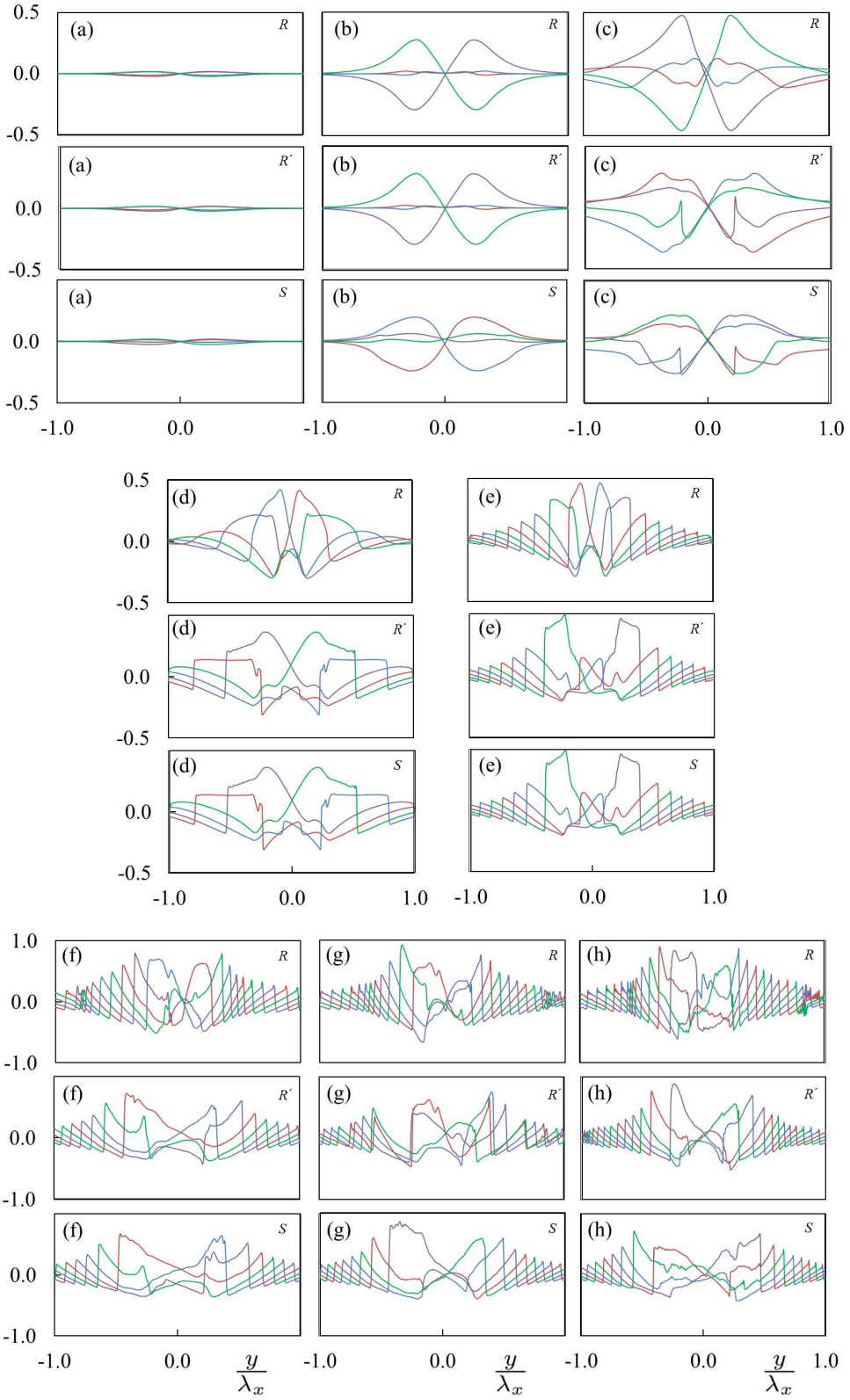

Figure 4–8: The normalized depth fluctuation profiles for $gh'/(\sqrt{gH}\sqrt{\overline{\overline{K'}}})$ with y at $x = \frac{1}{4}\lambda_x$, $x = \frac{2}{4}\lambda_x$, $x = \frac{3}{4}\lambda_x$, and $x = \lambda_x$.

than the disturbance kinetic energy produced. The energy losses in trans-critical flow is one order of magnitude greater the losses in sub-critical flow. The losses in supercritical flow is another order of magnitude greater. It is clear that the waves have the most prominent role in the supercritical flow.

4.7 Conclusion

The direct numerical simulations of the jet/wake transition to turbulence have produced results that are consistent with the fully developed turbulent plane jets data obtained in the laboratory and the visualization of the island wakes in the atmosphere. The reduction in the exchanges for the supercritical flow is anticipated due to the huge energy dissipation and radiation by the waves. The intensification of the disturbance energy and the spreading rate in the trans-critical flow however is unexpected. Laboratory experimental data are not available for the trans-critical and supercritical transition. Therefore, further studies in the laboratory are necessary to confirm, in particular, the unexpected results found in the trans-critical flow transition.

CHAPTER 5

CONVERGENCY STUDY

Grid refinement study has to be conducted for direct numerical simulations to show the simulated results are not dependent on the mesh size. A series of grid refinement calculations has been carried out to confirm the linear growth rate of the instabilities by WENO scheme. Calculations are performed for different grid points across one wavelength, that is N = 32, 64, 128, 256 and 512 points. The convergence of the maximum linear growth rate $\hat{\alpha}$ is studied and correlated with the number of points over one vorticity thickness $\delta_{\omega_o}/\Delta_x$ for different grid sizes.

The order of convergence as the grid is refined is determined from the procedure outlined by Stern et al. (2001). For a group of three values $\hat{\alpha}_{k-1}$, $\hat{\alpha}_k$, and $\hat{\alpha}_{k+1}$ obtained from the simulation at different grid sizes, k denotes the number of grid points, the order of convergence P_k is

$$P_k = \frac{1}{\ln r} \ln [\frac{\hat{\alpha}_{k+1} - \hat{\alpha}_k}{\hat{\alpha}_k - \hat{\alpha}_{k-1}}] \quad \text{where} \quad r = \frac{\hat{\alpha}_k}{\hat{\alpha}_{k+1}} \tag{5.1}$$

The estimated true value from the extrapolation is

$$\hat{\alpha}_{\text{true}} = \frac{r^{P_k}\hat{\alpha}_{k+1} - \hat{\alpha}_k}{r^{P_k} - 1} \tag{5.2}$$

Knowing the estimated true value, the estimated fractional error (FE) is then computed by

$$\text{FE}(\%) = \frac{|\hat{\alpha} - \hat{\alpha}_{\text{true}}|}{\hat{\alpha}_{\text{true}}} \times 100 \tag{5.3}$$

Table 5–1 shows the values of growth rate and fractional error of for Fr = 1.6 and Fr = 2.4 at the maximum wave number $k_x = 0.5$. Table 5–2 tabulates the results of the grid refinement study of supercritical flows of Fr = 4.0 at five different k_x values . The graphs of

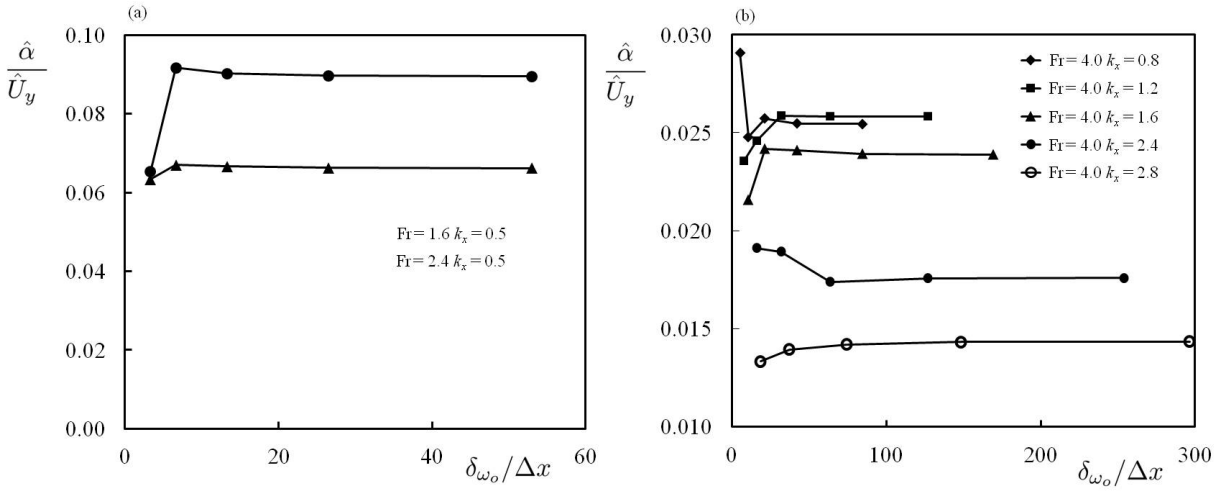

Figure 5–1: (a) Grid refinement of full jet simulation for Fr = 1.6 $k_x = 0.5$ and Fr = 2.4 $k_x = 0.5$ and (b) Fr = 4.0 $k_x = 0.8, 1.2, 1.6, 2.4, 2.8$

maximum growth rate against the number of grid point over one vorticity thickness δ_ω are shown in Figure 5–1.

The WENO scheme performs very well. The error of the computation is quite acceptable in the present simulation for N = 128 and 256 nodes over the wavelength between the periodic boundary conditions. In the full jet simulations, the results obtained with N = 128 give an accuracy of three significant figures. The simulations with N = 256 have an accuracy of four significant figures. N = 512 point result is almost identical with the extrapolated exact solution. Because of the computational efficiency, all the results in Chapter 3 are from N = 256 simulations. The resulting graph of the fractional error as refining the grid is presented in Figure 5–2.

The convergency study of the non-linear part of the instability analysis is demonstrated by calculating the first peak of the maximum kinetic energy. The exact solution is extrapolated based on three grid sizes of N = 64 , 128, and 256. Table 5–3 presents the results for three typical case corresponding of the flow in the subcritical, trans-critical and supercritical stage. The WENO scheme also performs very well as the error is approximately 0.1% as shown in Figure 5–3. The results of N = 256 are also reliable because it almost matches with the exact solutions. Therefore, the results in Chapter 4 are from N = 256 simulations.

Table 5–1: Grid size, fractional error and order of convergence for full jet simulation (sinuous mode) of Fr = 1.6, $k_x = 0.5$ and Fr = 2.4, $k_x = 0.5$

Case Number	N	$\delta_{\omega_o}/\Delta x$	$\hat{\alpha}/\hat{U}_y$	FE(%)	Order
		Fr = 1.6 k_x=0.5			
1	32	3.310	0.065401	26.8479	
2	64	6.619	0.091711	2.5806	-4.08
3	128	13.239	0.090152	0.8367	1.59
4	256	26.477	0.089632	0.2556	1.71
5	512	52.954	0.089474	0.0781	
Exact	∞	∞	0.089404	0	
		Fr = 2.4 k_x=0.5			
1	32	3.310	0.063391	1.1965	
2	64	6.619	0.067071	1.3657	-3.10
3	128	13.239	0.066642	0.7171	0.26
4	256	26.477	0.066285	0.1764	2.02
5	512	52.954	0.066196	0.0434	
Exact	∞	∞	0.066168	0	

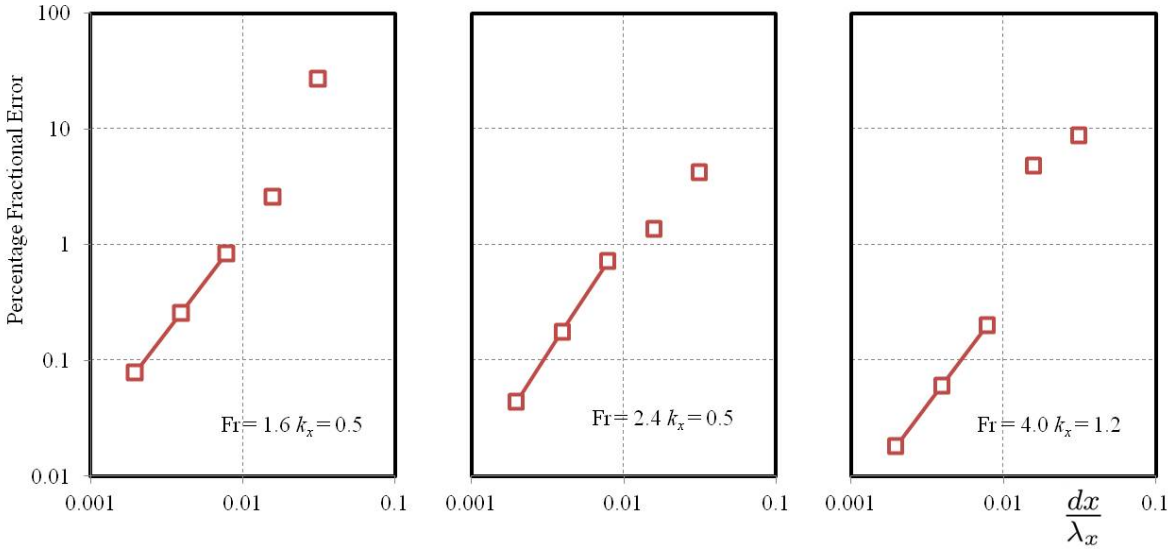

Figure 5–2: Fractional error in percentage the growth rate of the full jet simulation of Fr = 1.6 k_x=0.5, Fr = 2.4 k_x=0.5, and Fr = 4.0 k_x=1.2

Table 5–2: Grid size, fractional error and order of convergence for full jet simulation (varicose mode) of Fr = 4.0 k_x = 0.8, 1.2, 1.6, 2.4 and 2.8

Case Number	N	$\delta_{\omega_o}/\Delta x$	$\hat{\alpha}/\hat{U}_y$	FE(%)	Order
		Fr = 4.0 k_x=0.8			
1	32	5.295	0.029050	14.1782	
2	64	10.591	0.024785	2.5872	-2.18
3	128	21.182	0.025724	1.1041	-1.83
4	256	42.364	0.025460	0.0661	4.06
5	512	84.727	0.025444	0.0040	
Exact	∞	∞	0.025443	0	
		Fr = 4.0 k_x=1.2			
1	32	7.943	0.023575	8.7124	
2	64	15.886	0.024583	4.8121	0.36
3	128	31.773	0.025877	0.2002	-5.16
4	256	63.545	0.025841	0.0600	1.74
5	512	127.091	0.025830	0.0180	
Exact	∞	∞	0.025825	0	
		Fr = 4.0 k_x=1.6			
1	32	10.591	0.021563	9.6956	
2	64	21.182	0.024175	1.2412	-5.47
3	128	42.364	0.024116	0.9946	1.82
4	256	84.727	0.023908	0.1237	3.01
5	512	169.454	0.023882	0.0154	
Exact	∞	∞	0.023879	0	
		Fr = 4.0 k_x=2.4			
1	32	15.886	0.019097	8.5999	
2	64	31.773	0.018937	7.6900	3.28
3	128	63.545	0.017386	1.1310	-3.06
4	256	127.091	0.017572	0.0697	4.02
5	512	254.181	0.017584	0.0043	
Exact	∞	∞	0.017585	0	
		Fr = 4.0 k_x=2.8			
1	32	18.534	0.013330	6.9646	
2	64	37.068	0.013935	2.7456	1.21
3	128	74.136	0.014197	0.9167	1.09
4	256	148.272	0.014320	0.0579	3.99
5	512	296.545	0.014327	0.0037	
Exact	∞	∞	0.014328	0	

Table 5–3: Grid size, fractional error and order of convergence of the first peak of turbulent kinetic energy for full jet simulation of Fr = 0.5 k_x=1.0, Fr = 2.4 k_x=0.5, and Fr = 4.0 k_x=1.2

Case Number	N	$\delta_{\omega_o}/\Delta x$	$\hat{K}'/\Delta^2$	FE(%)	Order
		Fr = 0.5 k_x=1.0			
1	64	13.239	0.07717	0.8624	
2	128	26.477	0.07773	0.1401	
3	256	52.954	0.07782	0.0228	2.62
Exact	∞	∞	0.07784	0	
		Fr = 2.4 k_x=0.5			
1	64	6.619	0.06498	6.9500	
2	128	13.239	0.06935	0.6665	
3	256	26.477	0.06973	0.1083	3.49
Exact	∞	∞	0.06981	0	
		Fr = 4.0 k_x=1.2			
1	64	15.886	0.00502	1.7964	
2	128	31.773	0.00591	0.5272	
3	256	63.545	0.00622	0.0856	1.52
Exact	∞	∞	0.00628	0	

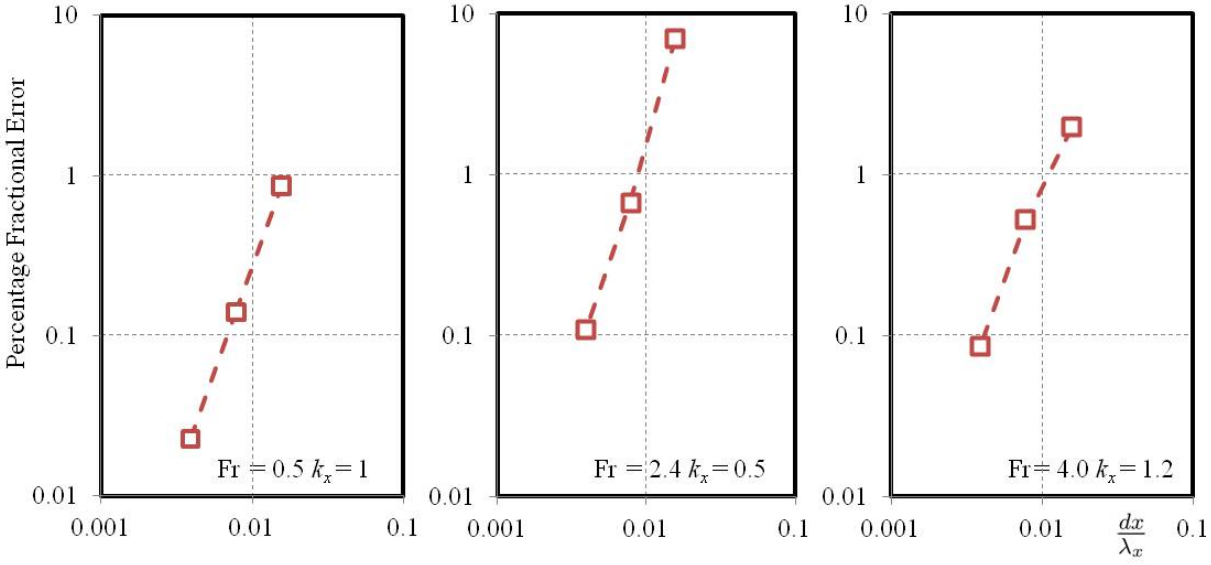

Figure 5–3: Fractional error in percentage of the first peak of the turbulent kinetic energy of the full jet simulation of Fr = 0.5 k_x=1.0, Fr = 2.4 k_x=0.5, and Fr = 4.0 k_x=1.2

CHAPTER 6

EXPERIMENTAL STUDY OF THE EXCHANGE PROCESS BETWEEN THE MAIN FLOW AND ITS SIDE BASIN

6.1 Introduction

6.1.1 Mass Exchange Process in the Basin

The study of mass and momentum exchange between the main flow and its side basins has many important engineering applications. For example, the spur dikes in Figure 6–1(a) are constructed as river training structures to protect erosion. The river stream is considered as shallow flow since the depth is much smaller than the width. The main stream enters and exits into the dike causing the exchange process. Recirculating flow regions are observed inside the spur dikes and sediments or pollutants could be trapped due to locally low velocity. The rate of the mass exchange between the spur dikes and the main river is an important parameter used to describe this exchange process.

The exchange process for the supercritical flows is as important as the exchange process in subcritical flows. A fish ladder in Figure 6–1(b) is built as an ancillary structure of a dam to facilitate fish to swim back to the upstream fish hatchery. The fish tends to swim against the supercritical main flow and rests inside the chamber to pass the dam. The fish ladder is constructed along a steep slope and consists of several chambers. The main flow velocity is higher than the recirculation velocity inside the chambers.

6.1.2 Shear Flow in Shallow Open Channels

Pinilla and Chu (2008, 2009 a,b) and Chu (2010) have studied numerically the role of gravity-wave radiation on the development of shear flow in shallow open channels. Figure 6–2 shows their simulations of the shear instabilities of a hyperbolic tangent velocity profile for

(a) Spur dikes, Yellow River, China (b) Fish ladders, Columbia River, US

Figure 6–1: (a) Spur dikes in the Yellow River, China to protect erosion. (b) Fish ladders in Columbus River, USA built next to a dam

three different convective Froude numbers: (a) $\mathrm{Fr_c} = 0.4$ (b) $\mathrm{Fr_c} = 0.8$ and (c) $\mathrm{Fr_c} = 1.2$. The columns on the left-hand side of the figure show the velocity vectors and the columns on the right-hand side show the dilation. The evolution of a small disturbance with time eventually leads to large scale lateral exchanges between the two sides of the shear flow of different velocities. At low convective Froude number when $\mathrm{Fr_c} = 0.4$, the mass and momentum exchanges as shown in Figure 6–2(a) are characterized by the formation of the turbulent eddies. At high convective Froude number when $\mathrm{Fr_c} = 1.2$ as shown in Figure 6–2(c), the exchanges are characterized by the radiation of gravity wave and the less energetic sliding shocklets. The radiation of gravity waves from the shocklets has reduced the instability and suppressed the mass exchanges across the shear layer.

Similar dependence of the shear instability on the convective Froude number is obtained from the linear stability analysis using the normal mode approach as shown in Figure 6–3. For the hyperbolic tangent base velocity profile, the exponential growth rate α_{max} decreases with the convective Froude number $\mathrm{Fr_c}$. This dependence on the convective Froude number for the shear flow in open channels is analogous to the shear instability of compressible gas dynamics. The lines for Mach number Ma = 0.01, 0.4, 0.8 and 1.2 in Figure 6–3 are

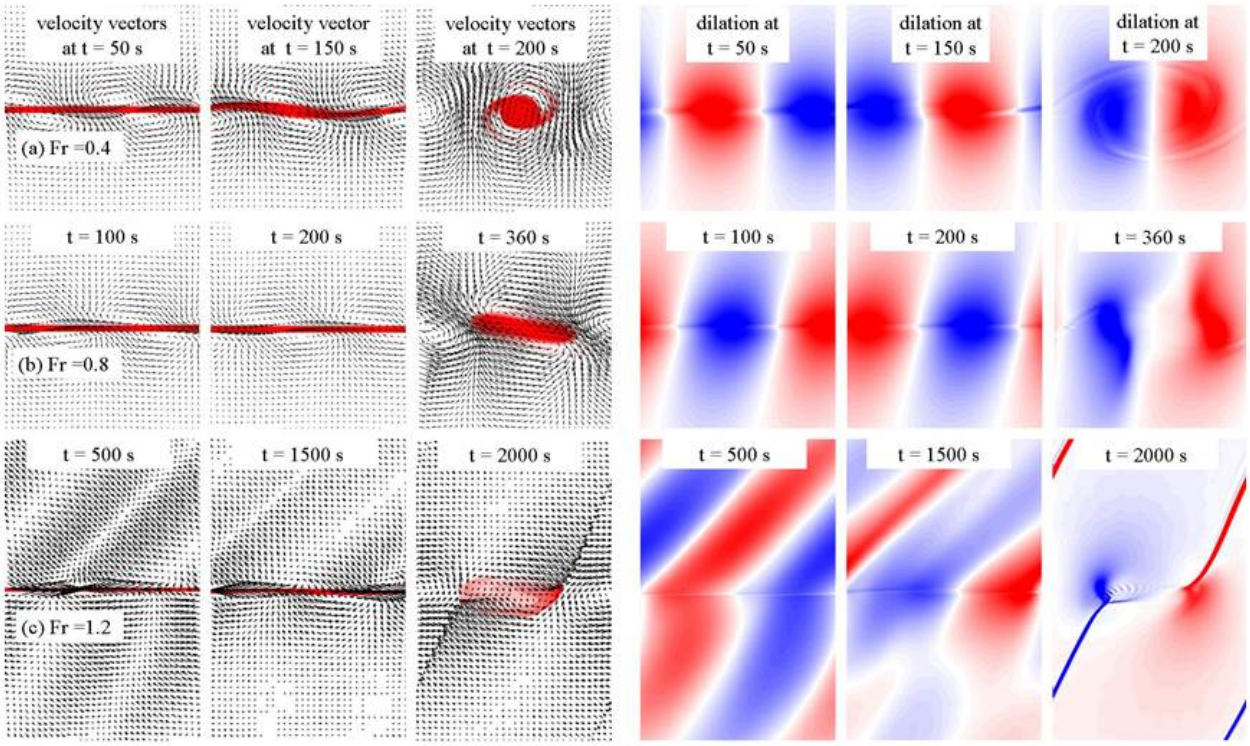

Figure 6–2: Development of shallow shear flow of hyperbolic-tangent velocity profile for three convective Froude numbers; (a) $\mathrm{Fr_c} = 0.4$, (b) $\mathrm{Fr_c} = 0.8$ and (c) $\mathrm{Fr_c} = 1.2$. The three left-hand columns show the velocity vectors and the rollup of a thin layer of dye between the shear flows moving in opposite directions. The three right-hand columns show the dilation of the depth-averaged velocity. Radiation of gravity waves characterizes the shear flow of large convective Froude number $\mathrm{Fr_c} = 1.2$ in (c)

instability calculations obtained for ideal gas by Sandham and Reynolds (1990). The gravity-wave radiation from the shear flows in open channels has the similar effect on instability as the radiation of the sound from the shear layer in compressible gas.

Figure 6–4 shows another shear-flow exchange between an open-channel flow with one side basins for three different Froude numbers. The shear layer in the subcritical main flow of Froude number $\mathrm{Fr_c} = 0.2$ is shown in Figure 6–4(a). For comparison, the cases of the supercritical main flow with $\mathrm{Fr_c} = 1.5$ and 3.5 are shown in Figure 6–4(b) and (c), respectively. The impingement of the mixing layer on the downstream corner generates the recirculating flow in the basin. The level of the turbulence energy defines the contours in the figure. It is clear the turbulent energy is concentrated in the mixing layer between the main

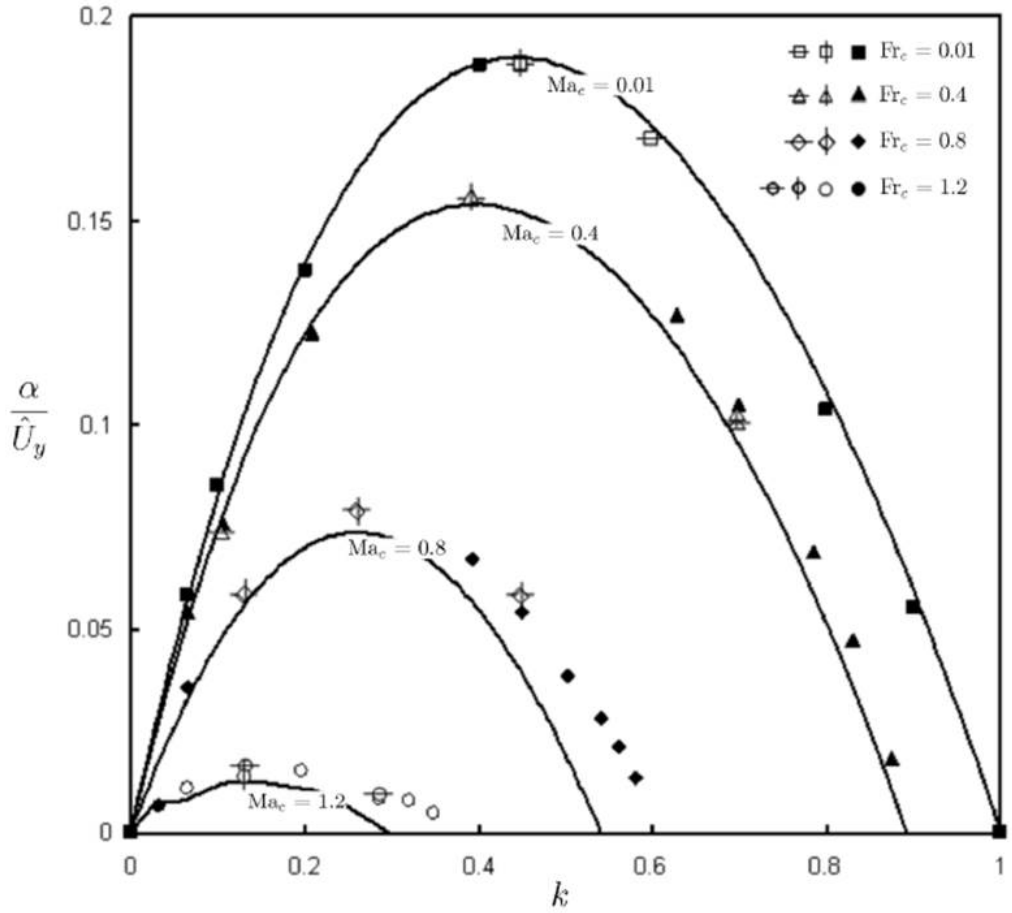

Figure 6–3: Exponential growth rate α of the unstable shear flow of the classical hyperbolic tangent velocity profile. Its dependence on the convective Froude number $\mathrm{Fr_c}$ is analogous to the dependence of the rate on the convective Mach number $\mathrm{Ma_c}$ in the compressible shear flow

flow and the recirculating flow in the basin. The subcritical mixing layer characterized by formation of eddies in the mixing layer as shown in Figure 6–4(a) is significantly greater in thickness when compared with the supercritical mixing layer shown in Figure 6–4(c). The recirculating flow associated with the subcritical mean flow is also more energetic comparing with that associated with the supercritical mean flow. These comparisons between the subcritical and supercritical shear flow are consistent with the conclusion from the stability analysis by Pinilla and Chu (2008, 2009 a,b) and the direct numerical simulation of the turbulent flow by Chu (2010).

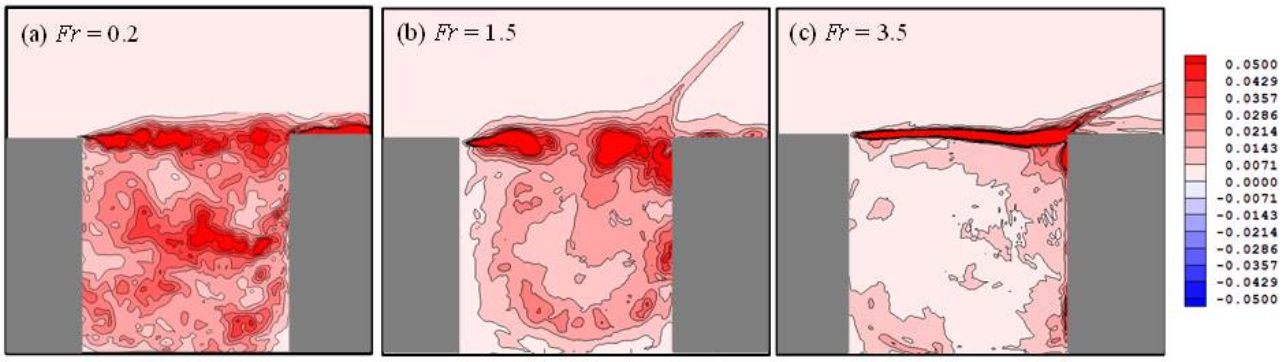

Figure 6–4: The normalized turbulence kinetic energy distribution associated with flow in the square basin for Froude number (a) $Fr_c = 0.2$, (b) $Fr_c = 1.5$ and (c) $Fr_c = 3.5$

6.1.3 Scope of Current Investigation

The laboratory experiments are performed to support the development of turbulence model for both subcritical and supercritical flows. Most of the existing laboratory works are done in subcritical flow only. The current experiments are aiming to the supercritical flow and are revealing the difference between the subcritical and supercritical exchange. The experiments cover a wide range of Froude numbers Fr from Fr = 0.48 to Fr = 2.92. Red dye was injected into the basin and the experiments were filmed by a video camera with the frame rate of 30 frames per second. A video imaging method was employed to measure the dye concentration. The accumulation and retention times of the dye in the side basin are determined as the parameters to characterize the exchanges.

6.2 Experimental Method

6.2.1 Experimental Set up

The mass and momentum exchanges across the shear flow are investigated in the laboratory in a 217 cm long and 35.5 cm wide water table. The channel bottom could be flat or tilted with a slope. The experimental setups are shown in Figure 6–5 (a) and (b) for the subcritical flow and supercritical flow experiments, respectively. In subcritical experiments,

the flow enters the channel directly from the upstream stilling basin while in supercritical experiments, a square reservoir is created upstream and separated from the channel by a sluice gate. The supercritical flow is created by changing the water depth in the reservoir. A square side basin with dimension L = 24 cm x 24 cm is attached along the side of the main open channel at 96 cm upstream from the flow entrance to allow flow exchange. During the experiments, red dye (Triactive Red DF-6BL New) of concentration c_o as the tracer at a rate of q_o is injected into the channel from the injection point on the upstream edge of the basin for flow visualization. Figure 6–6 shows the close-up of the basin and the main channel, and the flow circulates in the basin in counterclockwise direction. The experiment is filmed by a video camera hanging directly above the channel with the zoom focusing to the basin. The tests are conducted for supercritical flows of Froude number Fr = 2.92, 1.69, 2.45, 2.14 and subcritical flows of Froude number Fr = 0.48 and 0.55 on the channel slopes of S_o = 0 and 0.3%, respectively. The test conditions including water depth h and velocity U in the main channel are summarized in Table 6–1.

Table 6–1: Experiment conditions

Experiment No.	Fr	S_o	U(m/s)	mean depth (cm)	c_o (mg/L)	q_o (ml/s)
E1	0.55	0	0.33	3.70	1000	0.444
E2	0.48	0	0.28	3.50	5000	0.444
E3	2.92	0.3%	1.21	1.74	1000	0.396
E4	1.69	0.3%	0.73	1.87	1000	0.520
E5	2.45	0.3%	1.02	1.77	4000	0.323
E6	2.14	0.3%	0.87	1.69	4000	0.415

6.2.2 Video Imaging Method

The measurement of the dye concentration in the basin was based on a video imaging method developed by Zhang and Chu (2003). The dye concentration can be determined as a function of light intensity which could be determined from analysing the images produced by the video camera. Each image contains 1440*1080 pixels and in each pixel there are

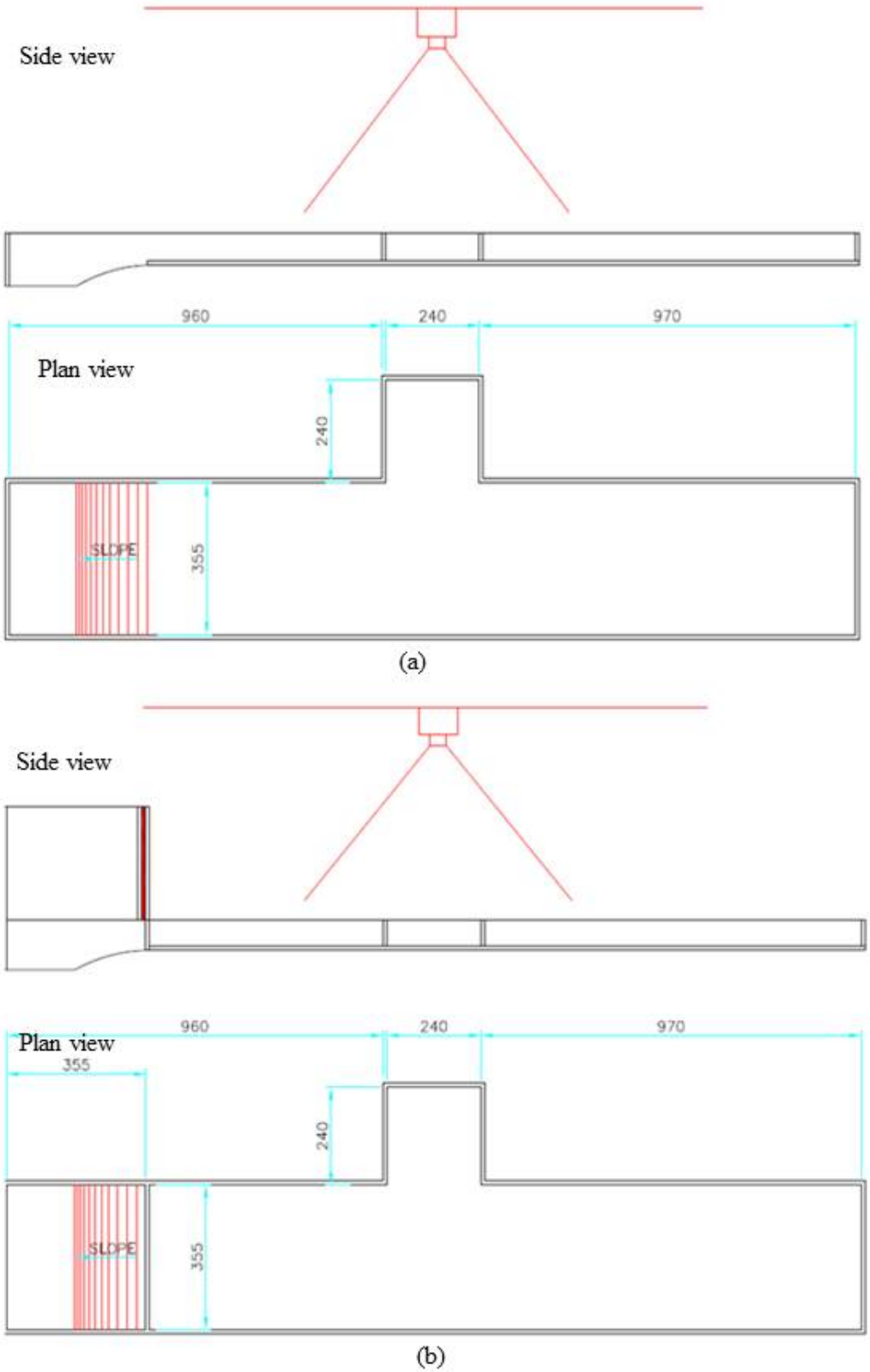

Figure 6–5: Side view and plan view of experiment apparatus (a) subcritical experiments (b) supercritical experiments

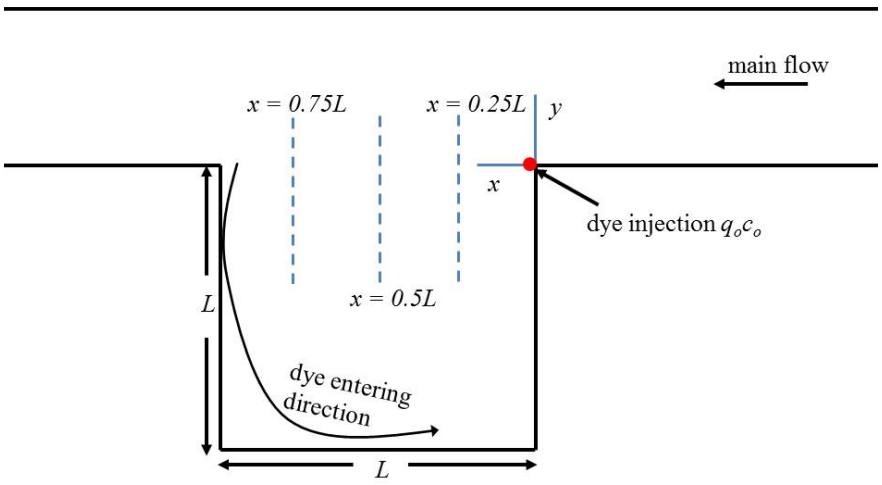

Figure 6–6: Close-up of the basin showing the dye entraining direction

three numbers (R,G,B) telling the three basic color, red, green and blue color intensity. This number is an integer from 0 to 255. 0 means minimum intensity while 255 means maximum intensity of the corresponding color. The combination of the three numbers gives any color as seen in the image. The injection of the red dye in the basin of depth h reduced the intensity of both green and blue light as shown in Figure 6–7 while red light intensity is kept the same. The percentage of the green light intensity reduction p was calculated for each pixel by

$$p = 1 - \frac{G}{G_o} \tag{6.1}$$

G is the green color intensity of the image and G_o is the green color intensity of the background. The background is the clean water image in the basin before the injection of the dye. As the lighting conditions on the flow is not entirely uniform and unavoidable shake of the camera during the experiment, the aperture of the video camera might not be kept at the same value during the experiment. As a result, further adjustment is needed to adjust the camera aperture by

$$p = 1 - \frac{G}{G_o} \times \frac{G_{oc}}{G_c} \tag{6.2}$$

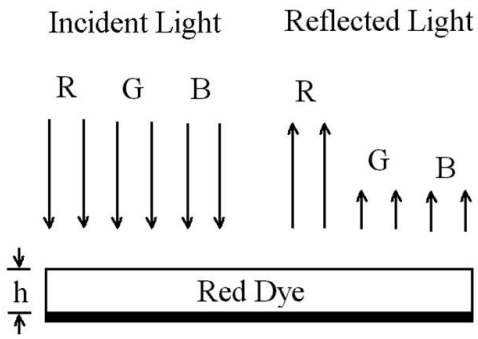

Figure 6–7: Absorption of green and blue light due to the presence of red dye in the open-channel flow of depth h.

Figure 6–8: Experiment image background image and processed image by removing the background

where G_c is the green color intensity of the image and G_{oc} is the green color image of the background at the same location of the clear water outside the basin where no dye is presented in this area.

The image processing is illustrated in Figure 6–8. The processed image is obtained by subtracting the background image from the original image at every pixel of the image. The processed image could show the movement of the dye and the development of the boundary layer more clearly.

Table 6–2: Calibration data for all experiments

Concentration(mg/L)	p (E1)	p (E2)	p (E3,E4)	p (E5,E6)
25.0	0.6500	0.7090	0.5523	0.5141
12.5	0.6039	0.6562	0.4265	0.3937
6.25	0.4910	0.5443	0.2945	0.2726
3.125	0.3488	0.3992	0.1960	0.1704
1.5625	0.2357	0.2823	0.1158	0.1039
0.78125	0.1392	0.1767	-	-
0	0.0000	0.0000	0.0000	0.0000

6.2.3 Data Calibration

A calibration curve is needed to correlate the dye concentration to green light intensity reduction p. The calibration has to be conducted before each experiment by keeping the same light condition as the experiment. The pre-determined concentration solutions were dumped into the calibration box which has the same dimension as the basin. Since the percentage of reduction p depends on water depth, the water depth inside the basin during the experiment is measured and then used as the calibration depth to ensure the same volume of water in the basin during the experiment and in the calibration box. The same lighting condition is also kept in calibration and during the experiment.

The preparation of the calibration concentration solution is done by dilution. The first sample to start the dilution is 25 mg/L dye solution. The subsequent samples are done by dilution the previous sample by half. The process of preparing calibration samples are then filmed and the percentage of green light reduction p is determined. Table 6–2 shows the calibration data and Figure 6–9 shows the calibration curves for all the experiments.

The calibration data are fitted with a smooth polynomial with the equation in the following form. $a_1, a_2, a_3, a_4, a_5, a_6$ are constants and their values are shown in Table 6–3.

$$c = a_1 p + a_2 p^2 + a_3 p^3 + a_4 p^4 + a_5 p^5 + a_6 p^6 \tag{6.3}$$

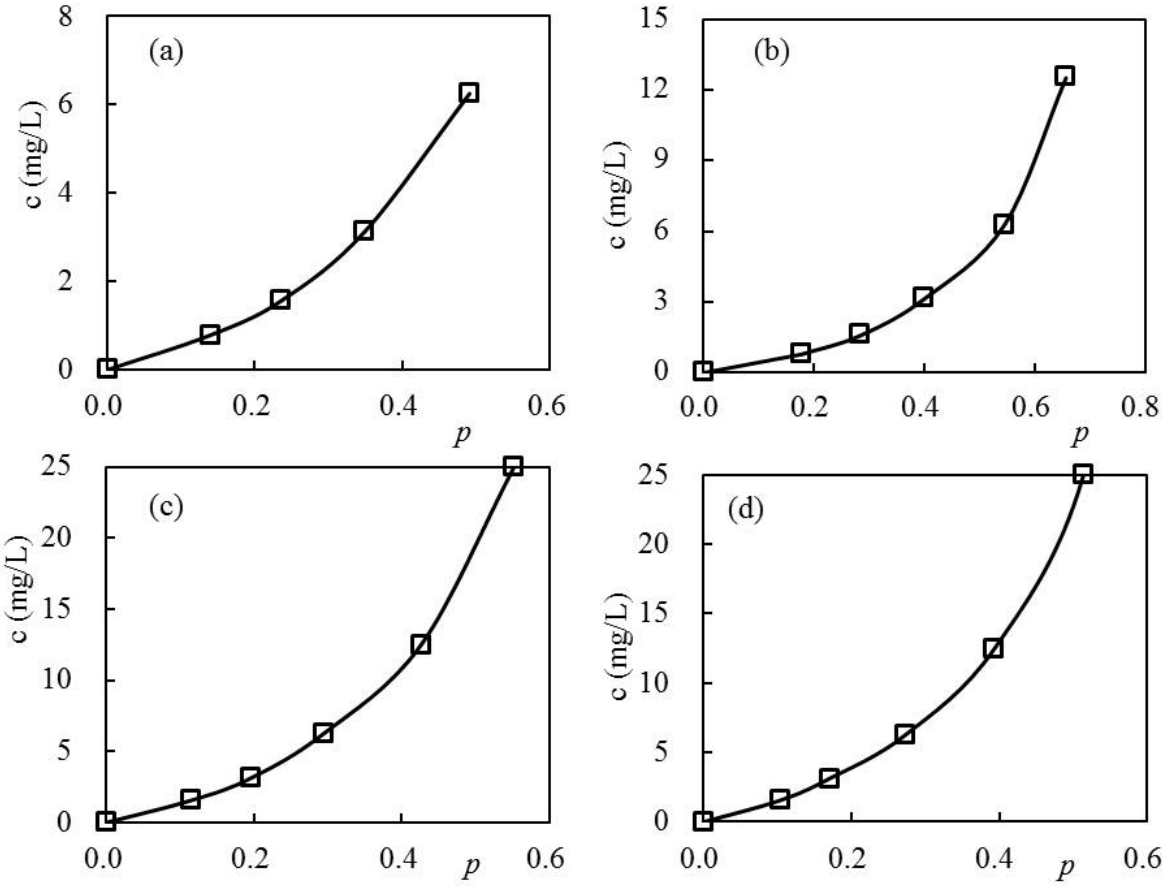

Figure 6–9: Calibration curves for all the experiments (a) E1 (b) E2 (c) E3 and E4 (d) E5 and E6

Table 6–3: The coefficient for each calibration curves

Constant	E1	E2	E3, E4	E5, E6
a_1	4.6596	-5.5185	20.982	-13.206
a_2	1.7958	88.066	-162.55	636.83
a_3	29.836	-234.60	1106.2	-5148.4
a_4	0	239.85	-2497.3	19885
a_5	0	0	2121.1	-35168
a_6	0	0	0	23456

6.3 Experimental Results

6.3.1 Dye Entrainment Mechanism

Figure 6–10, 6–11 and 6–12 show the processed images of the start of dye accumulation for Froude number 0.48, 2.45 and 2.92. The time interval between adjacent image is 0.5 s. There is a recirculating eddy observed in the subcritical images Fr = 0.48. The dye enters the basin from the downstream edge of the basin and rotates counterclockwise. The dye gets into the basin from the outer core progressively into the inner core. The eddy is well defined and the roll up of the eddy is the feeding mechanism of the dye. As the Froude number increases to 2.45 and 2.92, the eddies becomes less well defined. Surface waves are observed in and outside of the basin. Especially in Figure 6–12 (Fr = 2.92), the dye entering into the basin is not by the recirculation of the eddy with the flow. Instead, it seems the dye follows the direction of the surface wave radiation which pumps in and out from the basin to the main flow. The wave pumping is the dominant exchange mechanism.

6.3.2 Accumulation and Retention Time

The dye in the basin increased with time after the dye was introduced from the main flow. The supply of the dye from the leading edge of the basin was maintained until the dye concentration in the basin reached a quasi-steady state. The source of the dye supply was then shutoff to allow the dye concentration in the basin to reduce with time. The concentration of the basin could be obtained by tracking the percentage of green light reduction and the calibration curve. Figure 6–13 shows the basin concentration versus time for all the six experiments. The plots are dimensionless. The dimensionless dye concentration is c^* = $\ln(\frac{cUhL}{c_o q_o})$, which is obtained by the normalization of the source dye mass flux $c_o q_o$. The dimensionless time is $t^* = tU/L$, where U is averaged flow velocity in the main channel and L is the dimension of the square basin. The concentration of the dye in the basins c^* first increased with time t^*. It reaches a quasi-steady state after a period of time. The decay of the dye concentration in the basin is subsequent to the quasi-steady state after the dye

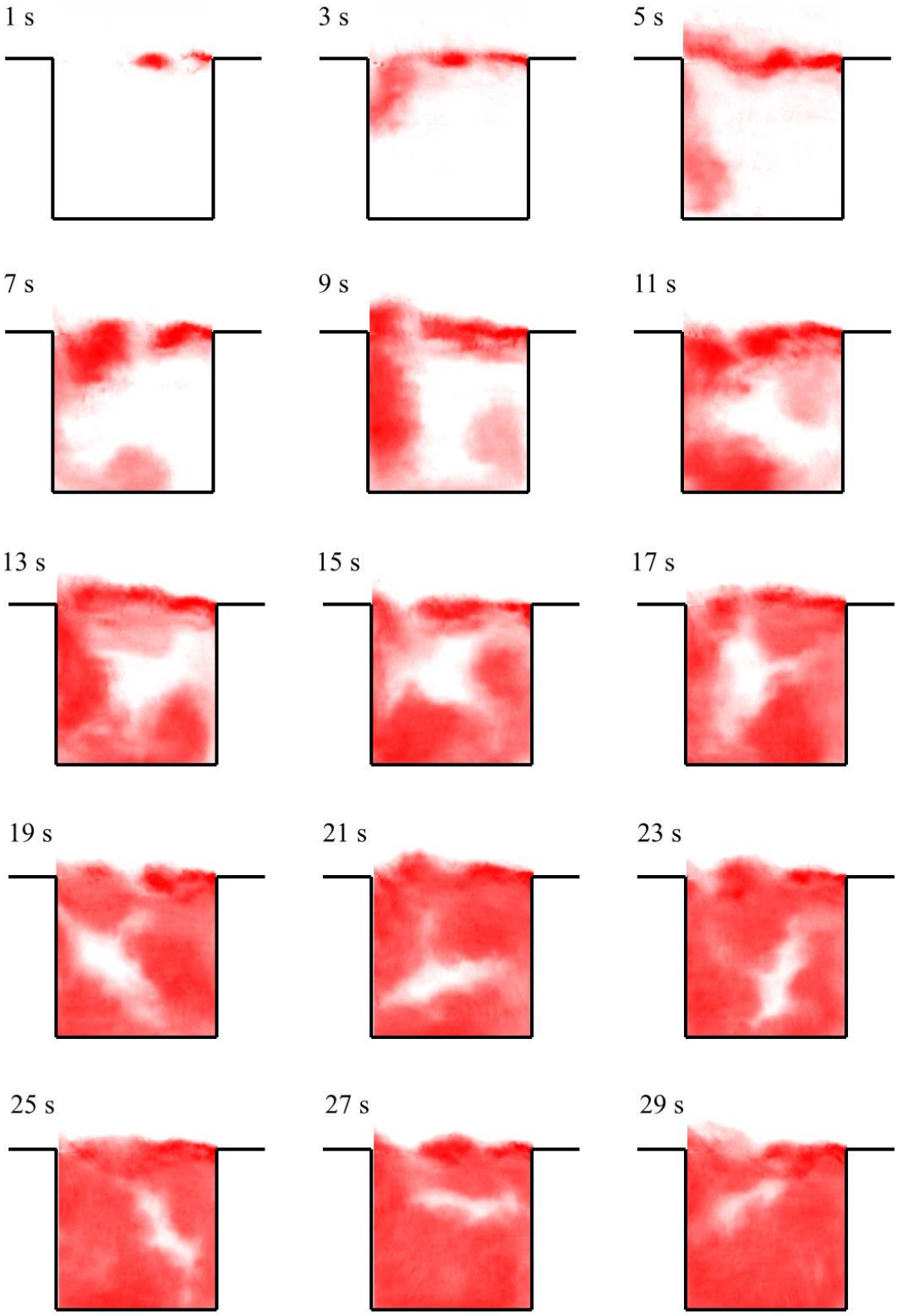

Figure 6–10: Dye accumulation images for Fr = 0.48

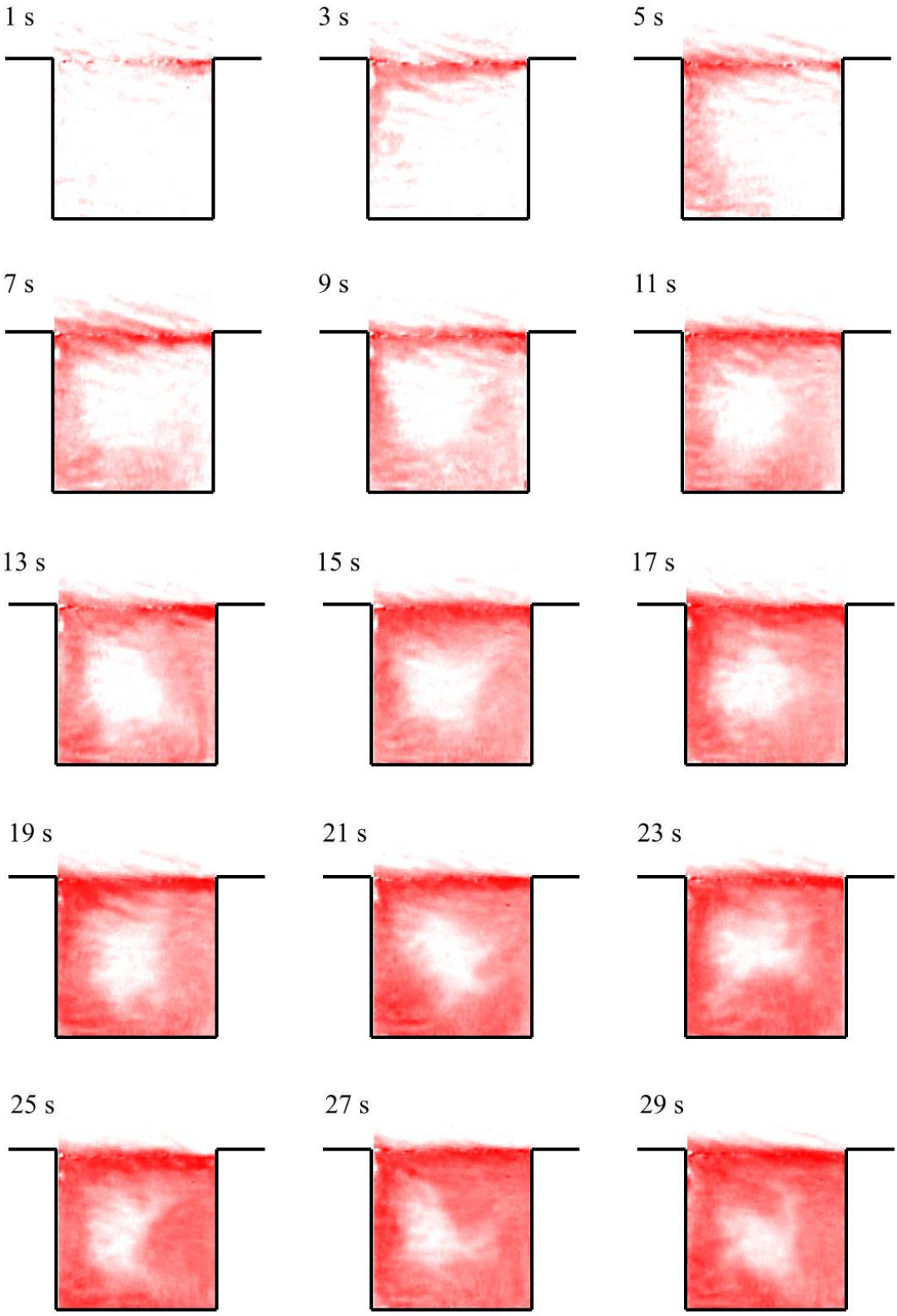

Figure 6–11: Dye accumulation images for Fr = 2.45

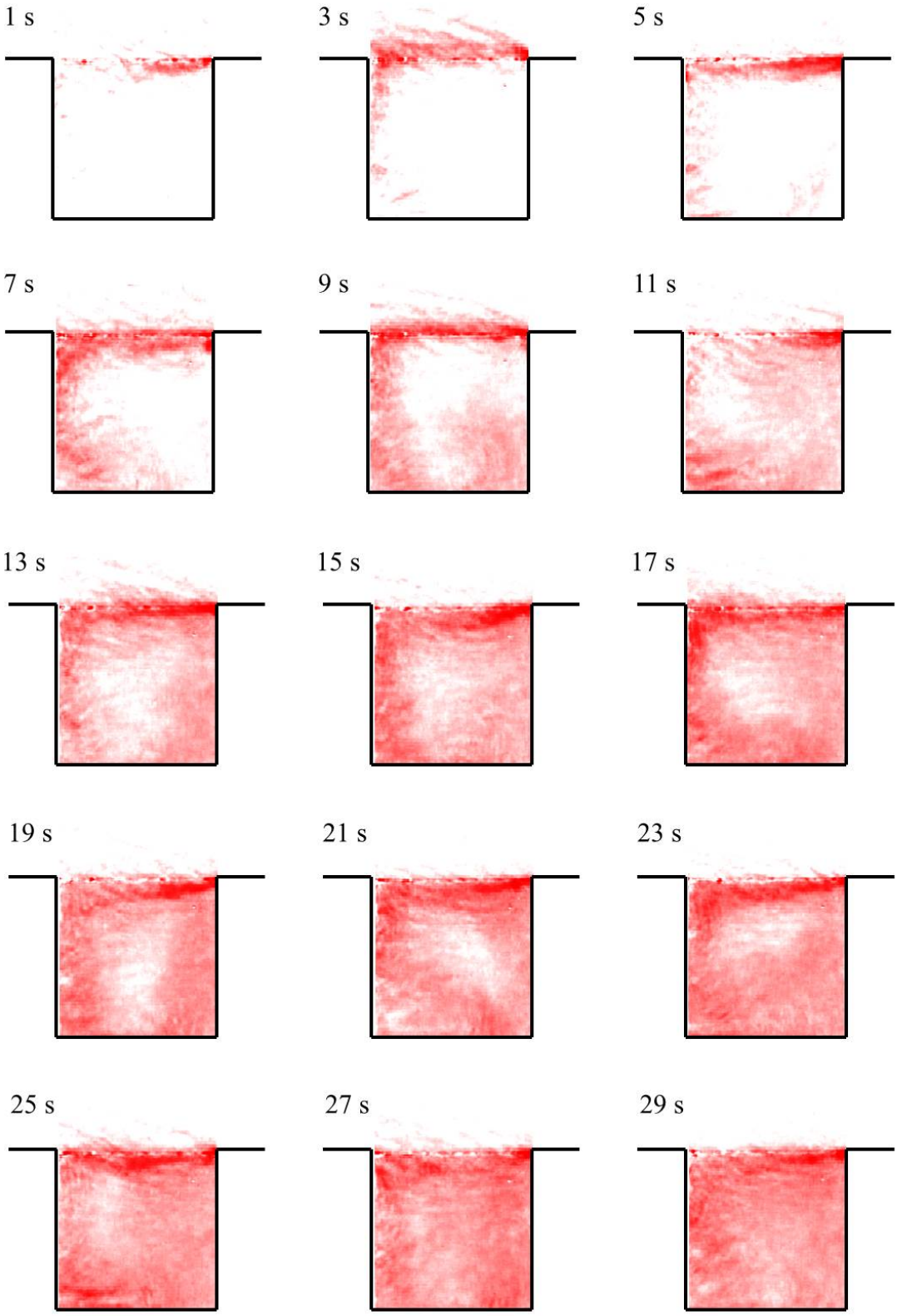

Figure 6–12: Dye accumulation images for Fr = 2.92

supply is shutoff from the upstream source. A curve of the following functional form is fitted through the experimental data for the period during the accumulation phase:

$$c^* = c^*_{qs}(1 - exp(-\frac{t}{\tau_a})) \tag{6.4}$$

where τ_a is the dimensionless accumulation time and c^*_{qs} is the dimensionless quasi-steady concentration. Similarly, the reduction of the dye concentration with time for the period during the decaying phase is fitted with the follow function. τ_r is the dimensionless retention time.

$$c^* = c^*_{qs}(exp(-\frac{t}{\tau_r})) \tag{6.5}$$

The accumulation time scale τ_a and the retention time scale τ_r are the dimensionless parameters that are introduced to characterize the overall exchanges of fluids in the basin with the main flow in the open-channel. A large value of the dimensionless time scales would suggest a slow exchange process and vice versa. Booij (1989) has used the retention time τ_r to define the exchanges of subcritical flow in harbours. Altai and Chu (1997) determined the retention time τ_r for a wider range of the subcrtical Froude numbers, and found the retention time to have comparable values as those obtained by Booij (1989).

The accumulation and retention phase of the experiment could be fitted by the first order exponential curves in Equation 6.4 and 6.5 as shown in Figure 6–14 and 6–15 for all the experiments. It appears that the data fit quite well with the concentration data in the retention phase rather than the accumulation phase. This is probably due to the complexity of the dye accumulation process. The first order equation may over simplify the process. There are other parameters such as basin oscillation and channel friction could affect the dispersion of the dye and subsequently affect the accumulation time. On the other hand, the retention time is a better measure of the mass exchange process between the basin and the main open-channel flow. In both subcritical and supercritical experiments, the retention could be described as first order decay. The eddies in the subcritical experiments and waves in the supercritical experiments dominate the retention process than any other effect.

Table 6–4 summarizes the values of the basin dimensionless retention time scales from the experimental data. Bigger retention time means it takes longer time for the dye to escape the basin thus indicates less mass exchange with the main flow. The values of the retention time for the subcritical main flow are rather reasonable. It is comparable in magnitude to the previous results obtained by Booij (1989) and Altai and Chu (1997) for similar shear flows. However, the dimensionless retention time for the case of the supercritical main flow is three to four times greater than the value of the subcritical flow. Figure 6–16 plots the retention time τ_r^* versus the Froude number Fr obtained from the present series of experiments. The retention time is about $\tau_r^* = 24.6$ and 30.2 for subcritical flow with Fr = 0.48 and 0.52. τ_r^* progressively increases as the increase of the Froude number. It reaches 107.2 at Fr = 2.92. The big difference in retention time is also confirmed by the observation from the images described previously. It is clear that the mass exchange processes in the supercritical flow are different from the processes in subcritical flow. The exchanges in the subcritical flow are characterized by the roll up of the fluid in the coherent eddies and the excitation of the shear layer by the gravity wave feedback as evident in the dyed flow images shown in Figure 6–10. On the other hand, the exchanges in the supercritical flow are due to gravity waves radiation from the shear layer in a manner analogous to the development of supersonic shear layers in compressible fluid (Bogdanoff (1983), Papamoschou and Roshko (1988), Kim (1990)). There is no evidence that can be found in Figure 6–12 to suggest that coherent eddies had formed in the supercritical shear layer. Although significant flow oscillations are produced by the radiation of the gravity waves, the presence of the gravity waves do not seem to have any direct effect on the mass exchanges of the dye between the basin and the supercritical main flow. The indirect effect of wave radiation on the shear instability is however expected.

6.3.3 Mean and RMS Concentration Profiles

The quasi-steady state concentration profile could be further analyzed by statistical method. A series of images in the quasi-steady state are produced with the frame interval

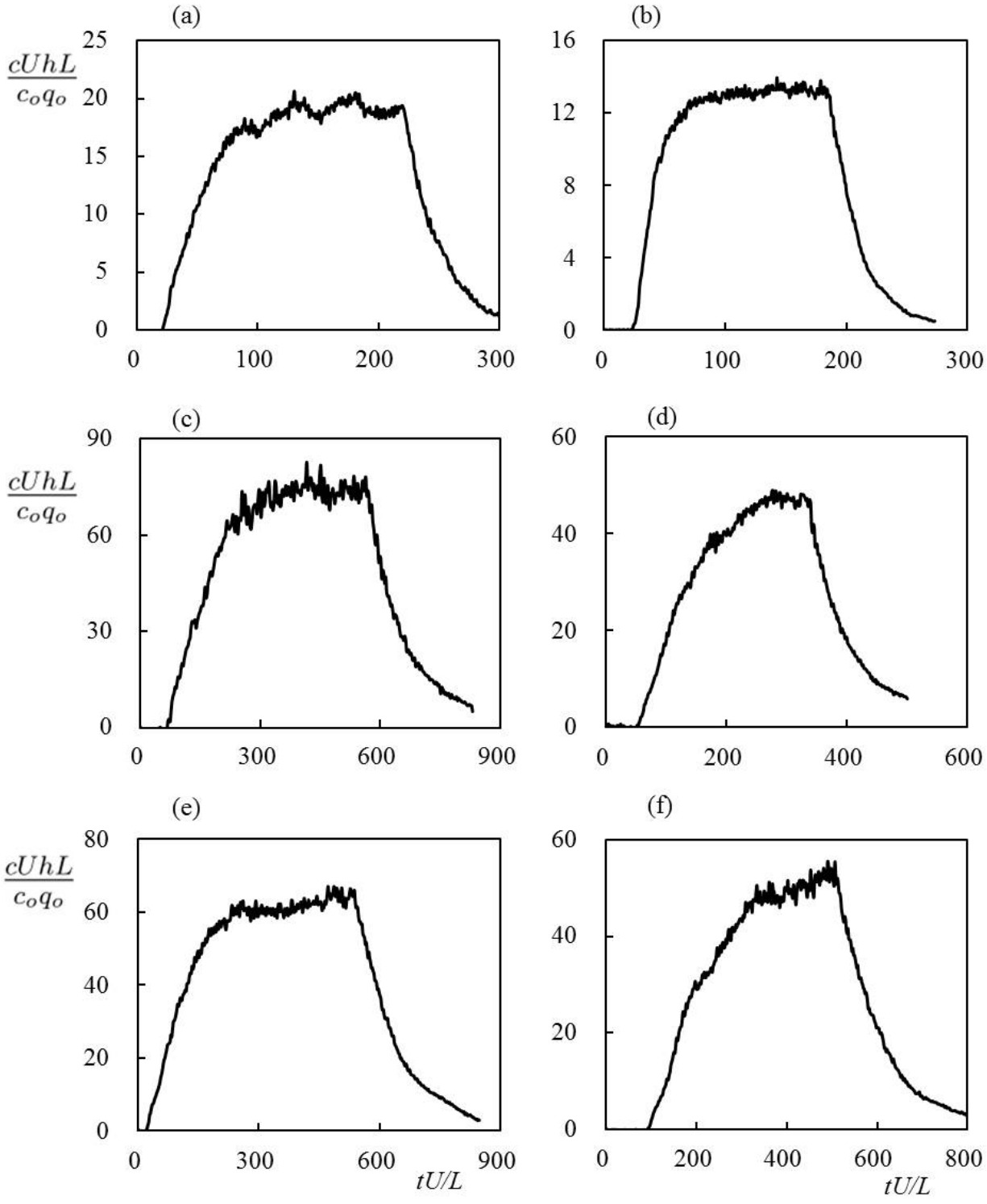

Figure 6–13: The evolution of the dye concentration inside the basin with time as the dye turns on and then shuts off at the source

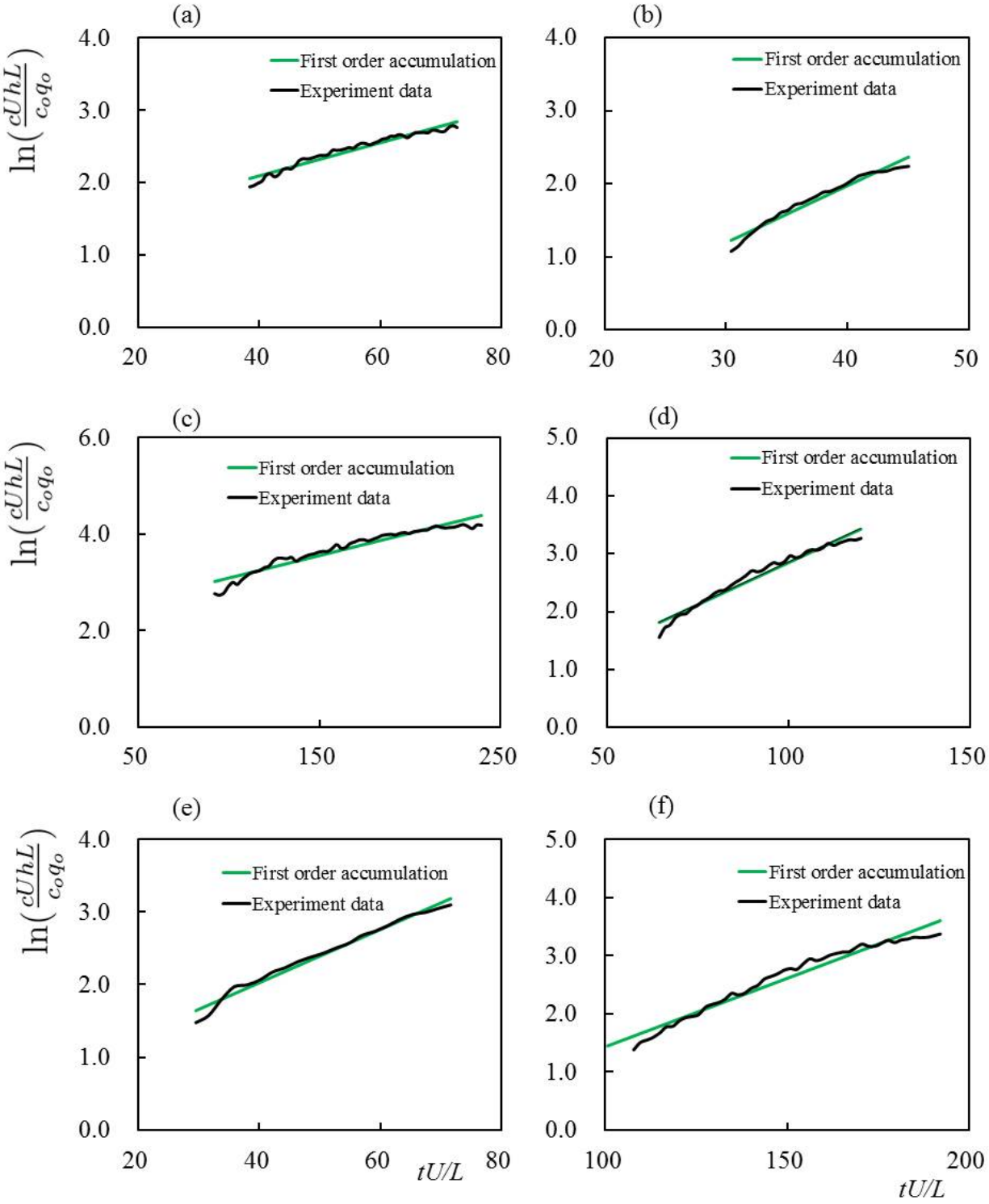

Figure 6–14: Dye concentration inside the basin in the accumulation process. The green line shows the best-fit line from the first order accumulation equation.

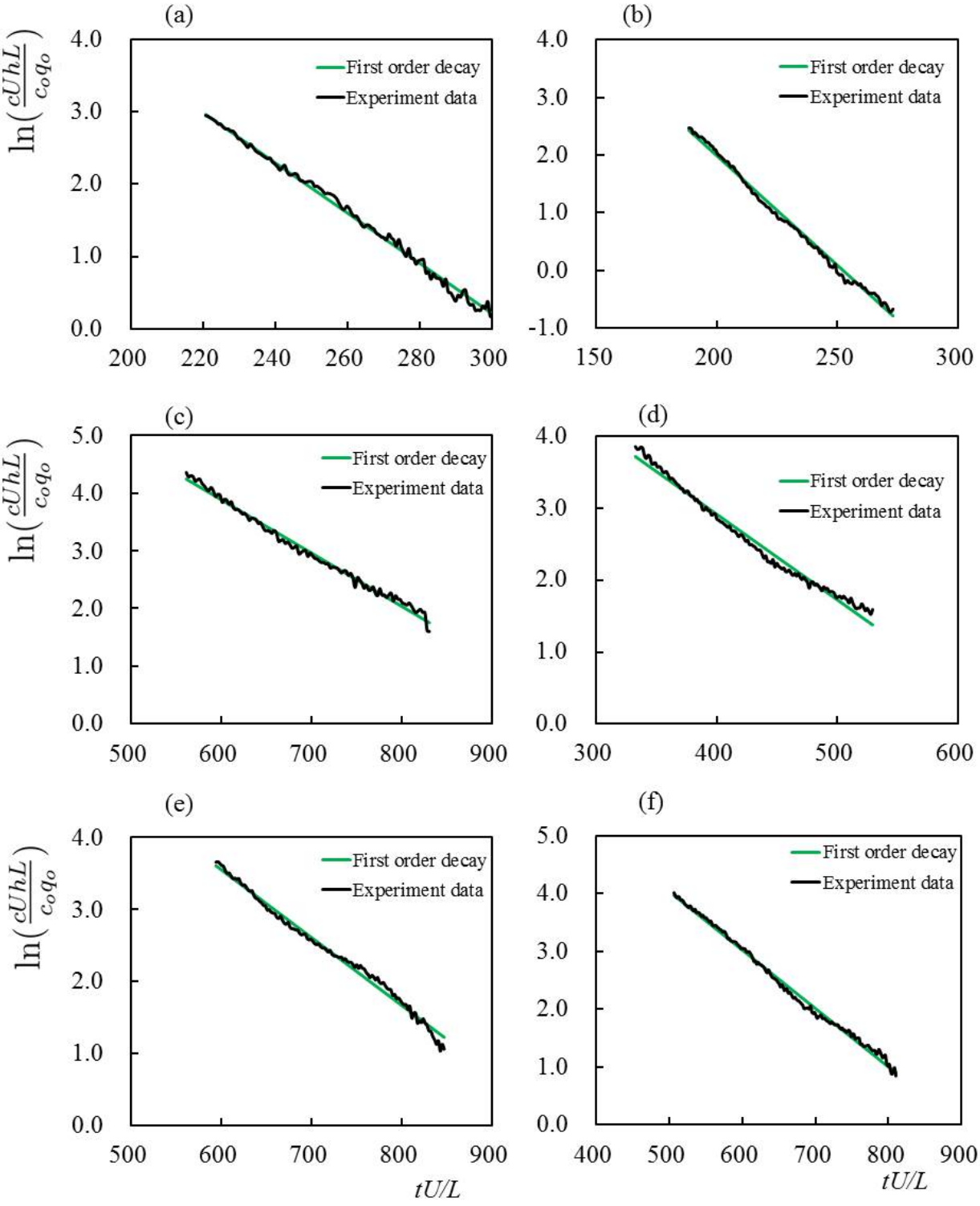

Figure 6–15: Dye concentration inside the basin in the retention process. The green line shows the best-fit line from the first order decay equation.

Table 6–4: Dimensionless retention time for all the experiments

Experiment No.	Fr	c_{qs} (mg/L)	τ_r (s)	τ_r^*
E1	0.55	3.0	22.0	30.2
E2	0.48	12.0	21.0	24.6
E3	2.92	6.0	21.5	107.2
E4	1.69	7.5	24.0	71.9
E5	2.45	21.0	24.5	103.2
E6	2.14	26.0	26.5	95.2

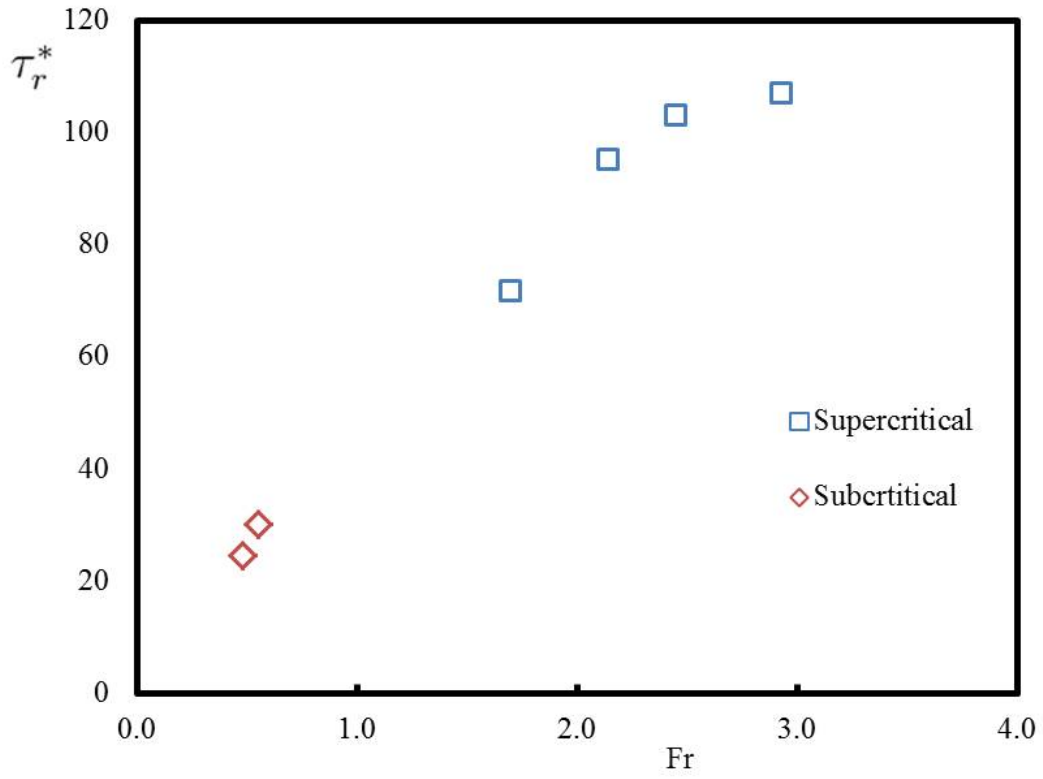

Figure 6–16: Dimensionless retention time correlates to Fr

1/30 s. In each image, at each pixel number (x,y), the dye concentration could be calculated by the video imaging method and the calibration curve described in the previous section. Therefore, the instantaneous dye concentration in the quasi-steady state $c(x, y, t)$ is defined as a function of space and time. The mean concentration $\bar{c}(x, y)$ at a particular location x and y could be calculated from averaging the instantaneous concentration $c(x, y, t)$ in Equation 6.6. N is the total number of quasi-steady state images.

$$\bar{c}(x, y) = \frac{1}{N} \sum_{n=1}^{N} c(x, y, t) \tag{6.6}$$

The root mean square (RMS) of the concentration fluctuations could be also obtained from the following equation.

$$\sqrt{\bar{c'^2}}(x, y) = \frac{1}{N} \sum_{n=1}^{N} [c(x, y, t) - \bar{c}(x, y)]^2 \tag{6.7}$$

The mean concentration profiles and the RMS concentration fluctuation profiles across of the mixing layer are plotted at three longitudinal sections, $x = 0.25L$, $0.5L$, and $0.75L$. The location of these sections is defined in Figure 6–6. The dimensionless mean concentration profiles $\bar{c}UhL/c_o q_o$ and the dimensionless RMS profiles $\sqrt{\bar{c'^2}}UhL/c_o q_o$ for all six experiments are shown in Figure 6–17 and Figure 6–18. In these plots, the x-axis is y/L, indicating the position in longitudinal direction. The origin $y/L = 0$ is defined at the upper right corner of the basin, which is also the location of dye injection point. Positive y/L values indicate the location outside the basin in the main stream while negative y/L values indicate the location inside the basin. y/L = -1 is defined at the inner edge of the basin.

The mean concentration profiles shown in Figure 6–17 are a measure of basin oscillation. In subcritical experiments E1 and E2, the basin shows more regular behavior as the quasi-steady state concentration inside the basin is a constant. The concentration outside the basin drops smoothly and approaches to zero as moving away from the mixing layer. The mixing layer is well defined. In supercritical flow experiments, dye concentration inside the basin is also a constant but with more variation. The variation is due to the generation

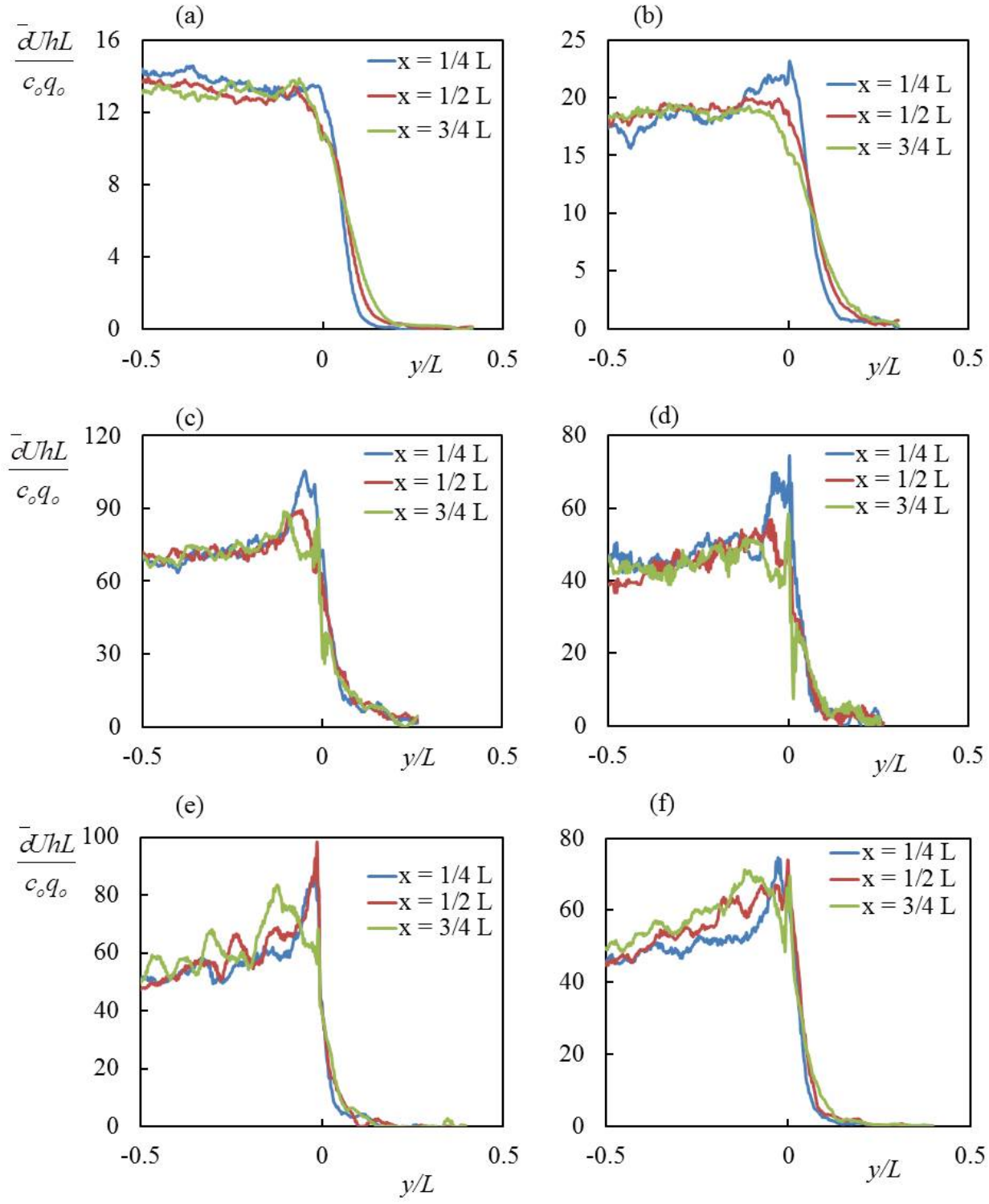

Figure 6–17: Mean concentration profiles at cross sections $x = 0.25L$, $0.50L$, and $0.75L$ for all the experiments. (a) E1 (b) E2 (c) E3 (d) E4 (e) E5 (f) E6

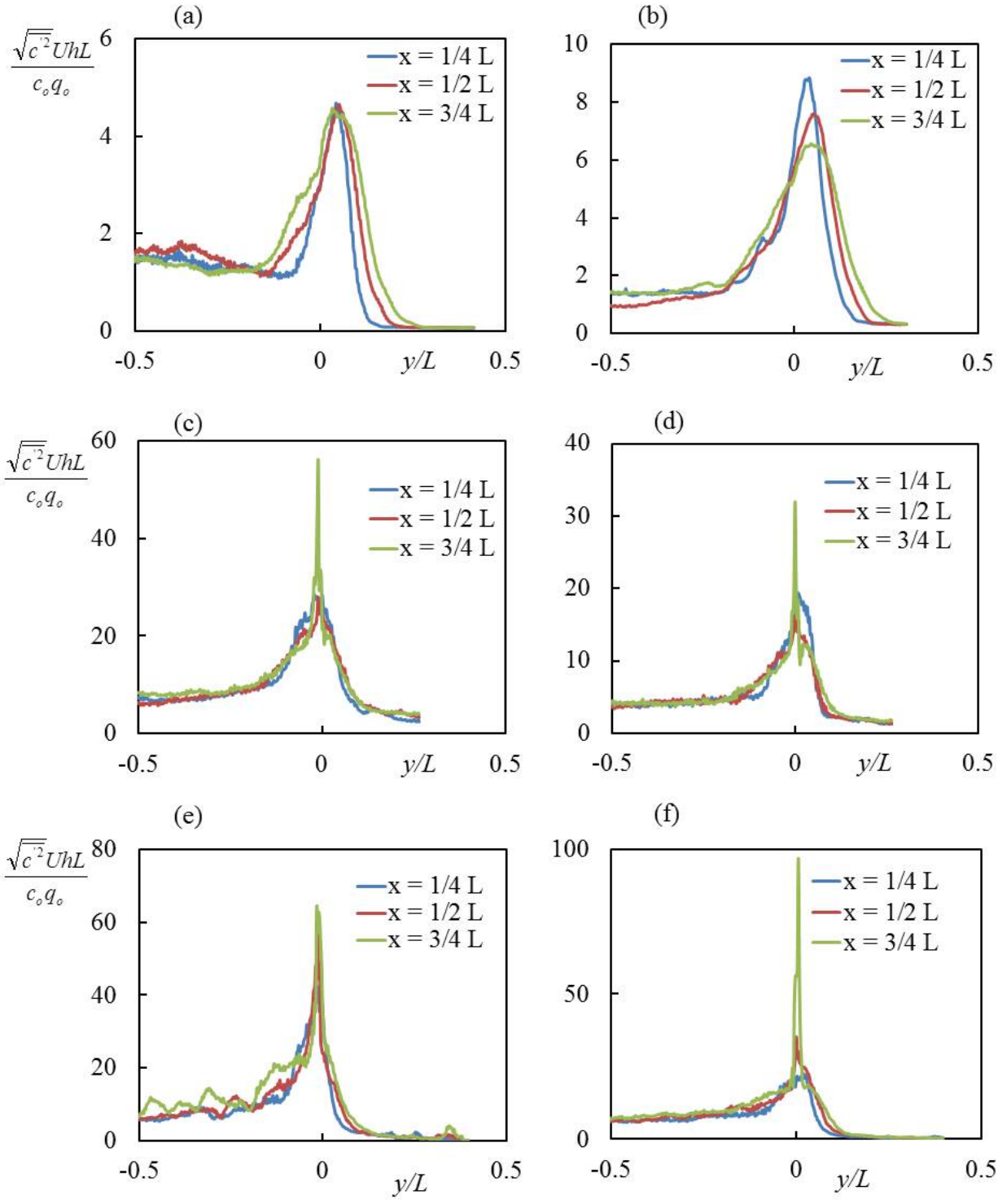

Figure 6–18: Root mean square profiles at cross sections $x = 0.25L$, $0.50L$, $0.75L$ for all the experiments. (a) E1 (b) E2 (c) E3 (d) E4 (e) E5 (f) E6

of the gravity waves. The concentration outside the basin is more oscillatory because the gravity waves continuously pumping in and out from the basin. The concentration outside the basin changes more significantly particularly in the cross section $x = 0.75L$. This is due to the fact that mixing layer is not well defined.

The RMS fluctuation profiles follow the Gaussian distribution as shown in Figure 6–18. The maximum RMS value is at the outside edge of the basin. The RMS fluctuation is produced by the excitation of the mixing layers from the basin. At high Froude numbers, an extremely high peak value is observed at $x = 0.75L$. At downstream of the basin, the variation in concentration is big and the mixing process is extremely irregular. The basin excitation is enhanced by gravity waves and more turbulence is observed. As a result, subcritical flows demonstrate more vigorous and regular mixing process while supercritical flows demonstrate less vigorous and irregular mixing process.

6.3.4 Mixing Layer Thickness

The width of the mean concentration profile is illustrated in Figure 6–19 (a). It shows the dimensionless concentration $\bar{c}UhL/c_o q_o$ at location $x = 0.25L$ for Fr = 2.45. The maximum concentration $\bar{c}_{max}$ is defined in the figure first. The lateral position of the profile (y_{mean}) is then found to be one-half of the maximum concentration ($\frac{1}{2}\bar{c}_{max}$). The y_{mean} is a measure of the mixing layer thickness based on the mean profile. Similarly, the width of the RMS fluctuation profile is illustrated in Figure 6–19 (b). The lateral positions corresponding to one-half of the maximum RMS fluctuation $\frac{1}{2}\sqrt{\overline{c'^2}}_{max}$ are y^+_{rms} in positive axis and y^-_{rms} in negative axis. The half width of the RMS fluctuation profile δ is calculated as

$$\delta = y^+_{rms} - y^-_{rms} \tag{6.8}$$

Figure 6–20 plots y_{mean}, y^+_{rms} and y^-_{rms} for three different Froude numbers (Fr = 0.48 , 1.69 and 2.45) at locations $x = 0.25L$, $x = 0.5L$, and $x = 0.75L$, respectively. When Fr = 0.48, the depth of the turbulent flow is deep and the mixing layer behaves more orderly.

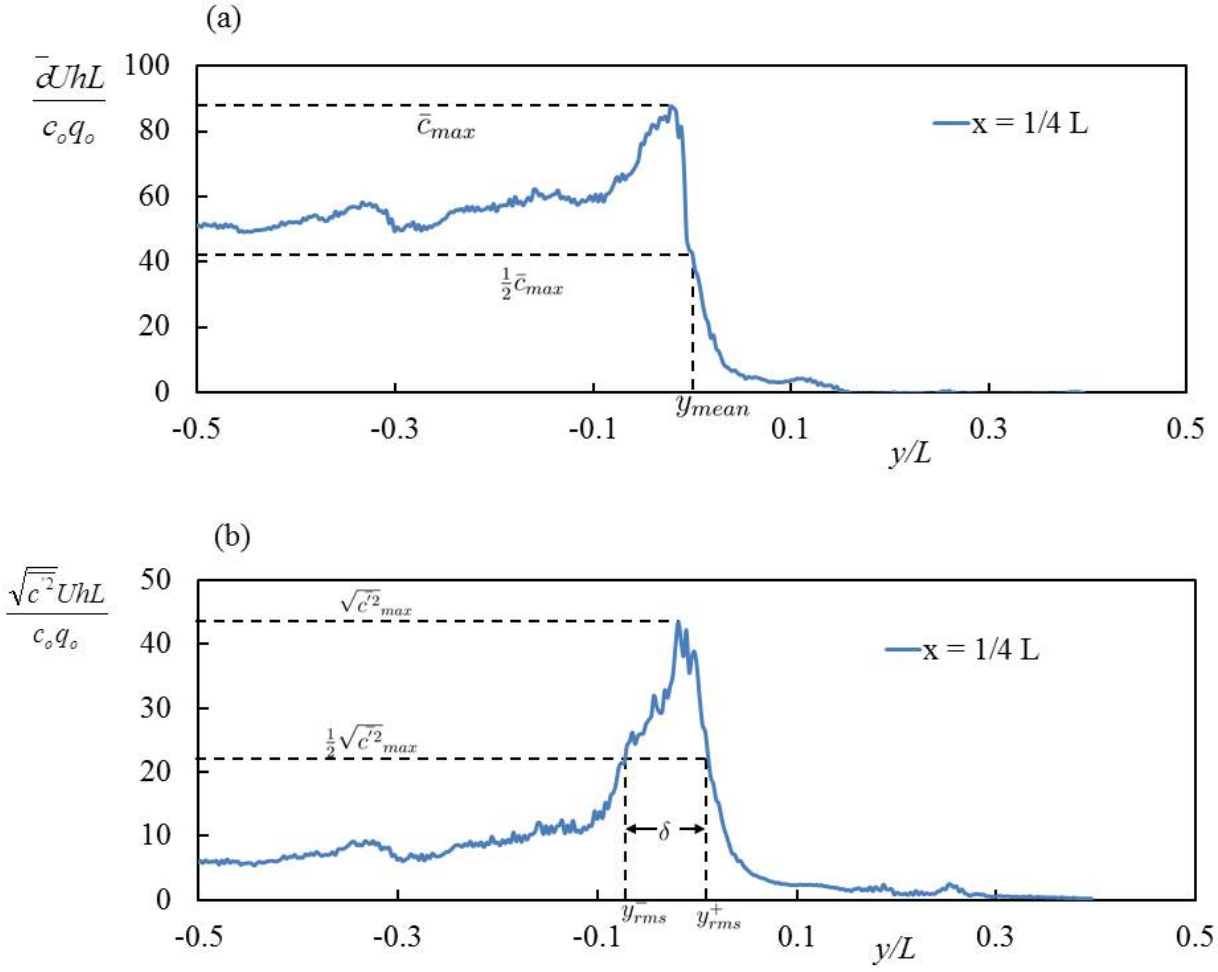

Figure 6–19: (a)definition of the mixing layer width by mean concentration (b)definition of the mixing layer width by RMS.

The layer thickness shown in RMS fluctuation profile increase linearly as moving away from the origin. This result agrees with previous experiments on the measurement of free mixing layer (Wygnanski and Fiedler (1970), Brown and Roshko (1974), Champagne et al. (1976)). They concluded the growth rate of the free mixing layer increased with distance at low Froude numbers. However, for Fr = 1.69 and 2.45, the linear dependence on the distance does not exist any more. Instead, the layer thickness reduces in all three locations because of continuous excitation of the gravity waves.

Figure 6–21 shows the variation of the mixing layer thickness based on the mean profile and RMS fluctuation profile at longitudinal locations $x = 0.25L$, $x = 0.5L$, and $x = 0.75L$

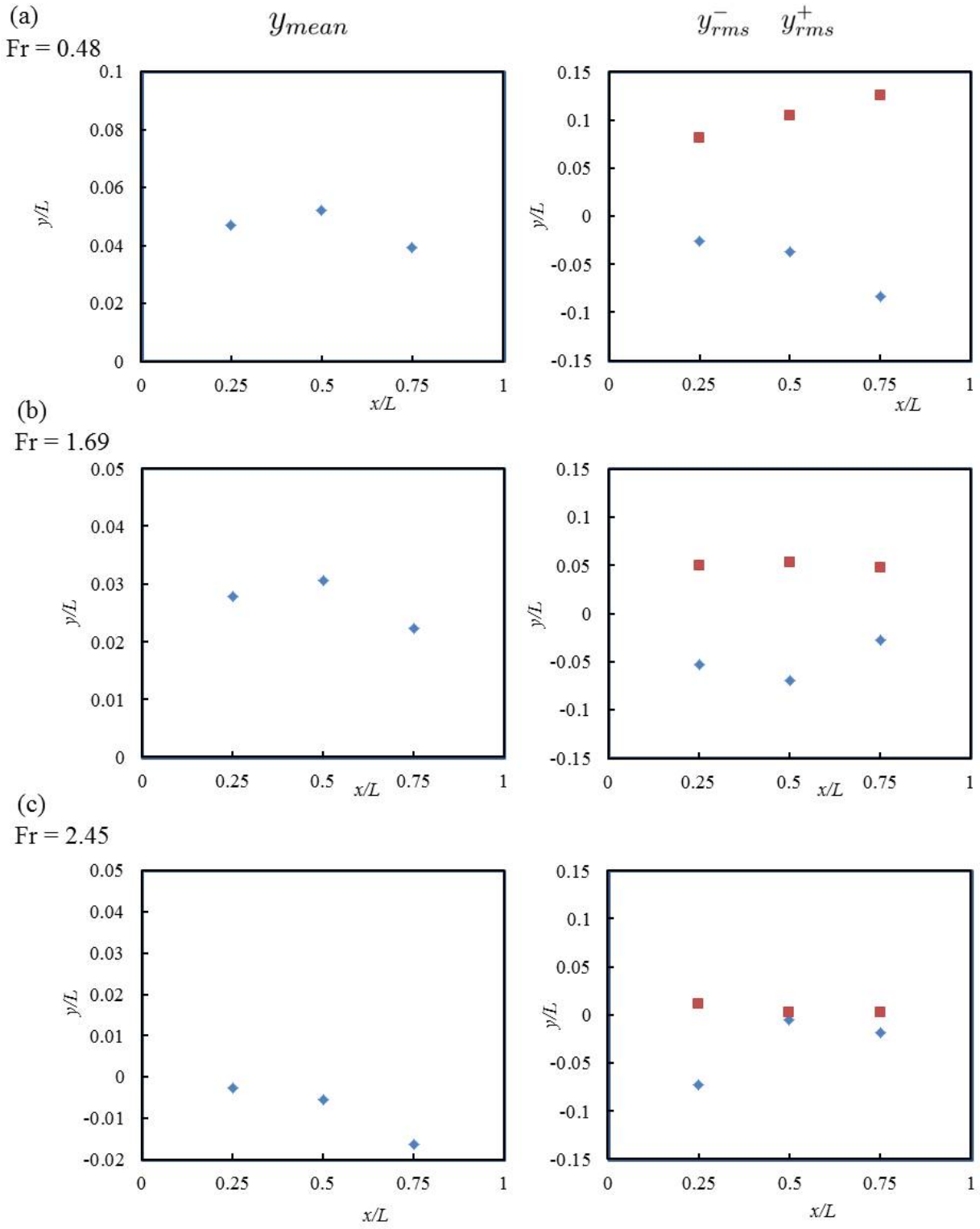

Figure 6–20: Mixing layer thickness of y_{mean}, y^+_{rms} and y^-_{rms} in three different Froude numbers at locations $x = 0.25L$, $x = 0.5L$, and $x = 0.75L$

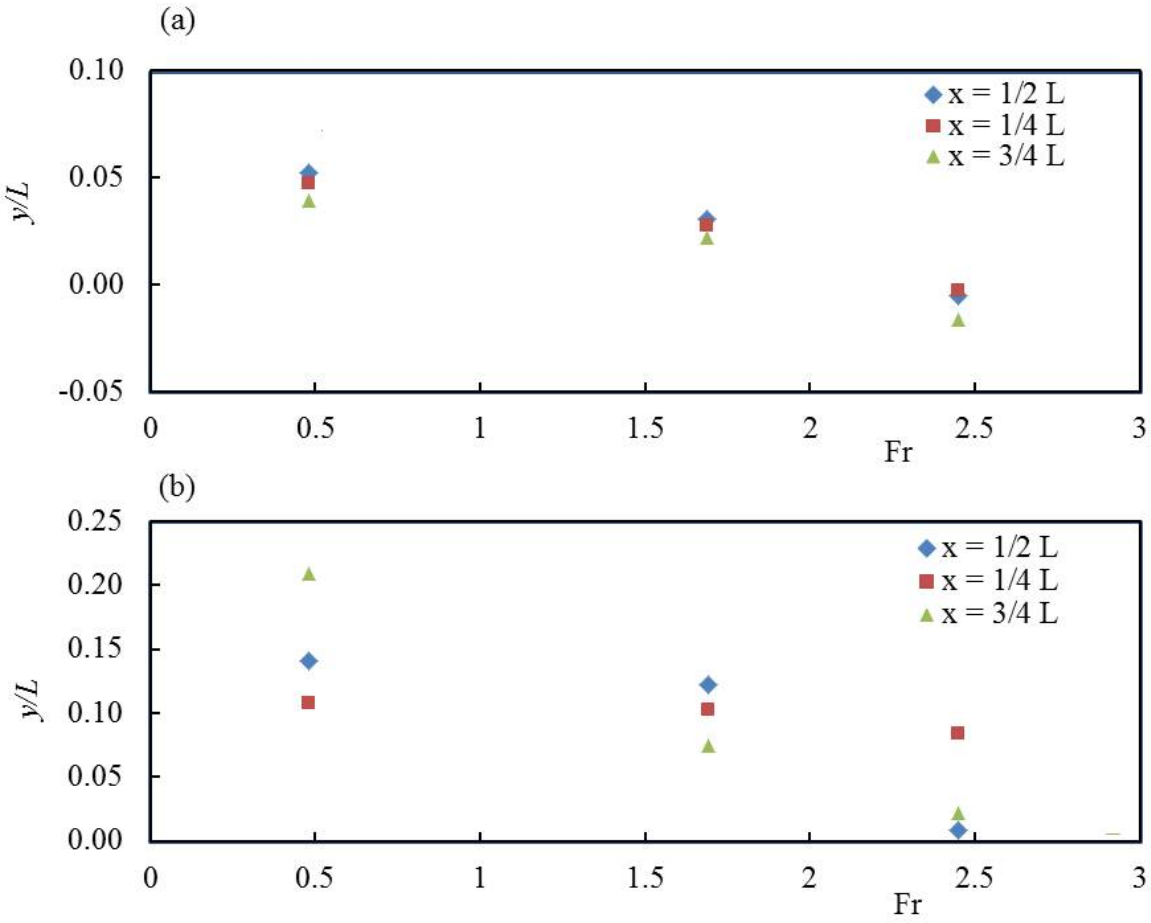

Figure 6–21: The variation of the mixing layer thickness Versus Froude number (a) based on the mean profile and (b) based on the RMS fluctuation profile

with the Froude number Fr. Both of the mean profile and RMS fluctuation profile suggest the mixing layer thickness decreases with Froude number for all three locations. Also, the thickness of the supercritical mixing layer is significantly smaller in comparison with that of the subcritical mixing layer. Such results are qualitatively in agreement with the numerical simulation of the flow shown in Figure 6–4.

6.4 Conclusion

The subcritical and supercritical flow exchanges were studied experimentally by a video imaging method. In subcritical flow, the process of the entrainment across the shear layer

was due to formation of eddies in the shear layer between the main flow and the recirculating flow in the basin. The entrainment is due to roll up of fluid to form eddies. In supercritical flow on the other hand, the entrainment was not as well defined. Gravity waves were generated as the supercritical main flow interacted with the flow in the basin. The radiation of the gravity waves away from the basins was intense but did not positively affect the entrainment. In comparison with the case of the subcritical main flow, the shear layer between the supercritical main flow and the flow in the basin was less turbulent.

The retention time is one overall parameter that characterizes the mass and momentum exchanges across the shear layer between the main channel and its side basins. Supercritical flows lead to bigger retention time meaning longer exchange process. The measurement of the parameter using the video imaging technique has supported the conclusion obtained from hydrodynamic stability analysis that the supercritical shear layer is more stable to disturbance and as a consequence less energetic for the exchanges across the shear layer.

Statistical analysis on the mean profile and RMS fluctuation profile is also conducted on the dye concentration in the basin in quasi-steady state. The transient variation of the dye in the basin had been analyzed. The results obtained from the transient analysis had led to essentially the same conclusion that the mixing across the supercritical shear layer is significantly reduced due to wave radiation from the shear flow. These observed radiation-damping in supercritical shear flow is a phenomenon supported by stability analysis in Pinilla and Chu (2009) and numerical simulations in Chu (2010).

CHAPTER 7

NUMERICAL SIMULATIONS OF MACRO RESISTANCE IN STEEP OPEN CHANNELS AND MEANDERING CHANNELS

7.1 Introduction

The navigation of water around rocks and boulders in mountain stream is a process that is unique and distinctively different from the slow flow through large rivers. In steep channel, the flow changes rapidly from subcritical to supercritical at the control sections. The photo of the steep mountain stream in Figure 7–1 depicts the process. Significant energy dissipation occurs in the hydraulic jumps as the supercritical flow returns to its subcritical state. The white waters in the steep river are the demarcation for the return of supercritical flow to its subcritical state.

The resistance to flow is traditionally parameterized using the Manning coefficient of friction n_{bed}. The values of the Manning n_{bed} are tabulated (Arcement and Dchneider (1989), Chow (1959)). However, the selection of an appropriate n_{bed} from the tables is a matter of intangibles as described by Ven Te Chow (1959): "To veteran engineers, this means the exercise of sound engineering judgment and experience; for beginners, it can be no more than a guess, and different individuals will obtain different results. "Alternatively, the value of n_{bed} can be determined from in-situ measurements as described in French (1985). Either of these methods can be problematic.

In this chapter, the flow resistance is determined by direct numerical simulations. The goal of the simulations is to show that the Manning formulation is not generally correct when the dimensions of the obstacles are comparable to the width of the flow. The resistance to flow will be shown to be better correlated with an averaged drag coefficient. The direct numerical simulation also will provide the force and moment calculation that is critical in

Figure 7–1: The transition from subcritical to supercritical flow at the control sections and the return to subcritical flow through the hydraulic jumps. The white waters mark the location of the jumps.

the determined incipient motion of rocks and boulders in the highly unsteady flow through the mountain stream.

7.2 Numerical Models

7.2.1 Trans-critical Solver MIS2D

The development of the trans-critical solver for 2D numerical simulation of the shallow open-channel flow is based on finite-volume formulation using a staggered grid. The finite-difference equations in the limit as Δx and Δy approach zero are the partial differential equations:

$$\frac{\partial h}{\partial t} + \frac{\partial q_x}{\partial x} + \frac{\partial q_y}{\partial y} = 0 \tag{7.1}$$

$$\frac{\partial q_x}{\partial t} + \frac{\partial}{\partial x}\left(\frac{q_x^2}{h}\right) + \frac{\partial}{\partial y}\left(\frac{q_x q_y}{h}\right) = -\frac{1}{2} g \frac{\partial h^2}{\partial x} - f_x \tag{7.2}$$

$$\frac{\partial q_y}{\partial t} + \frac{\partial}{\partial x}\left(\frac{q_x q_y}{h}\right) + \frac{\partial}{\partial y}\left(\frac{q_y^2}{h}\right) = -\frac{1}{2} g \frac{\partial h^2}{\partial y} - f_y \tag{7.3}$$

f_x and f_y are the friction force components which relate the Manning coefficient n_{bed} and the velocity components (u, v) as follows:

$$f_x = n_{bed}^2 g \frac{u\sqrt{u^2+v^2}}{h^{\frac{1}{3}}}, \quad f_y = n_{bed}^2 g \frac{v\sqrt{u^2+v^2}}{h^{\frac{1}{3}}} \tag{7.4}$$

The procedure to perform the direct numerical simulation to obtain the solution of Shallow Water Equations is described previously in Chapter 2. The numerical solver has to be effective in capturing the discontinuity of the shock waves. The flux limiter with minimal intervention strategy (MIS) is applied in the momentum equations. This two-dimensional trans-critical solver based on the minimal intervention strategy will be referred as MIS2D model in this chapter.

7.2.2 FLOW-3D Hydrodynamic Model

The validation of the MIS2D model is checked against the commercial software FLOW-3D. FLOW-3D is a hydrodynamic model analysis tool that solves the full flow governing equations, the Navier-Stokes equations, in three dimensions (Hirt (2011)). The popularity of the 3D modeling has increased with the availability of more powerful desktop computers. The computational domain is divided into Cartesian computational meshes in the simulations. The mesh is staggered which means depth and pressure are defined at the cell center and velocity and shear stress are defined at cell faces. Given the initial conditions, an explicit solution method is used to evaluate the variables associated with velocities for the next step in the Navier-Stokes equations. Water pressure is evaluated in each cell by an iterative method until finding a converged state and then cell velocities are adjusted accordingly. Volume of Fluid (VOF) technique is used to compute the water free surface and come up

with the new configuration. The turbulence model is activated to solve the viscosity term by Renormalized Group (RNG) Model.

7.3 Model Validation by Oblique Dam-break Waves

7.3.1 Oblique Dam-break Waves by MIS2D

The simulation of oblique shock waves are performed to validate the MIS2D model. The waves are produced in a 100 m $\times$ 100 m square basin by the sudden removal of a dam. The initial water depths at time $t = 0$ are $h_o = 10$ m and $h_d = 1$ m separated by a dam located in the diagonal direction across the basin. Figure 7–2 (a) shows the plan view of the waves at time $t = 2.5$ s. Figure 7–2 (b) shows the depth and velocity profiles of the waves along the cross section A-A at this time obtained by the MIS2D using the MINMOD flux limiter with grid size of $\Delta x = \Delta y = 0.5$ m.

The MIS2D simulation is highly accurate and is very stable when the MINMOD flux limiter is used minimally to manage the spurious numerical oscillations. The MIS2D simulation profiles with $\Delta x = \Delta y = 0.5$ m are nearly identical to the exact solution obtained by Stoker (1957) using the method of characteristic. At time $t = 2.5$ s, the wave height is $h_s/h_o = 0.396$ and the velocity is $u/gh = 0.741$ according to the exact solution. Figure 7–2 (c) shows the convergence of the MIS2D simulation toward the exact solution as the grid is refined. The order of the convergence for velocity approaches to unity using the procedure for estimating and reporting of uncertainty as recommended by Celik et al. (2008). The integration of the Shallow Water Equations by the MIS2D model is second-order accuracy in time and space according to Pinilla et al. (2010). However, the convergence of the surge wave velocity to the exact solution is only first-order. This behavior nevertheless is consistent with the recent Godunov's assessment on the discontinuous solutions of the shallow-water equations.

7.3.2 Oblique Dam-break Waves by FLOW-3D

The simulation of the same oblique dam-break waves is repeated using a computational fluid dynamic model known as FLOW-3D developed and commercialized by Flow-Science Inc. (Hirt (2011)). The FLOW-3D model uses the finite difference method to solve numerically the Navier-Stokes equations. The spurious numerical oscillations are managed by a second-order monotonicity preserving method. FLOW-3D also uses the orthogonal staggered mesh. The Volume of Fluid (VOF) method is employed in the FLOW-3D to resolve the free water surface. It provides an accurate way to advect the fluid interface through a fixed computational grid while keeping the interface sharp and well defined. There are three key elements which must be in place in any CFD tools in order to be called a VOF method. First, there must be a fluid fraction variable F, which tracks the amount of fluid within a given computational cell. Second, an advection algorithm is required to not only advect F, but to keep the interface sharp. Third, free surface boundary conditions must be applied to the interface. The area and volume ratios in each cell are computed and the ratios are integrated into the conservation equations. The value of each dependant variable is associated to each cell and applied at the centre of the cell except the velocity, which is applied on the face of the cell. In order to solve the mass conservation and momentum equations, an explicit solution algorithm is used to evaluate the variables associated with velocities in the Navier-Stokes equation for a given time taking into account the initial conditions or variable values at previous time step. Water pressure is evaluated in each cell and iterations are used to advance the solution through a sequence of steps from a starting state to a final, converged state. The cell corresponding to the velocities are then adjusted. The present FLOW-3D simulation uses an uniform grid with $\Delta x = \Delta y = \Delta z$; the dimensions of the grid Δx and Δy are the same as the 2D simulations using MIS2D.

The FLOW-3D package also has the ability to do 2D simulation when the 3D modeling is not necessary. This 2D model is referred as FLOW-3D Shallow Water Model (FLOW-3D-SWM). It allows to model large river reaches, coasts and estuaries, and other large domains.

It takes a 2D grid in $x-$ and $y-$ direction and the vertical velocity is assumed to be zero. The model assumes all variables can be represented by their depth-averaged values and solves the 2D momentum equations with corrections for variation in depth.

The results of the oblique dam-break waves in a 100 m x 100 m square basin due to sudden removal of the dam are shown in Figure 7–3 and Figure 7–4. The initial depths are $h_o = 10$ m and $h_d = 1$ m. There are 20 layers in the vertical direction. Figure 7–4 shows the depth of the waves being color coded by velocity. Figure 7–3 shows the depth and velocity profiles along the diagonal cross section A-A. These FLOW-3D-SWM and FLOW-3D profiles are to be compared with the exact solution shown in Figure 7–2 (b). At this time $t = 2.5s$, the location of surge wave front obtained by FLOW-3D and FLOW-3D-SWM is both behind the supposed location at $x/t\sqrt{gh_o} = 1.0$ and the surge wave height is higher than the exact solution of $h/h_o = 0.396$. The difference is not large. The large difference in the number of layers at the shock-wave front may create numerical difficulty and that may make the 3D solution not realistic.

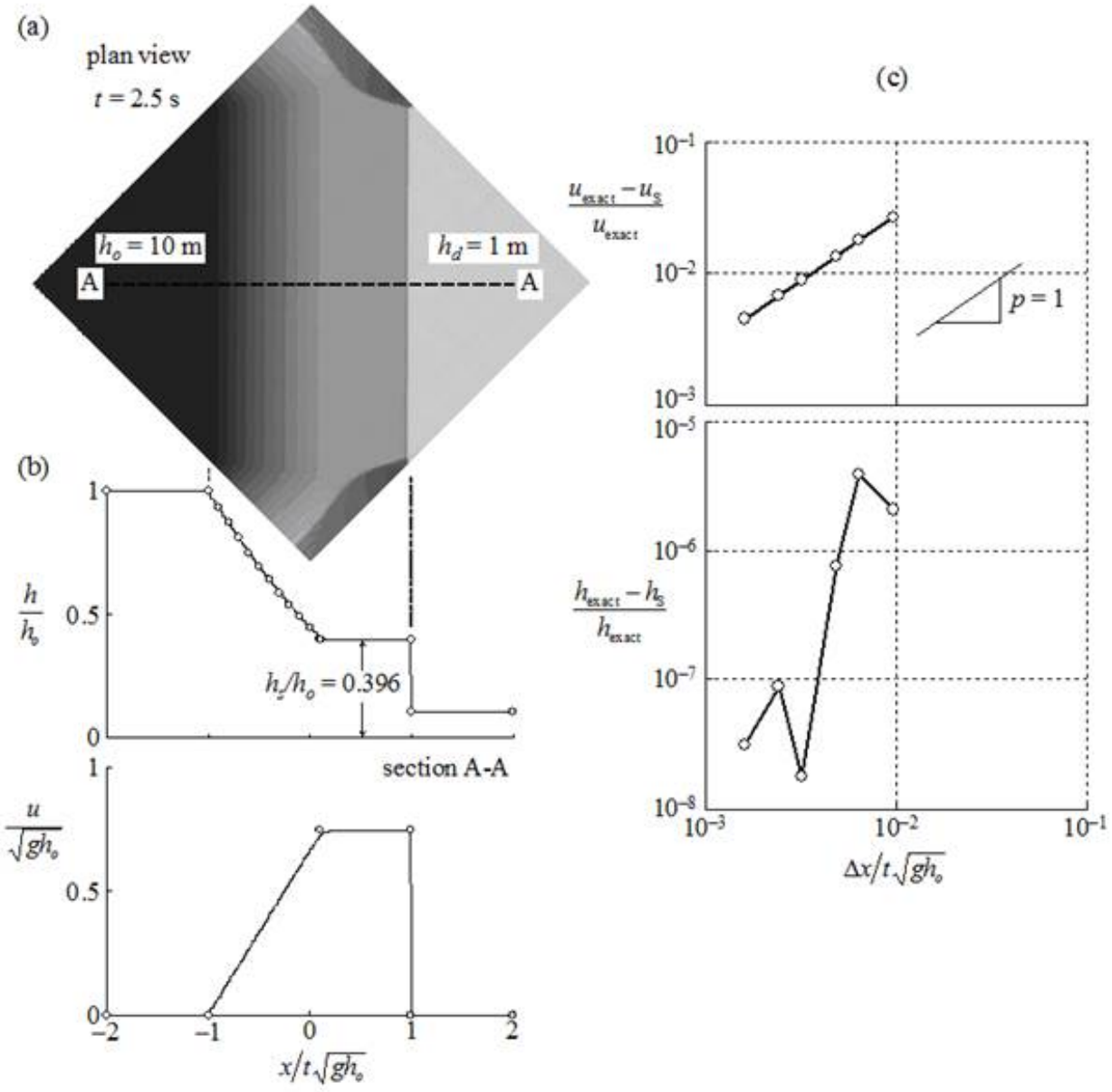

Figure 7–2: Oblique dam-break waves at time $t = 2.5$ s; (a) plan view, (b) depth and velocity profiles along the cross-section A-A, (c) diminishing error as the MIS2D simulation converges to the exact solution. Circle symbol denotes the exact solution of Stoker (1957).

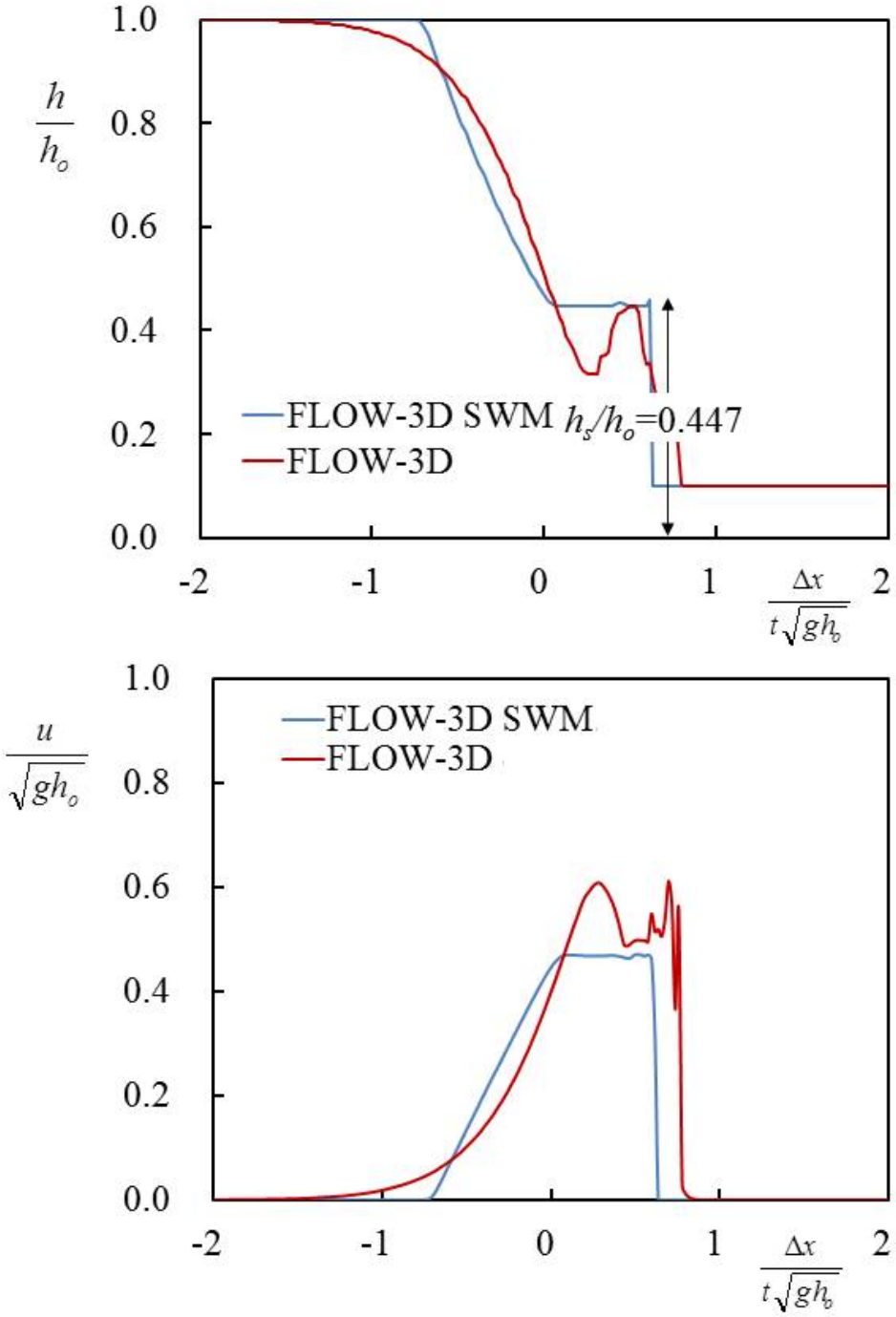

Figure 7–3: Comparison of depth and velocity profiles along the diagonal cross section A-A at time $t = 2.5$ s. Simulations are carried out using the FLOW-3D-SWM and FLOW-3D for the 100 m x 100 m square basin with grid $\Delta x = \Delta y = \Delta z = 0.5$ m

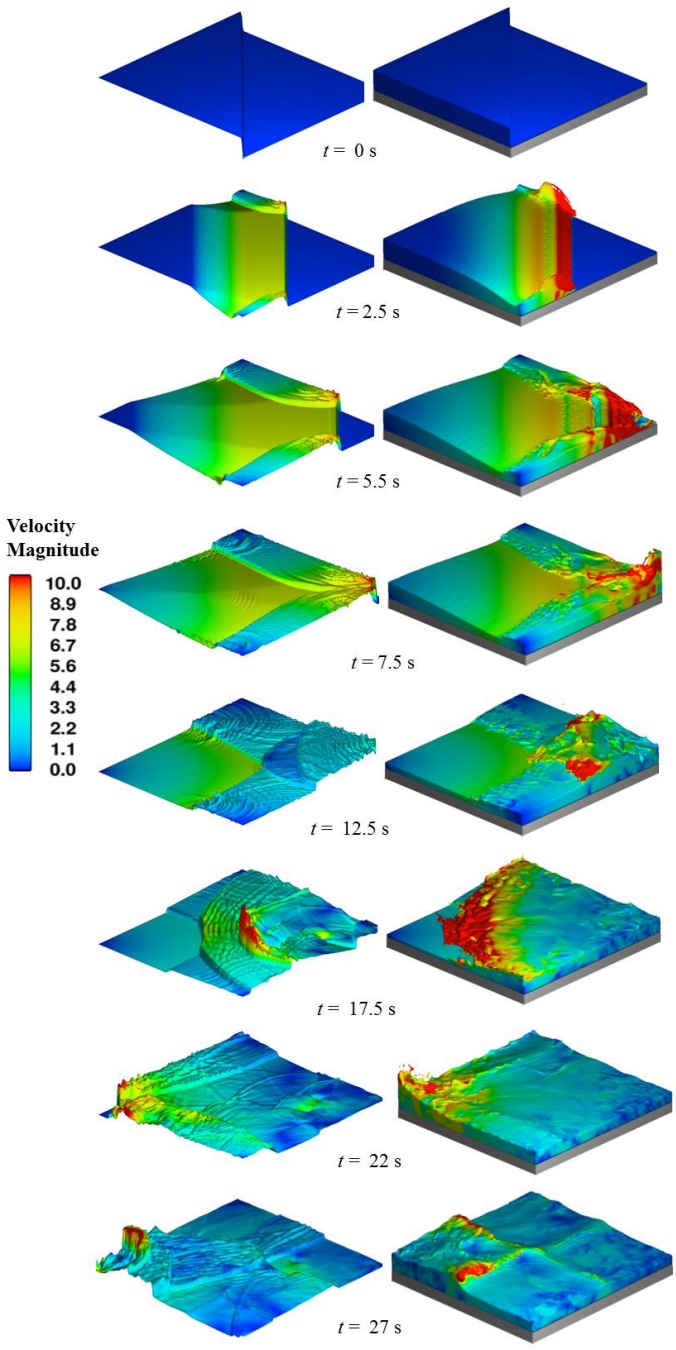

Figure 7–4: Velocity of the oblique shock wave problem. Left-hand side of the figure shows the simulation by FLOW-3D-SWM method while the right-hand side of the figure shows the simulation performed by FLOW-3D model.

7.4 Macro Resistance to Flow in Steep Open-Channel

7.4.1 Comparison of Three Numerical Schemes

The next series of simulations is conducted for open-channel flow in steep slope. The flow through the periodic arrays of blocks in Figure 7–5 is idealized in an attempt to mimic the steep flow in mountain streams. As shown in the plan view of Figure 7–5, the macro resistance to the open-channel flow is due to an array of blocks. To assess the effectiveness of the three schemes, the first set of simulations has an initial depth of $h_o = 2$ m and block width $b = 10$ m. Three channel-bottom slopes are considered at S_o= 0.005, 0.01 and 0.04. Periodic boundary condition is given at the left and right boundaries. The effect of bottom friction is eliminated by setting the roughness to zero and the effect of viscosity is eliminated by not activating the turbulent model. Therefore, the gravity component along the slope is the only driving force to cause the water to flow along the slope of the channel.

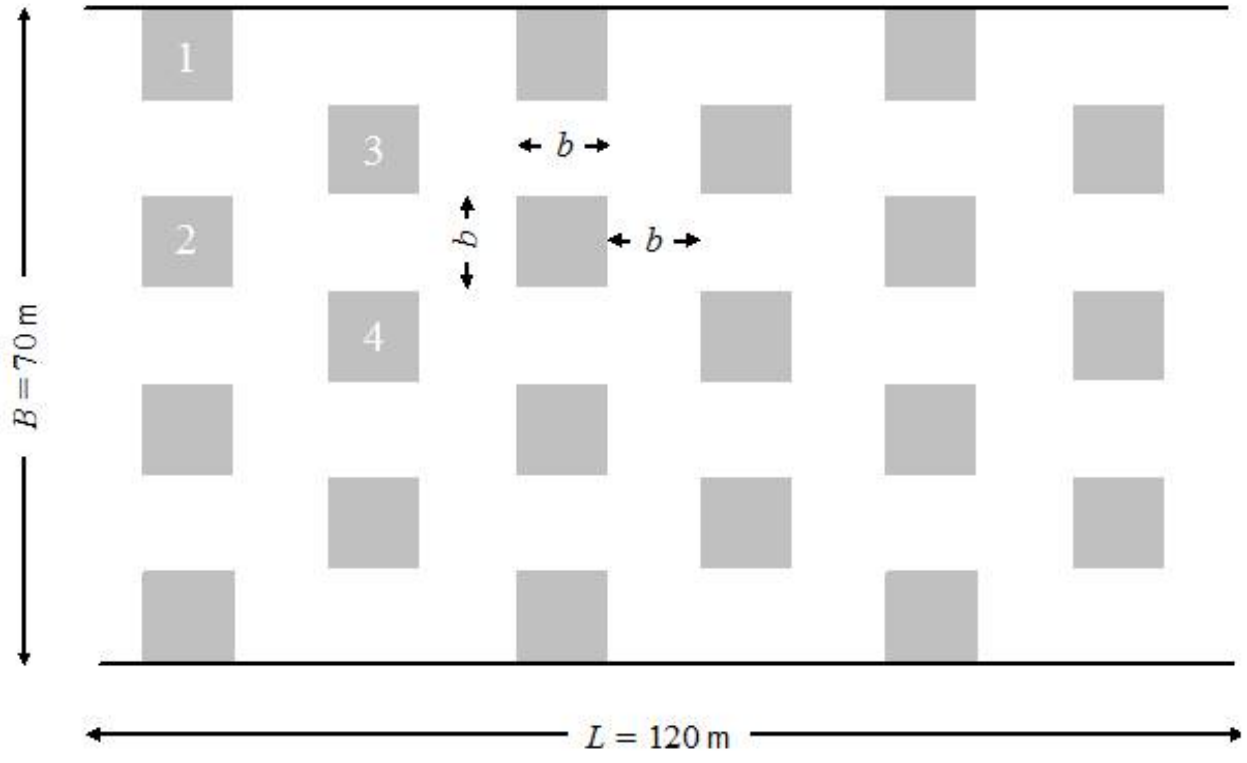

Figure 7–5: Plan view of the open-channel flow through an array of blocks.

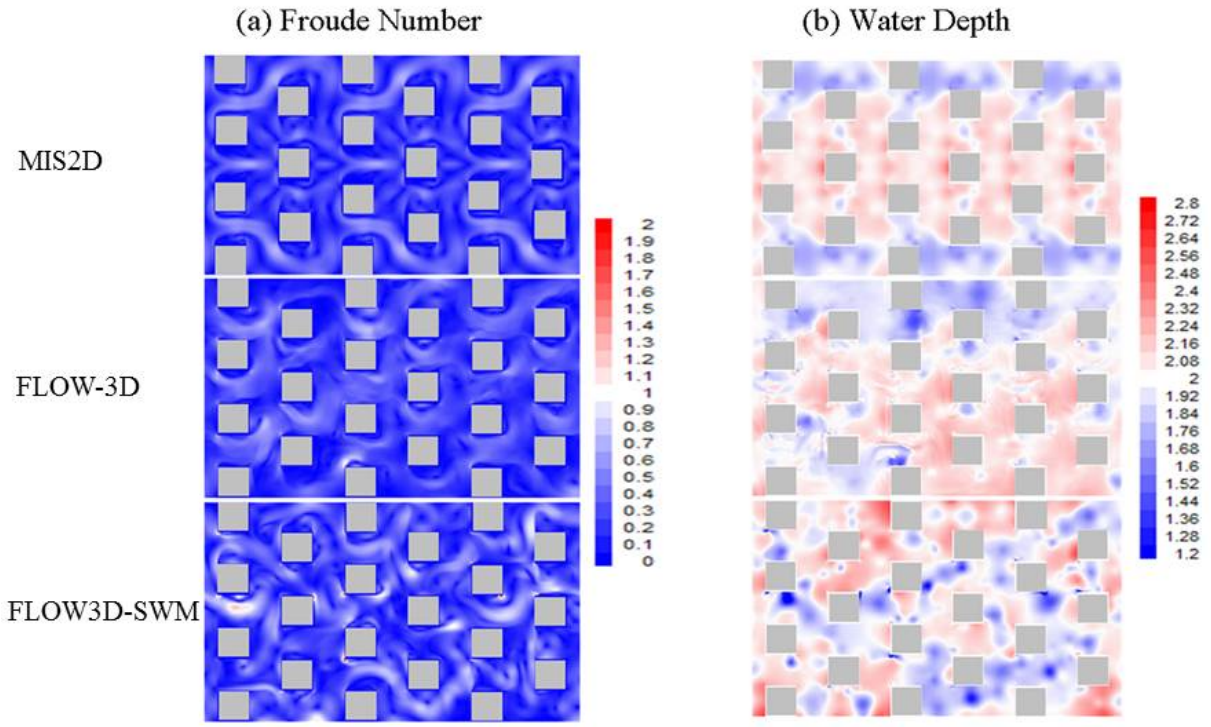

Figure 7–6: Froude number and water depth distribution in a steep open channel on slope $S_o = 0.005$. Top: MIS2D simulation result; Middle: FLOW-3D result; Bottom: FLOW-3D-SWM result.

The flow resistance of the channel is due to the presence of the blocks and the channel friction resistance. In the present simulation, such flow resistance is directly determined by the MIS2D, FLOW-3D, and FLOW-3D-SWM models. The simulations begin with a fixed initial depth of 2 m. Driven by the gravity, the flow through the channel first accelerates and then reaches a quasi-steady state. Figures 7–6, 7–7, and 7–8 show the Froude number and depth maps for the three slopes $S_o = 0.005$, 0.01 and 0.04 respectively using the three simulation methods with the same grid size $\Delta x = \Delta y = \Delta z = 0.5$ m. There are only two fluid layers over the depth of 1 m in the full three-dimensional FLOW-3D simulations. It is shown the MIS2D results give more fluctuations in Froude number and water depth while the FLOW-3D simulation results are less turbulent.

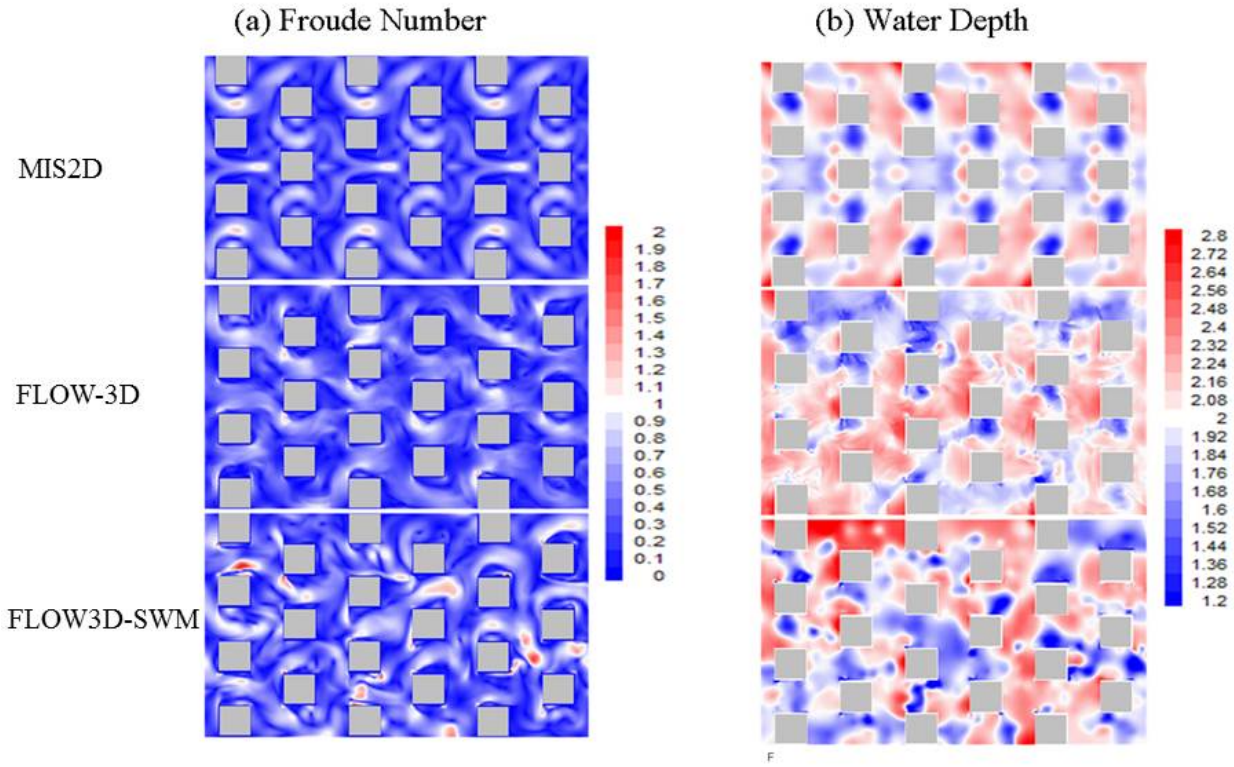

Figure 7–7: Froude number and water depth distribution in a steep open channel on slope $S_o = 0.01$. Top: MIS2D simulation result; Middle: FLOW-3D result; Bottom: FLOW-3D-SWM result.

Since the periodic condition does not allow the water to escape from the computational domain, in each simulation, there is a unique flow rate Q to describe the discharge capacity of the particular channel condition. The total discharge Q through the channel is obtained by integration of the velocity over the channel cross sections. Figure 7–9 compares the time series graph of the discharge rate Q against time t using three methods for three slopes in the same graph. It is found all the simulations follow the same trend. The water flow rate Q starts to accelerate with gravity initially and then reaches a quasi-steady rate. Higher slope yields higher discharge. The quasi-steady flow Q_{qs} is reached when the driven force of gravity is in balance with the resistance to flow by the blocks. The two-dimensional methods MIS-2D and FLOW-3D-SWM give comparable Q_{qs}. However, the three-dimensional method FLOW-3D, gives significant higher quasi-steady flow rate than the two-dimensional methods. Moreover,

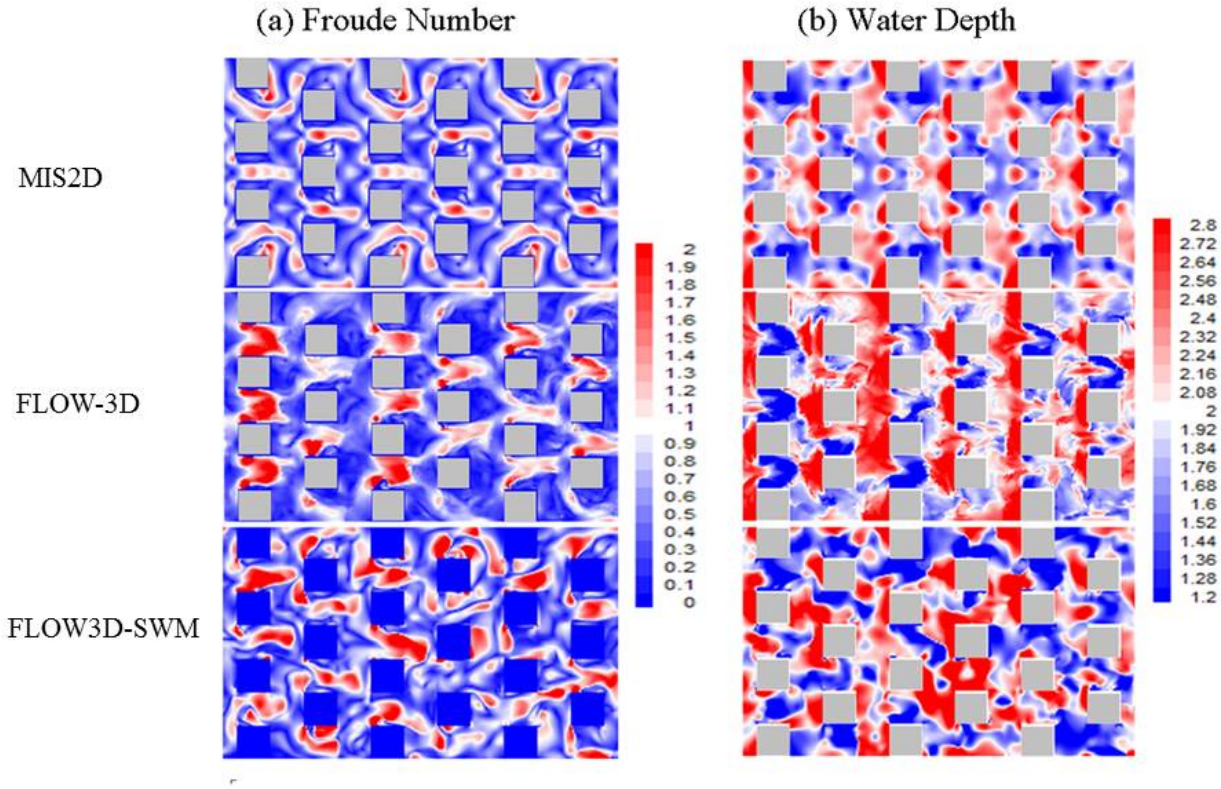

Figure 7–8: Froude number and water depth distribution in a steep open channel on slope $S_o = 0.04$. Top: MIS2D simulation result; Middle: FLOW-3D result; Bottom: FLOW-3D-SWM result.

the graphs of the FLOW-3D flow rate show less fluctuation. In the present calculations, the discharge Q_{qs} is the average of Q over the period from t= 150 s to 300 s. Table 7–1 summaries the results for Q_{qs}. The root-mean-square discharge shows the fluctuation of the flow rate at each time from the average of the quasi-steady rate and it is computed by the formula below and the results are tabulated in Table 7–2.

$$\sqrt{\bar{Q'^2}} = \frac{\sqrt{\sum_{t=150}^{300} (Q(t) - Q_{qs})^2}}{Q_{qs}} \tag{7.5}$$

The root-mean-square discharge is significantly lower for the simulation obtained using the full FLOW-3D model. Although the FLOW-3D-SWM is a 2D model, its root-mean-square value of the discharge is slightly higher. Higher root-mean-square values apparently are associated with scale of the turbulent motions which can be observed from the images

Table 7–1: Quasi-steady state flow rate Q_{qs} (m^3/s) obtained for the three channel slopes S_o = 0.005, 0.01 and 0.04 using MIS2D, FLOW-3D and FLOW-3D-SWM models.

Slope	MIS2D	FLOW-3D	FLOW-3D-SWM
0.005	51.0	80.4	50.8
0.01	70.4	106.4	73.2
0.04	120.7	174.1	140.3

Table 7–2: Root-mean-square discharge $\sqrt{\overline{Q'^2}}$ (m^3/s) for the three channel slopes obtained using the MIS2D, FLOW-3D and FLOW-3D SWM models.

Slope	MIS2D	FLOW-3D	FLOW-3D-SWM
0.005	1.1	0.7	3.3
0.01	2.0	0.8	2.4
0.04	2.4	1.4	3.1

shown in Figures 7–6, 7–7,and 7–8. The scale and nature of the turbulent motions obtained by the three models are clearly different.

The results obtained from the 3D model are more different than the difference between the 2D simulation models. This difference might be explained by the computational mesh is not fine enough particularly in the vertical direction for FLOW-3D model. Because of the limitation in computing power, further mesh refinement is not feasible to fully resolve the three dimensional features. Further more, more artificial resistance might be introduced into the problem to stabilize the three dimensional model in FLOW-3D. This resulting significant higher discharge values and lower RMS fluctuations in all the three slopes than the 2D models. Therefore, the full three dimensional model (FLOW-3D) may not be the best choice to solve this problem. The horizontal length scale is a few folds larger than the vertical scale the 2D models. MIS2D and FLOW-3D SWM appear to be adequate and economical thus represent the reality much better. The MIS2D and FLOW-3D SWM do not produce significantly different results. The subsequent simulations are performed by MIS2D model due to faster computing speed and easiness to set up.

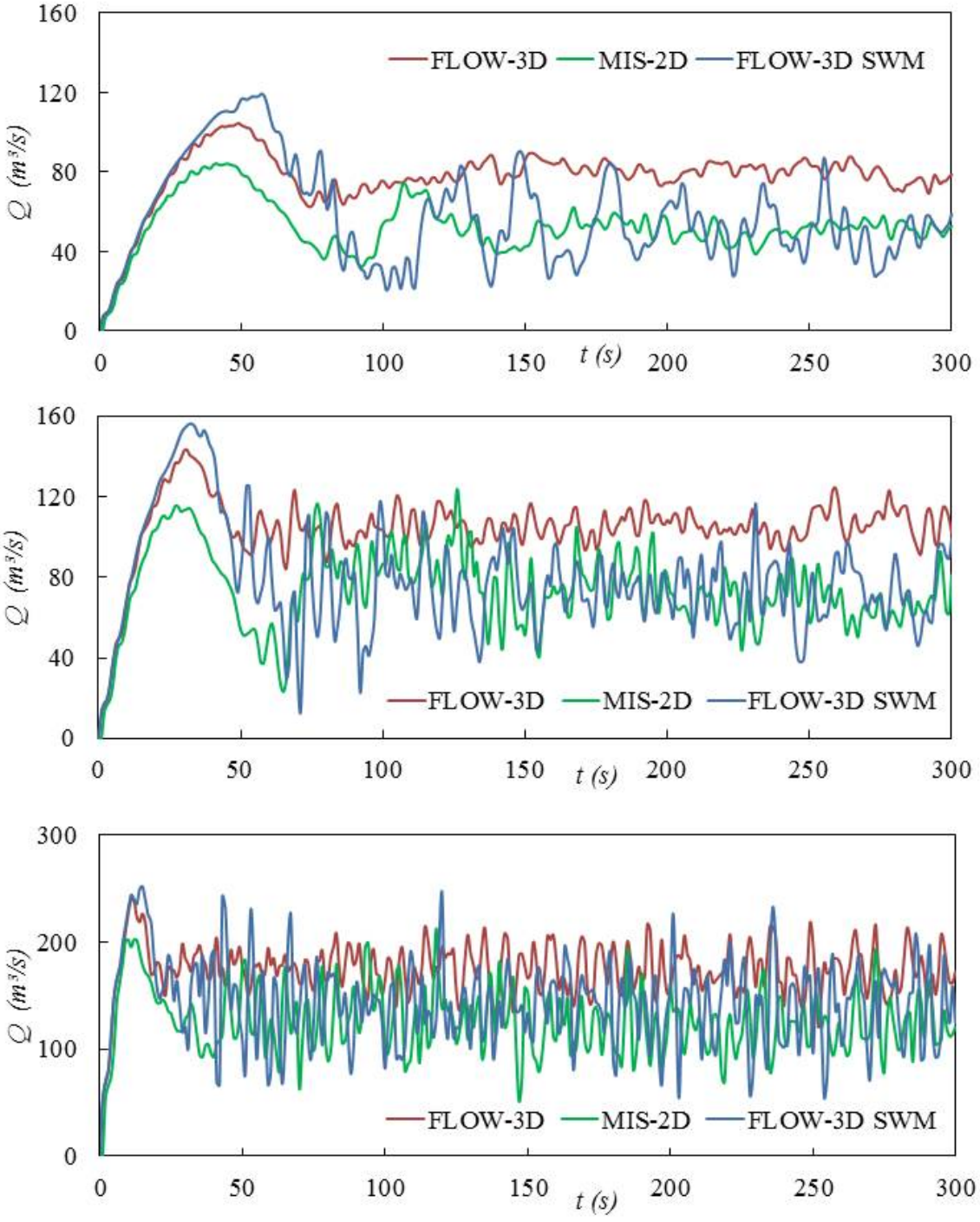

Figure 7–9: Variation of flow rate in $Q(m^3/s)$ with time t (s) for steep open channel flow obtained by the three models MIS2D, FLOW-3D and FLOW-3D-SWM. Top: $S_o = 0.005$; Middle: $S_o = 0.01$; Bottom: $S_o = 0.04$. The quasi-steady-state statistics are determined from the data obtained over a period of time from 150 s to 300 s.

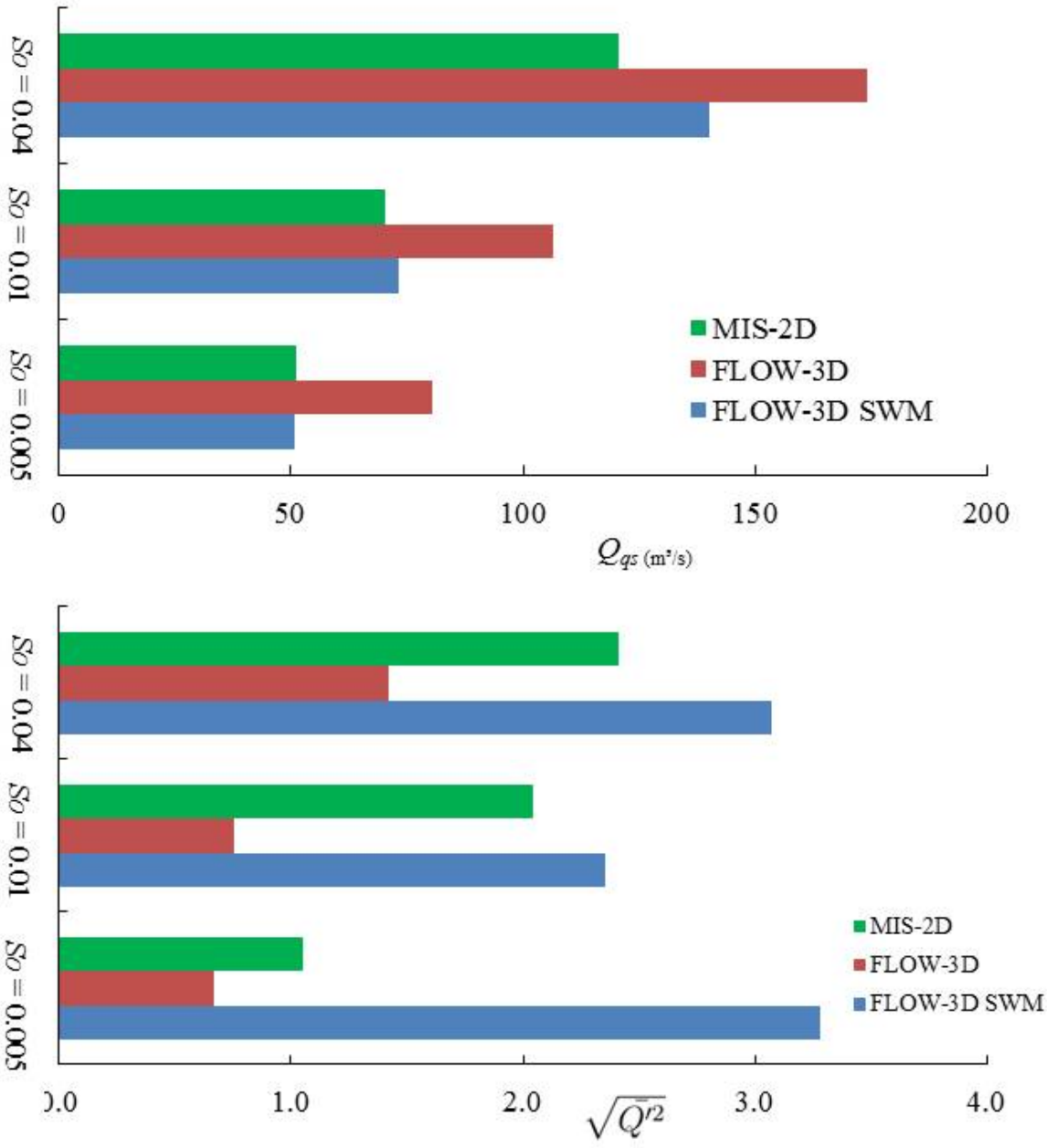

Figure 7–10: Bar graphs for the quasi-steady flow rate Q_{qs} (top), and for the root-mean-square discharge $\sqrt{\bar{Q}'^2}$ (bottom)

7.4.2 Manning Coefficient of Friction

The next series of simulations are performed to study the effect of initial water depth h_o and block size b on the flow resistance passing through an array of blocks as shown in Figure7–5. The simulation begins with a layer of water at rest on a channel of uniform slope S_o using a periodic boundary condition. The velocity in the channel increases under the influence of the gravity. Supercritical flows are created by altering the block width b. Typical of the simulation results of Froude number contours on the plan view are shown in Figure 7–11. At steep slope of $S_o = 0.02$, with small block size ($b = 1$ and $b = 2$), the flow in the channel is essentially supercritical. The Froude number exceeds the value of unity except the regions behind the blocks. With the increase of block size, it is observed constant flow transition occurs frequently at the confined spaces between the blocks. These areas are the critical sections controlled the flow process. The change of color from red to blue in Figure 7–11 marks the location of the hydraulic jump where significant energy dissipation occurs as the supercritical flow returns to its subcritical state. The wall-and-bed friction drag is represented by the Manning coefficient n_{macro}. The form drag can be calculated from the depth averaged flow obtained from the simulations.

The total flow rate Q eventually reaches a quasi-steady state as described in previous sections. The value of the quasi-steady discharge Q_{qs} is determined from the plot of Q versus time. In the quasi-steady state, the friction slope is equal to the bottom slope S_o and the discharge on the average is the quasi-steady discharge Q_{qs}. Given a Manning bed-and-wall friction coefficient n_{bed}, a macro Manning coefficient n_{macro} is determined from the quasi-steady flow rate Q_{qs} using the following formula:

$$Q_{qs} = \frac{1}{n_{\text{macro}}} A R^{\frac{2}{3}} S_o^{\frac{1}{2}} \tag{7.6}$$

The macro Manning coefficient n_{macro} is a catch-all parameter for the overall resistance of the blocks to the flow. The values of this overall resistance coefficient for different water

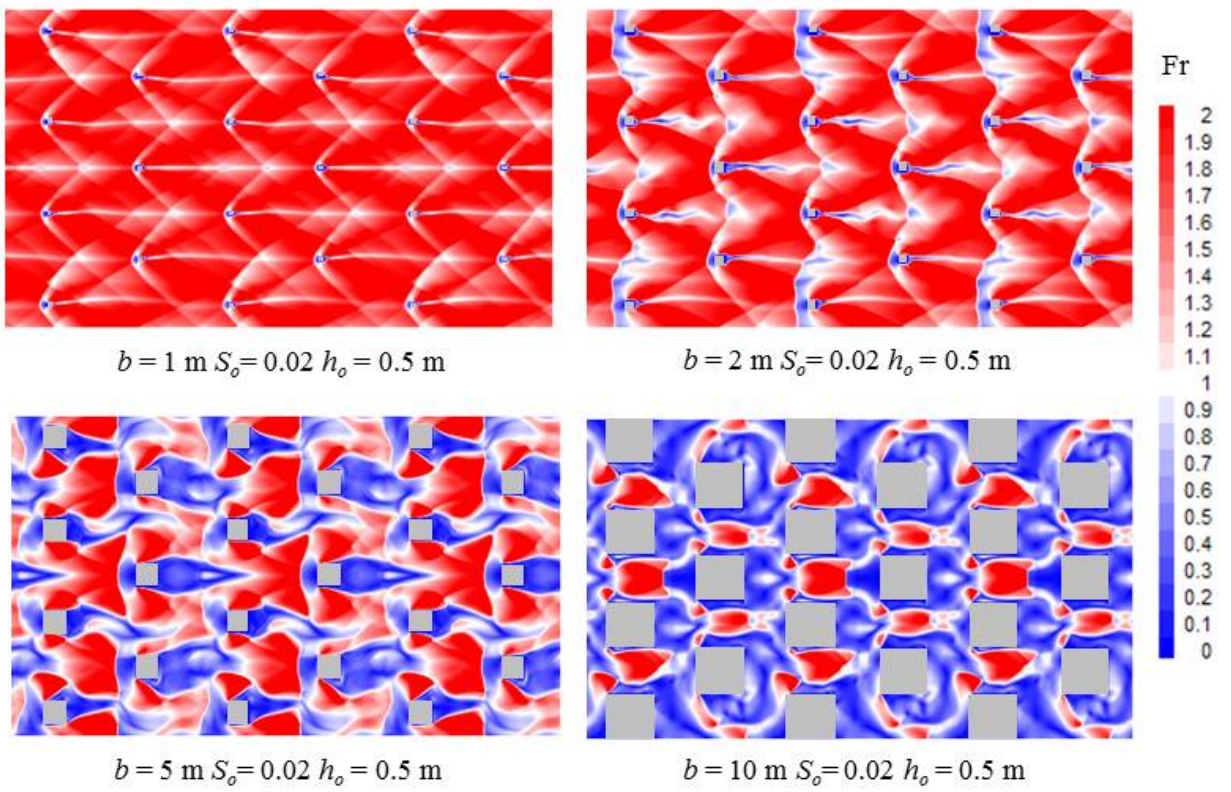

Figure 7–11: Froude number distribution of the flow around the blocks of different sizes $b =$ 1 m, 2 m, 5 m and 10 m in channel of average water depth $h_o = 0.5$ m on a slope $S_o = 0.02$ at time $t = 300$ s

depth $h_o = 0.5$ m, 1 m, 2 m and 4 m are given in Figure 7–12 for one channel of slope $S_o =$ 0.01. The corresponding time series plots of the flow rate Q_{qs} is given in Figure 7–13.

In the limiting of small water depth, the macro coefficient is the same as the friction coefficient; i.e.,$n_{\text{macro}} = n_{bed}$. It increases with the depth to a value as high as $n_{\text{macro}} \simeq 0.12$ when the water depth reaches $h_o = 4$ m. When the block size is small, the blocks would not contribute much on the channel resistance and there is less interaction between the blocks and water. Therefore, the computed n_{macro} is only slightly larger than the specified Manning coefficient n_{bed}. As the size of the blocks increases, water is constrained in the areas between the blocks. Those areas are the control sections of the flow which determine the upstream discharge. The form drag is the dominant resistance to flow, when the water is sufficiently deep and when the dimensions of the obstruction are comparable to the width of the flow.

Although the Manning formula is widely used in calculation based on the one-dimensional (1D) hydrodynamic model such as Hec-Ras, the value of the macro coefficient selected for the 1D simulation would be invalid if the macro coefficient n_{macro} changes with the depth. The value of the macro Manning n_{macro} obtained from in-situ measurement at low flow would not be the same at flood stage when the water depth is greater than the water depth during the in-situ measurement.

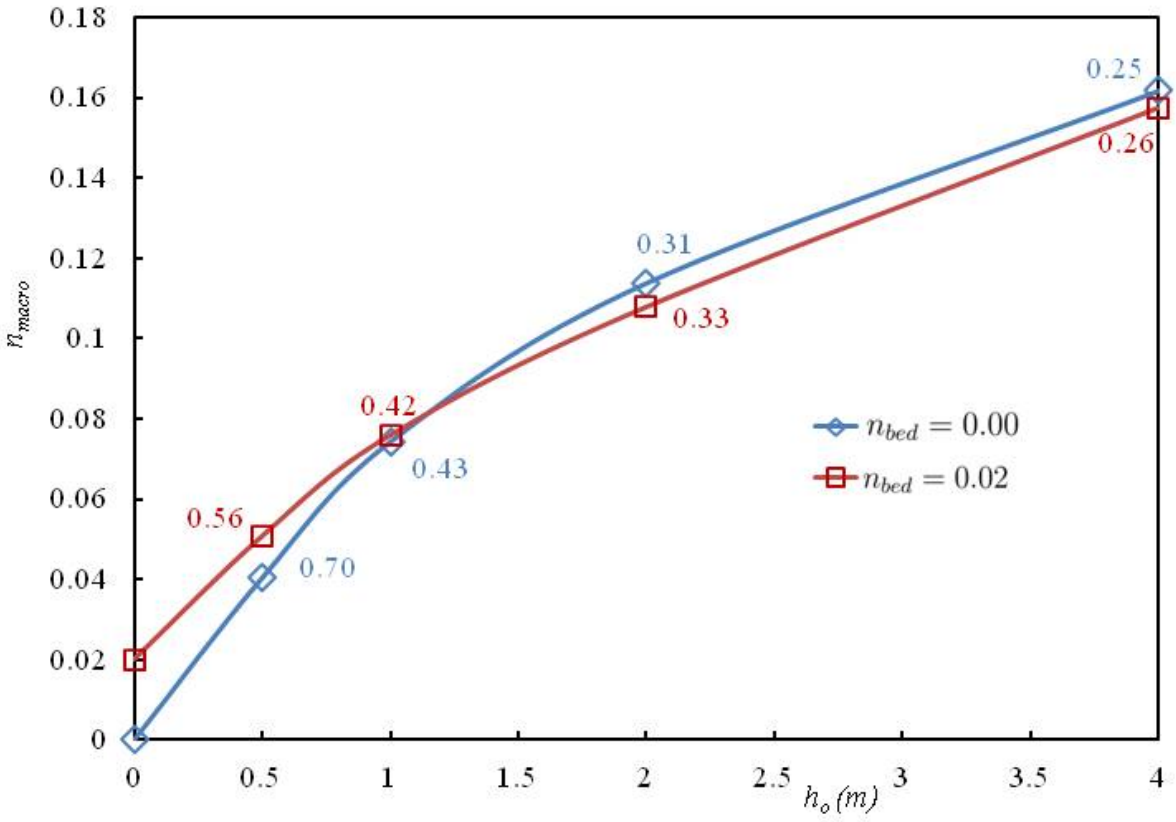

Figure 7–12: Macro coefficient of friction n_{macro} in a channel with an array of blocks; block size is fixed at $b = 5$ m and the slope is fixed at $S_o = 0.01$. The depth is differnt $h_o = 0.5$ m ,1 m ,2 m and 4 m. The label on the side shows the averaged Froude number in the channel

7.4.3 Form Drag Coefficient

For large scale obstructions, the resistance to flow is due to the friction drag and the form drag. The friction drag follows the correlation of the Manning formula. The form drag

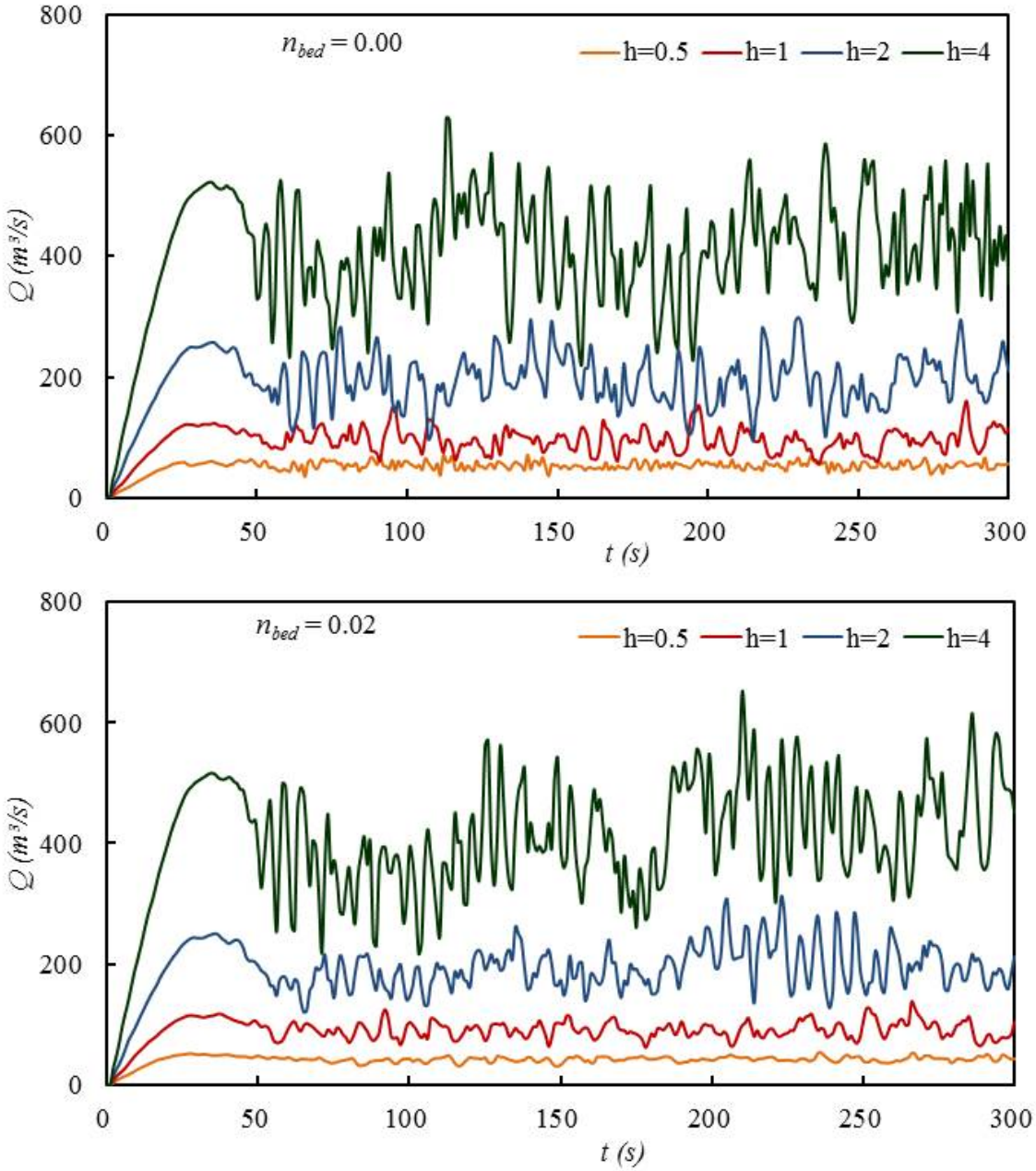

Figure 7–13: Total flow rate Q versus time t on a channel of slope $S_o = 0.01$ for water depth $h_o = 0.5$ m, 1 m, 2 m and 4 m. The bed-and-wall Manning coefficient $n_{bed} = 0.00$ and 0.02. For a fixed block size $b = 0.5$ m, the quasi-steady discharge Q_{qs} is dependent on the water depth

on the other hand is defined by the averaged drag coefficient as follows:

$$\tilde{C}_D = \frac{\tilde{F}_D}{\tilde{A}_f \, \frac{1}{2}\rho \tilde{V}^2} \tag{7.7}$$

There are 21 blocks over the length of the channel L. In quasi-steady state, the averaged drag force is equal to the averaged weight component of the fluid in the direction of the inclined; i.e.,

$$\tilde{F}_D = \rho g L [\frac{B h_o - 21 b^2}{21}] \sin\theta \tag{7.8}$$

The frontal area of the block is

$$\tilde{A}_f = b h_o \tag{7.9}$$

The averaged velocity is the quasi-steady flow rate Q_{qs} divided by the pore cross-sectional area and then weight averaged as follows:

$$\tilde{V} = \frac{Q_{qs}}{h_o(B-4b)}\frac{2b}{B} + \frac{Q_{qs}}{h_o(B)}\frac{B-4b}{B} + \frac{Q_{qs}}{h_o(B-3b)}\frac{2b}{B} \tag{7.10}$$

The average drag coefficients calculated according to Eq. 7.7 from the simulation are shown in Fig. 7–14 to be relatively independent of the water depth unlike the macro coefficient n_{macro} in Fig. 7–12. It is clear the drag-coefficient relation according to Eq. 7.7 is a better correlation in this case when the maximum blockage to the flow $4b = 4 \times 5 = 20$ m which is comparable to the total width of the flow of $B = 70$ m. The form drag and friction drag follow an opposite relation to depth. The flow resistance increases with the water depth according to the drag-coefficient correlation, and decreases with the depth according to the Manning formulation.

7.4.4 Unsteady Drag Coefficient

The drag coefficient computed by Eq. 7.7 is an average value. It is introduced assuming the flow in the channel has reached a steady state. The instantaneous drag force F_D on the block is computed directly from the numerical simulation by integrating the hydrostatic

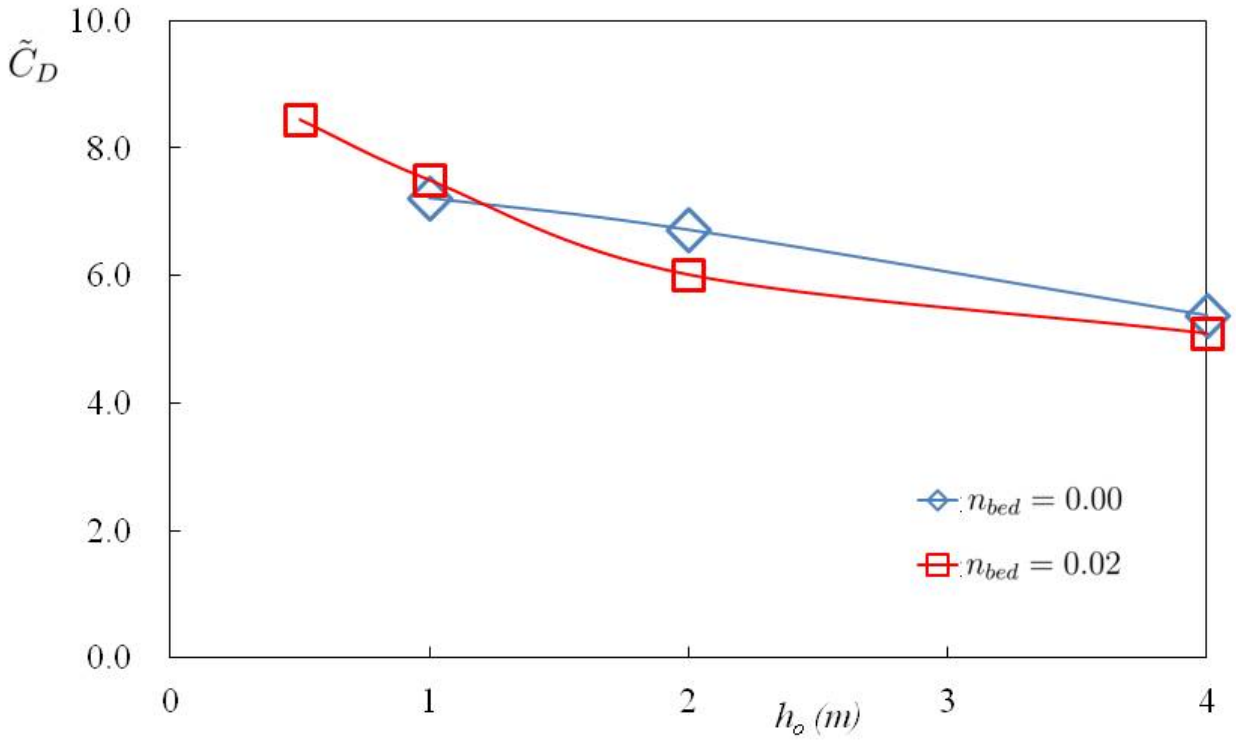

Figure 7–14: Average drag coefficient $\tilde{C}_D$ in a channel with an array of blocks with block width b= 5 m, depth $h_o = 0.5$ m ,1 m ,2 m ,and 4 m at slope $S_o = 0.01$.

pressure in the front face and at the back face of each block as follows:

$$F_D = \sum \frac{1}{2}\rho g h_{\text{front}}^2 \Delta y - \sum \frac{1}{2}\rho g h_{\text{back}}^2 \Delta y \tag{7.11}$$

This instantaneous force F_D has a very different magnitude compared with the averaged force $\tilde{F}_D$ given by Eq. 7.8 because the water depth is highly variable due to the formation of hydraulic jumps in the steep open-channel flow. Figure 7–15 shows the variation of depth for the case of the block size $b = 5$ m, the channel slope $S_o = 0.04$ and average depth $h_o = 0.5$ m. The maximum and minimum depths in the channel in this case are very different. Water piles up in the front face of the blocks. It reaches three times higher than the average depth $h_o = 0.5$ m. Since the flow through the blocks is unsteady, the drag force depends on time and space. The instantaneous force is directly calculated using Equation 7.11. The time and spatial variations of the drag coefficient obtained from the direct calculation is shown in Fig.

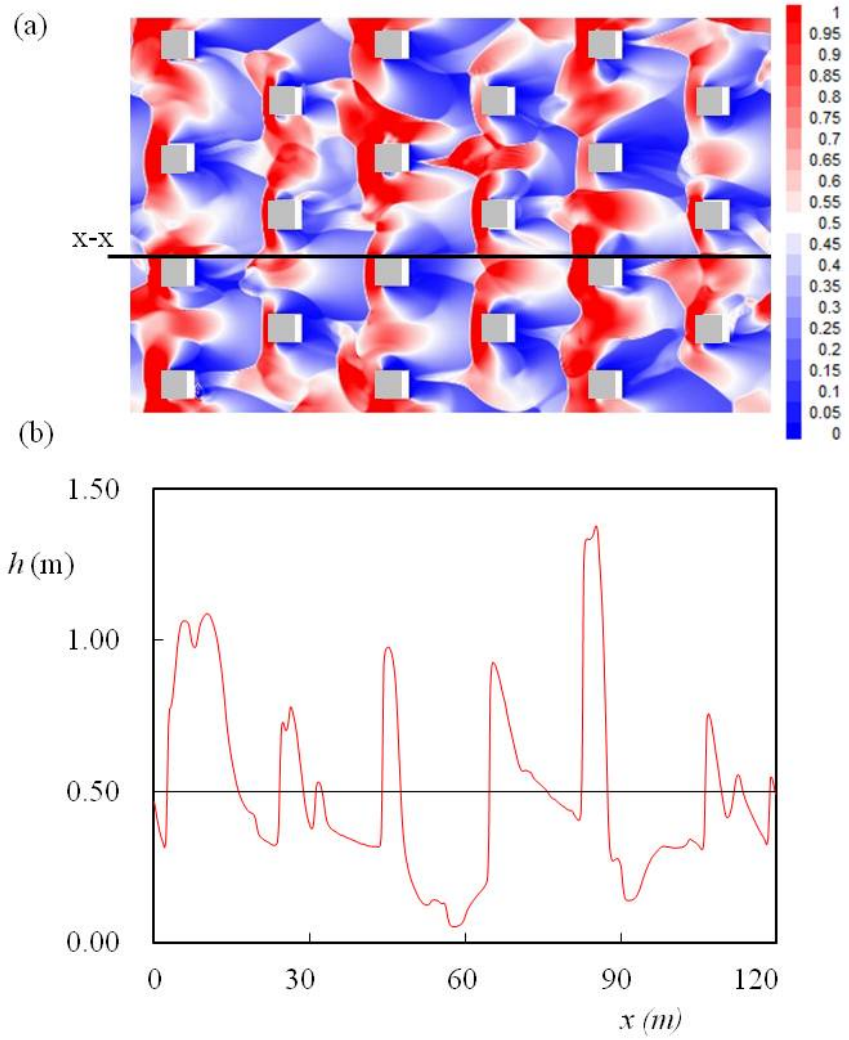

Figure 7–15: (a) Map in plan view showing the depth variation for the channel flow through array of blocks; block size $b = 5$ m, channel slope $S_o = 0.04$ and average depth $h_o = 0.5$ m. (b) Depth profile through the cross-section x-x.

7–16, where the drag coefficient C_D is plotted versus time t for four distinctive blocks no.1, no.2, no.3 and no.4 (Fig. 7–5) for the numbering of the blocks. The variation of the drag coefficient is huge particularly on block no.4. The value of the unsteady drag coefficient for block no.4 varies from the low value of $C_D = 0.1$ to the high value of $C_D = 27$. This 270 folds changes of the unsteady coefficient on the blocks is conceptually significant because the incipient motion of the rocks and boulders does not depend on the averages $\tilde{C}_D$ but rather is determined by the peaks of the force and moment in the highly unsteady flow.

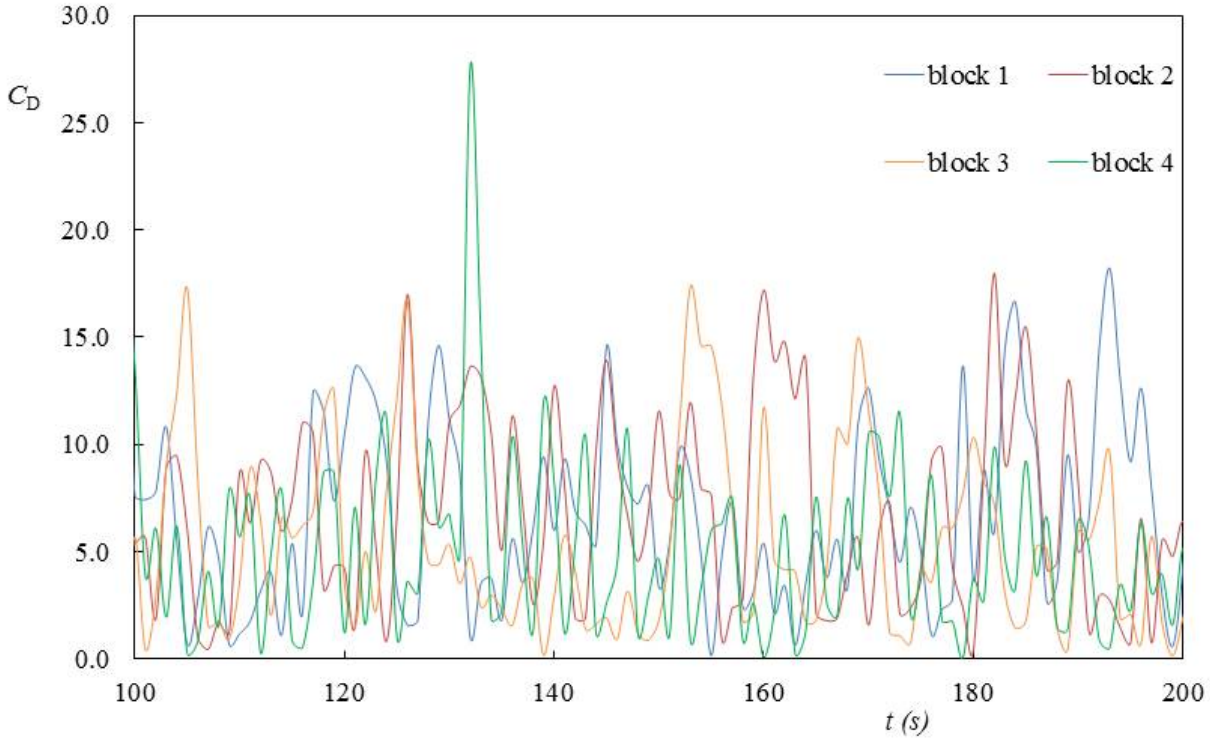

Figure 7–16: The unsteady drag coefficient C_D with block size $b = 5m$, depth $h_o = 4$ m at slope $S_o = 0.01$ for Block 1, 2, 3, and 4 from $t = 100$ s to 200 s

7.5 Flood Routing Through a Meandering Channel

The existence of the form drag over the friction drag is anticipated in many steep open-channel flow through large obstruction. The flood through a meandering river as shown in Figure 7–17 is another example. The numerical simulations for the flow through the meandering river are again carried out using MIS2D solver as shown before. The simulation starts with a layer of water at rest. The gravity along the incline accelerates the flow toward the quasi-steady state. The periodic boundary conditions produce the meander of infinite length. The flow is triggered by altering the channel bottom slope S_o. Figure 7–18 shows the vorticity profiles of the flow obtained for four channel slopes of $S_o = 0.0025$, 0.005, 0.01, and 0.02 and two Manning coefficients $n_{bed} = 0.00$ and $n_{bed} = 0.02$.

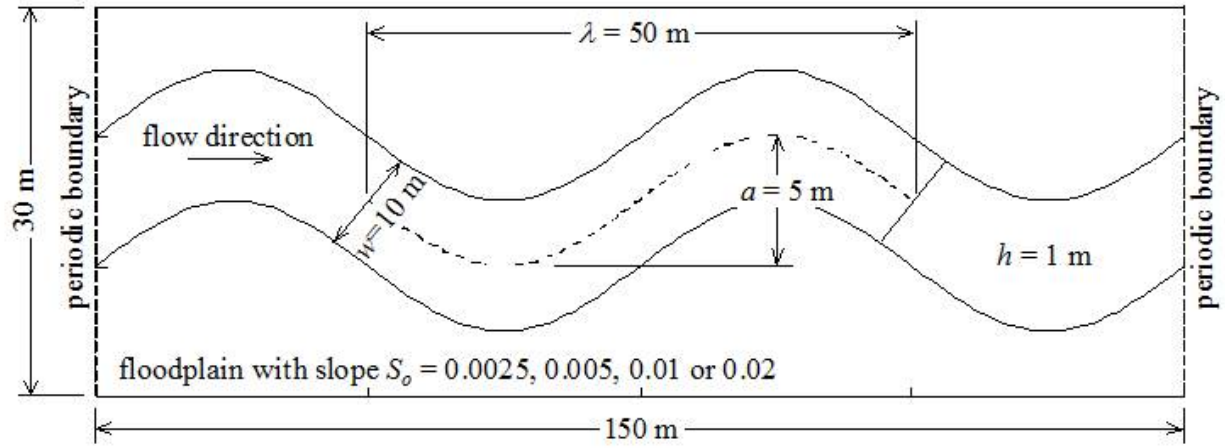

Figure 7–17: Meandering river of meander amplitude a, width w, water depth h and wave length λ on a channel of slope S_o.

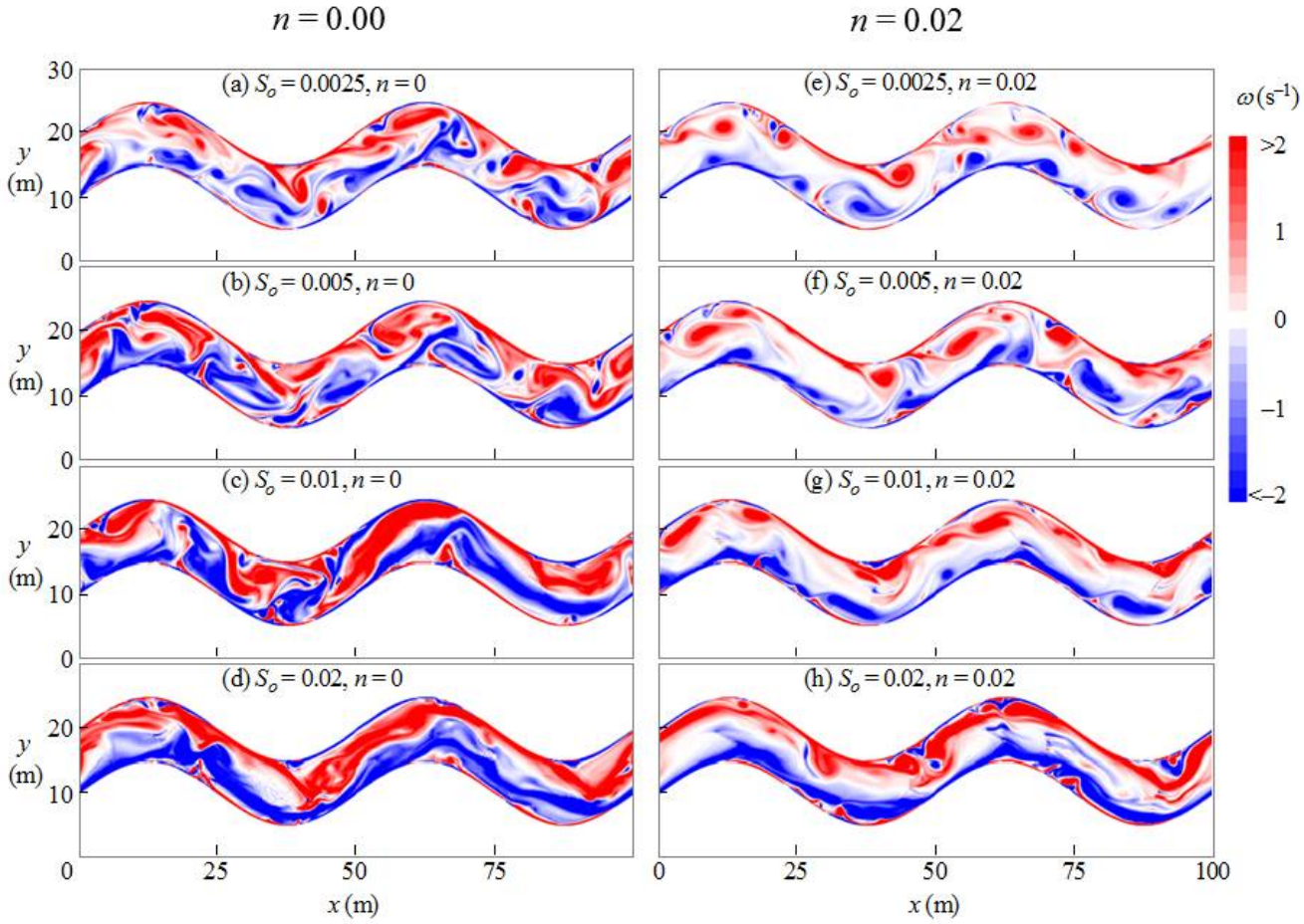

Figure 7–18: Vorticity contours in the meandering rivers of bed slope S_o = 0.0025, 0.005, 0.01, 0.02 and Manning coefficient n_{bed} = 0.00 and n_{bed} = 0.02 at time t = 250 s.

Figure 7–19 and Fig. 7–20 show the variation of the total discharge Q with time t for the meanders with Manning bed-and-wall coefficient $n_{bed} = 0.00$ and $n_{bed} = 0.02$. The discharge accelerates with time initially at a rate that is equal to the gravity force along the incline. It eventually attains a terminal state of a quasi-steady discharge Q_{qs} when the resistance force is exactly equal to the driving force of the gravity. In the case of $n_{bed} = 0.00$, although bed-and-wall friction is zero, the flow approaches a quasi-steady state. Since the friction force is zero, the resistance to flow is entirely due to the form drag which is produced by the turbulence and waves as the flow negotiates through the meander. The macro coefficient n_{macro} is found using the quasi-steady flow rate Q_{qs} as before based on the Manning's Equation in Eq. 7.6. Figure 7–22 plots the results of the macro coefficient n_{macro} with averaged depth h_o. Again, the macro coefficient n_{macro} is found to be strongly dependent on the depth.

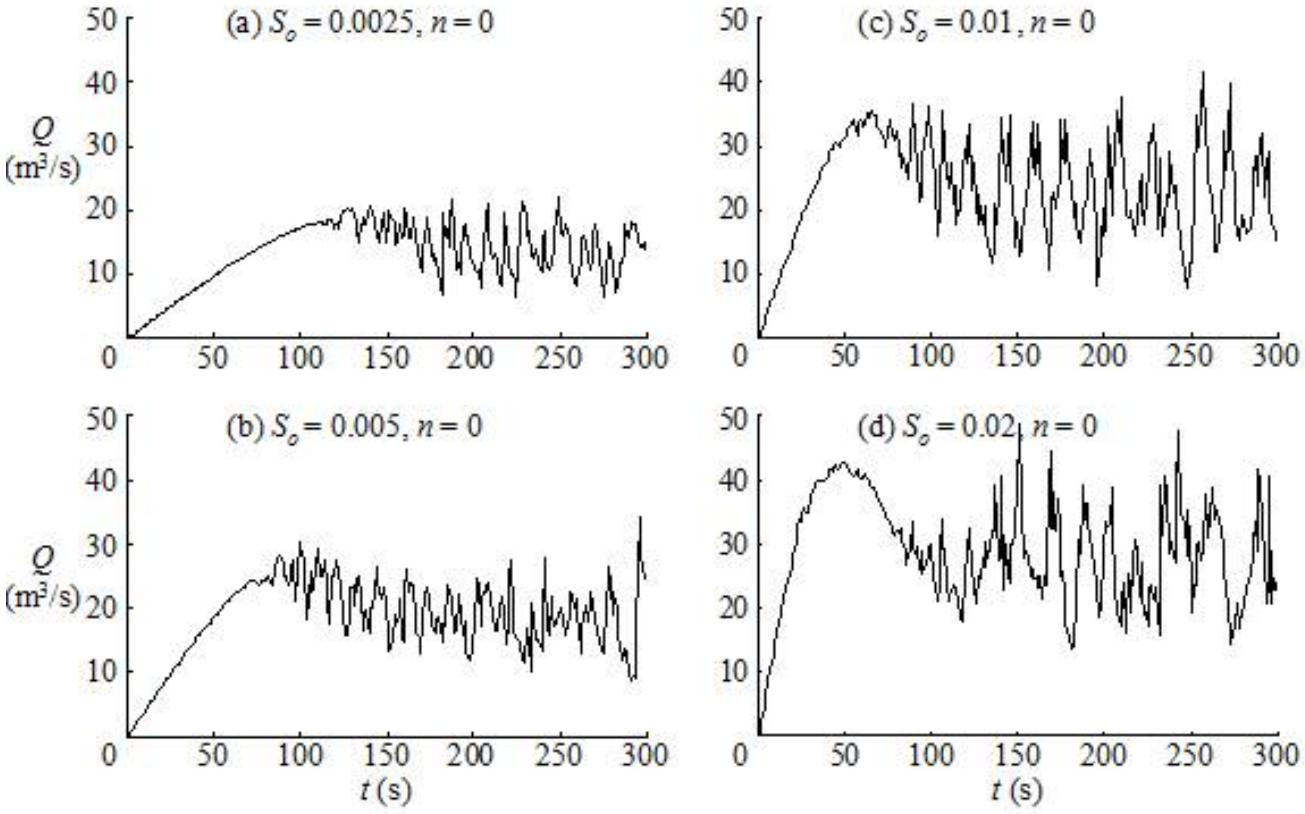

Figure 7–19: Quasi-steady state flow rate in meandering river with Manning coefficient for the bed $n_{bed} = 0.00$. Computations are conducted using grid size $\Delta x = 0.083$ m

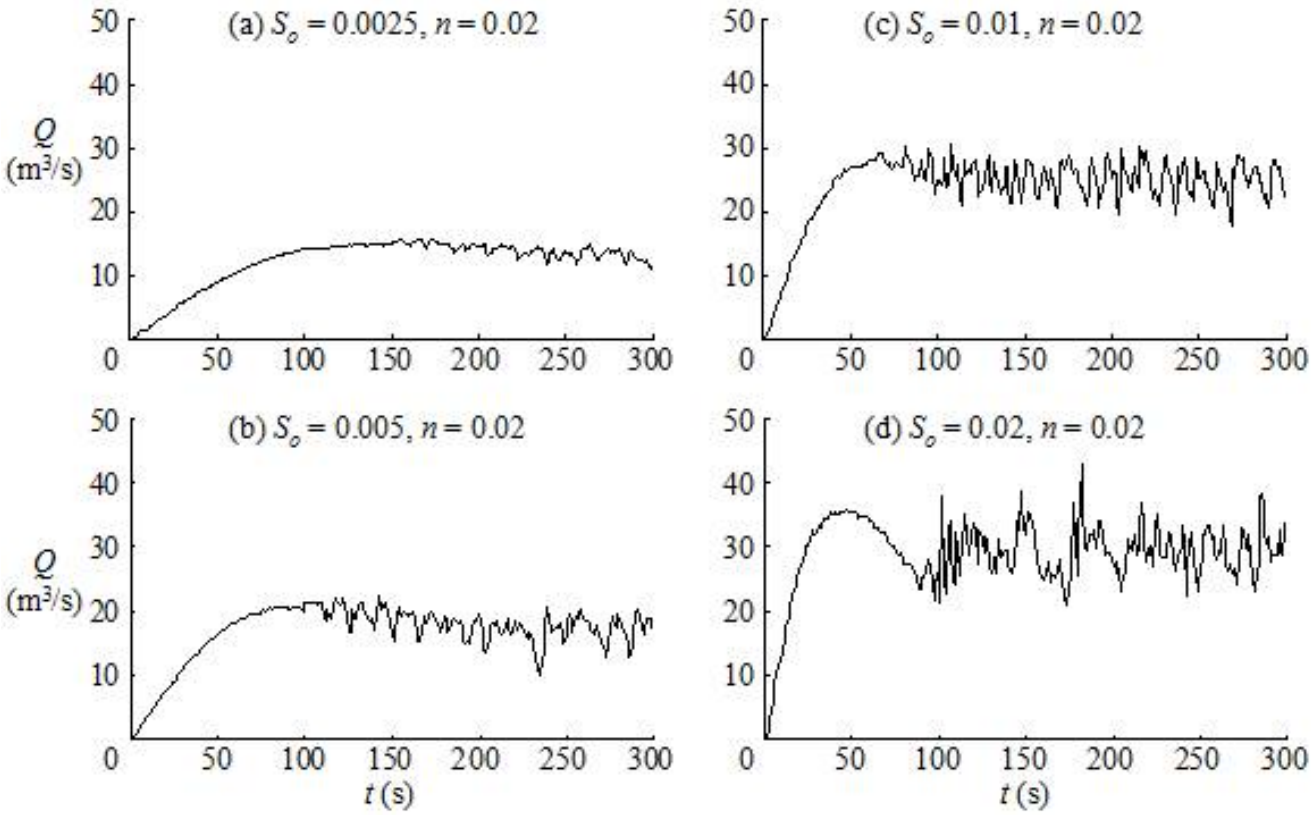

Figure 7–20: Quasi-steady state flow rate in meandering river with Manning coefficient for the bed $n_{bed} = 0.02$. Computations are conducted using grid size $\Delta x = 0.083$ m.

As shown in Figure 7–21, the macro coefficient n_{macro} is not a constant but dependent on the channel slope S_o. A series of simulation is performed using the same approach by fixing the slope $S_o = 0.01$ and changing depth h_o to 0.5 m, 1 m, 2 m and 4 m. If the Manning equation is valid, the Manning coefficient should be a constant that depends neither on the slope nor on the depth. However, macro coefficient is observed to increase with slope as well as depth. These results are significant. It points to the fact that the Manning formula is not correct for evaluating the flow resistance due to large scale features such as the meander.

Since the Manning formulation is not valid in this case, a correlation for the form drag is attempted. In the quasi-steady state, the drag force is equal to weight of the water along the incline. For the meandering river the weight along the incline is

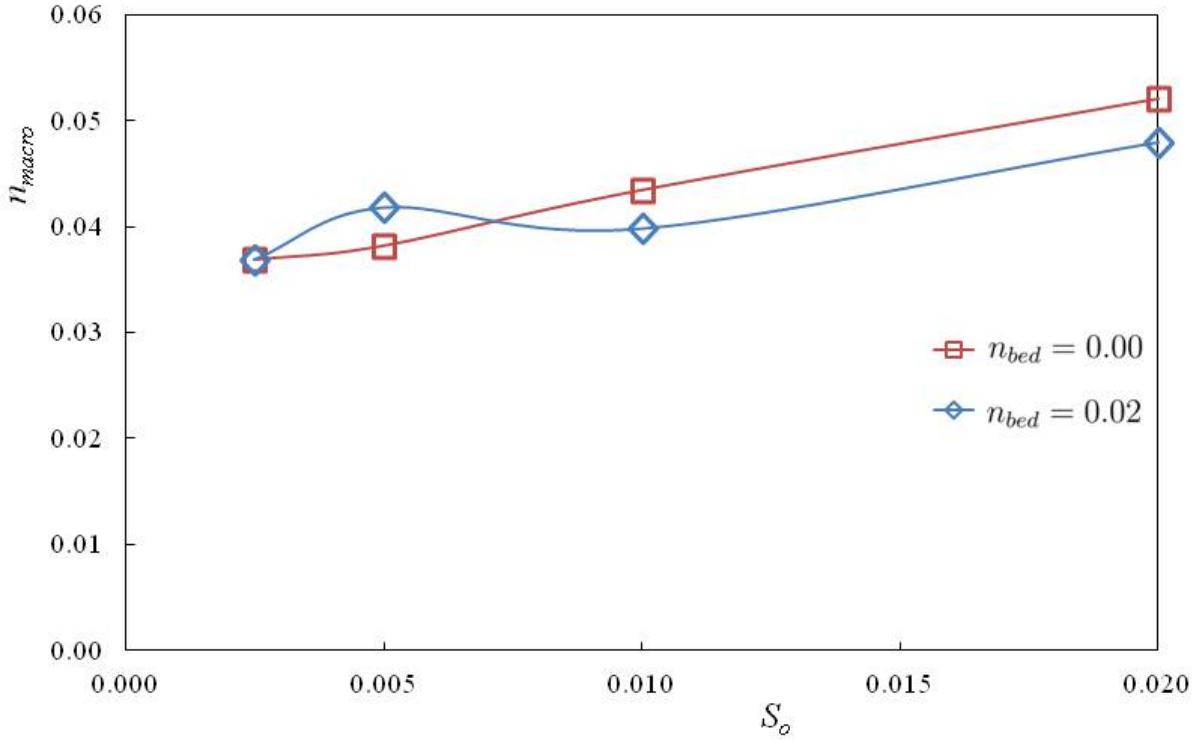

Figure 7–21: Macro Manning coefficient of friction n_{macro} in the meandering channel of slope $S_o = 0.0025$, 0.005, 0.01, and 0.02.

$$\tilde{F}_D = \rho g B L_s h_o \sin\theta \tag{7.12}$$

where L_s is the arc length of the sinusoid. The frontal area is

$$\tilde{A}_f = a h_o \tag{7.13}$$

where a is the amplitude of the meander. The velocity through the meandering channel is simply

$$\tilde{V} = \frac{Q_{\text{qs}}}{w h_o} \tag{7.14}$$

With $\tilde{F}_D$, $\tilde{A}_f$ and $\tilde{V}$ as given in the above equations, the averaged drag coefficient $\tilde{C}_D$ is calculated using Eq. 7.7 for the meandering river. Figure 7–23 shows the results. The drag coefficient is relatively independent of the water depth suggesting the form drag is the

dominant process in this particular meander river with a channel width $w = 10$ m and a meandering amplitude of $a = 5$ m.

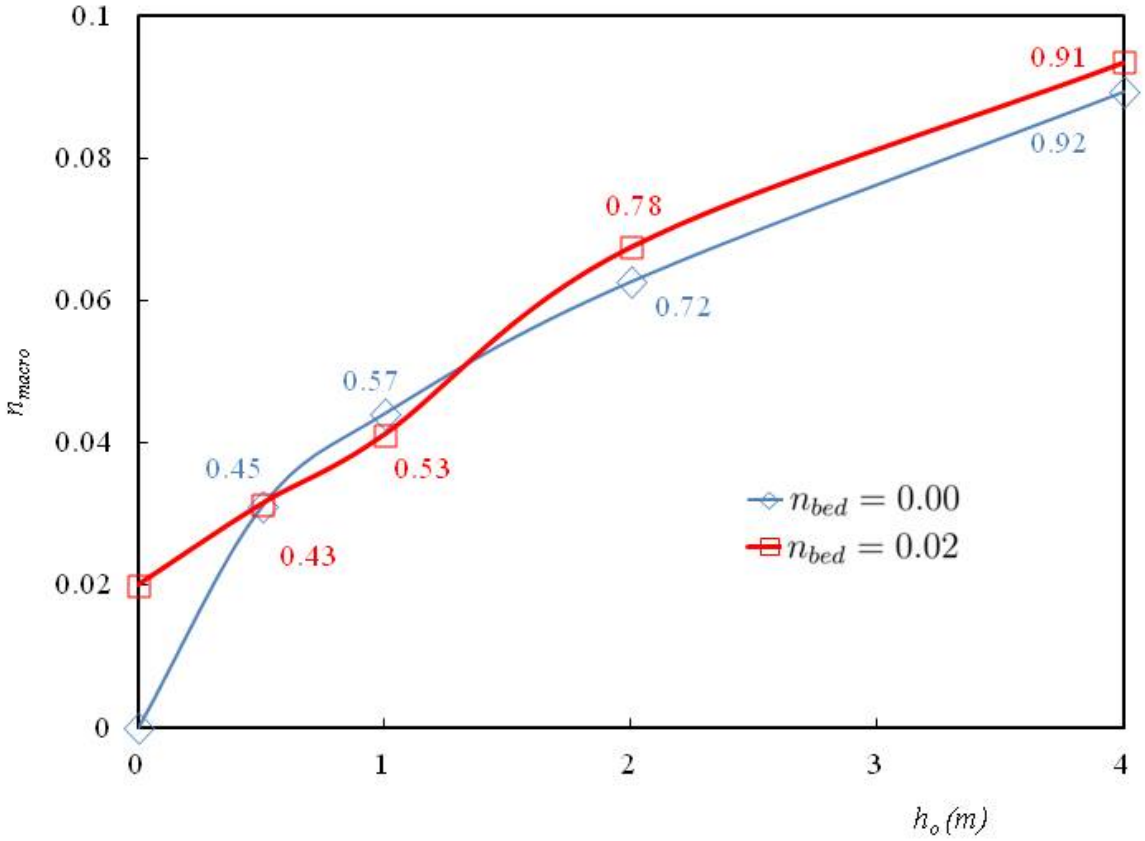

Figure 7–22: Macro Manning coefficient of friction n_{macro} in the meandering channel of depth $h_o = 0.5$ m,1 m ,2 m and 4 m on a slope $S_o = 0.01$. The label on the side shows the averaged Froude number in the channel.

7.6 Conclusion

The results of numerical simulations have shown that the resistance to the flow in open channels is a combination of the friction drag and the form drag. Although the selection of the Manning friction coefficient n_{bed} has been the practice in one-dimensional hydrodynamic modeling such as Hec-Ras, it is important to recognize that this coefficient may also depend on the depth of the flow. The macro coefficient n_{macro} obtained from in-situ measurement at low flow rates may have a very different value at flood stage. The friction drag may be specified by the Manning coefficient of friction. The form drag on the other hand is

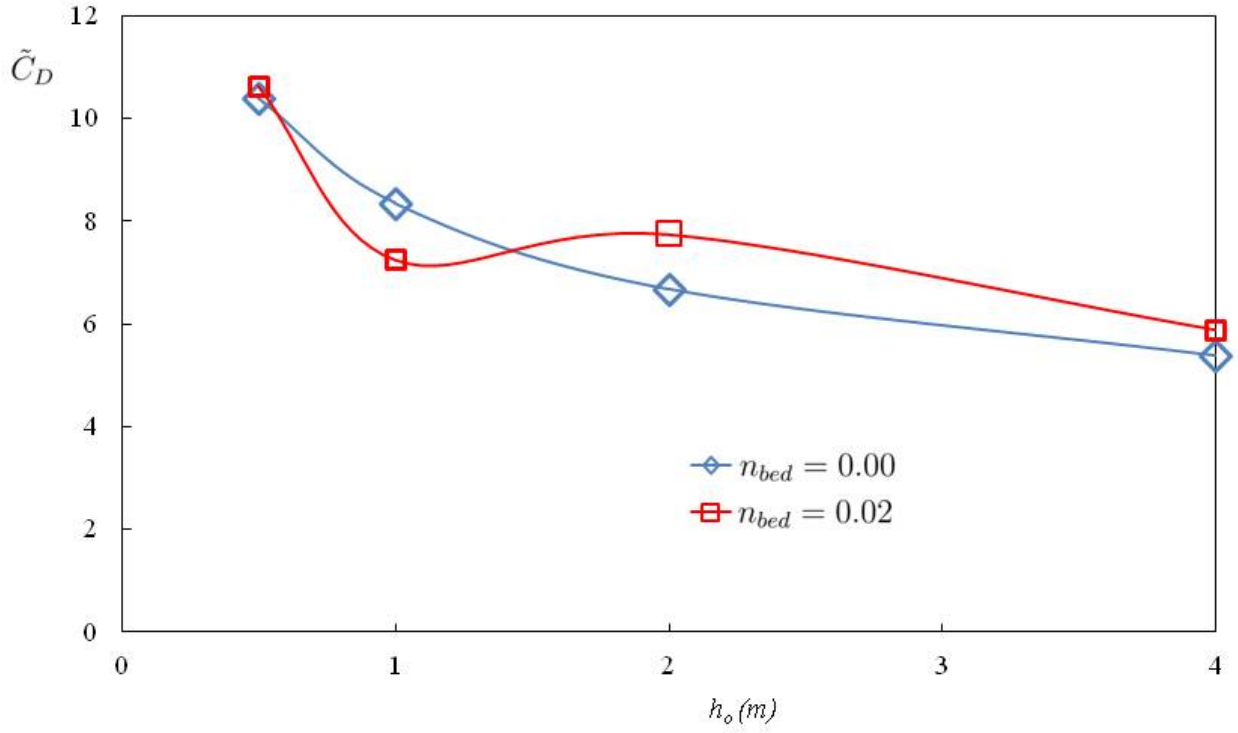

Figure 7–23: Averaged drag coefficient $\tilde{C}_D$ in the meandering channel of depth $h_o = 0.5$ m,1 m, 2 m and 4 m on a slope $S_o = 0.01$.

more appropriately determined by the drag coefficient. The two kinds of flow resistance follow entirely opposite dependences on the water depth. When the size of the obstacles is comparable with the size of the channel, the form drag is the dominant resistance in the channel and the drag coefficient could be determined from numerical calculations. The direct numerical simulation also will provide the force and moment calculation that is critical in the determined incipient motion of rocks and boulders in the highly unsteady flow through the mountain stream. The peak values of the force and moment obtained from the direct numerical simulations is significantly greater than the averages. These differences must be factored in the model for rock-and-boulder transports in steep rivers and in the model of debris flow produced by floods and Tsunami.

CHAPTER 8

CONCLUSION

8.1 Summary

A series of numerical simulations and laboratory experiments has been carried out for a number of problems for shallow water flow in open channels focusing on the wave effects on turbulence in high-speed shear flow with large Froude numbers. A robust hydrodynamic solver of consistent transport is developed to perform direct numerical simulations. The fifth order WENO scheme is used to interpolate the face values and control the numerical oscillations by locally switching the scheme to third order. The spurious oscillations also have been managed using the flux limiter using the minimal intervention strategy (MIS2D). The accuracy of the WENO scheme is demonstrated by the convergence study of the linear growth rate and the maximum kinetic energy of the jet/wake. The fractional error is smaller than 0.1%. The accuracy of MIS2D model is demonstrated by comparing the dam-break wave simulation with the exact solution and the solution obtained from FLOW-3D.

8.1.1 Instabilities of Jet and Wake Flow in Shallow Waters at High Froude Number

Direct numerical simulations of the instability in shallow water associated with base flow that has the jet/wake hyperbolic secant profile are performed. The simulations cover a wide range of Froude number from Fr =0.05 to 4.0. The dominant instability involves both the sinuous and varicose modes when the convective Froude number is small, but only the varicose mode when the convective Froude number exceeds the critical value of about 2.8. These calculations of shear instability for the SECH velocity profile is most significant in the study of high-speed currents when the convective Froude number is greater than the value

of unity. The results are consistent with previous study of the analogous problems in gas dynamics.

8.1.2 Non-linear Transition of Jet/Wake Instability in Shallow Flows

The simulations to study the transition of jet/wake instability to turbulent flow in shallow flows are extended to the non-linear stage for both subcritical flow and supercritical flow. A small perturbation of the most unstable wave length is introduced to the jet/wake that has a hyperbolic secant velocity profile. The simulations track the rapid increase in the kinetic energy of the disturbance and the modification to the mean flow during the nonlinear transition. Aspect ratio of the eddy and eddy-shoklet shows agreement with available experimental data. The transition to turbulence depends on the relative velocity but not on the absolute velocity in the free-stream. Waves play a significant role in the transition. Significant reduction in mass and momentum exchanges is observed with the increase in value of the Froude number. The effect of the waves on the exchanges is classified according to the Froude number as subcritical, trans-critical and supercritical on the transition. To capture the flow discontinuities in the numerical simulations, the spatial interpolation over a stagger grid is by a fifth-order WENO scheme. A fourth-order Runge-Kutta method advances the calculations in time. The orders of convergence are 2.6, 3.4 and 1.7 for the simulations of the transition at the Froude number of 0.5, 2.4 and 4.0, respectively.

8.1.3 Experimental Study of the Exchange Process Between the Main Flow and its Side Basin

The transverse exchanges of mass between an open-channel main flow and an array of side basins are studied in the laboratory using a red dye as the tracer. A video imaging method is employed to measure the dye concentration. The accumulation and retention times of the dye in the side basins are determined as the parameters to characterize the exchanges. The mixing and exchange processes across these shear flows at high Froude number are critically dependent on the energy dissipation across the shock waves and the

radiation of energy from the waves. The energetic radiation of the gravity waves in the supercritical flow does not lead to vigorous exchanges. On the contrary, the dimensionless retention time for the supercritical flow at high Froude number is three to four times greater than the retention time for the subcritical flow.

8.1.4 Numerical Simulations of Macro Resistance in Steep Open Channels and Meandering Channels

The resistance to flow due to macro roughness on steep open-channel flow is calculated directly from numerical simulation by MIS2D model. A series of calculations has been carried out for several channel geometries including the flow through the meandering river and flow through obstacles. The flow around the macro roughness is turbulent and dependent on wave radiation from the turbulent flow. The overall macro roughness coefficient is determined from the simulations. The overall flow resistance includes both the channel bottom friction and the form drag. The friction is described by the conventional Manning formula and the form drag is described by the drag coefficient.

8.2 Contribution to Knowledge

The research has advanced knowledge of the wave effects on the shear instability and its transition to turbulence for the flow in shallow flows. A comprehensive study of the trans-critical and supercritical instabilities in comparison with the sub-critical flows are conducted. A generalized convective Froude number is introduced to parameterize the wave effects. In the jet/wake instability problem, the convective Froude number defines stability for both sinuous and varicose modes of oscillations. The co-existence of modes and the switching from the varicose to sinuous mode described by the direct numerical simulation is a problem beyond the classical description by the normal mode. Convergence study has shown the numerical simulations to have better than one percent of accuracy. The analysis of non-linear stage of the jet/wake development evaluates the velocity fluctuation, mean velocity profile, total energy and half width, and correlates these variables with convective Froude

number. The correlation shows the existence of the subcritical range, trans-critical range and supercritical range of the flow. In the experiments to study the exchange process, the generation of waves is observed in the laboratory at Froude number greater than the unity. Friction effect has been included as an addition to the wave effects in the simulations of macro roughness in open channel flow. Manning coefficient of friction often used in engineering practice in one dimensional formulation is found to underestimate the flow resistance as the wave drag is not generally negligible in meandering river channels. Waves produces by the blockage of rocks and gravels can also contribute significantly the overall resistance in channel flow on steep slope. The various aspects of the wave effects examined in this thesis are elements needed for the development of a comprehensive theory of turbulence for the trans-critical and supercritical flow in shallow flows.

REFERENCES

[1] V. Alavian and V.H. Chu. Turbulent exchange flow in shallow compound channel. In *Proceedings of the 21st International Congress of IAHR, Melbourne*, pages 446–451, 1985.

[2] W. Altai and V.H. Chu. Retention time in recirculating flow. In *Proceedings of the 27th IAHR Congress*, San Francisco, USA, 1997.

[3] G. J. Arcement and V.R. Schneider. *Guide for selecting Manning's roughness coefficients for natural channels and flood plains*. US Government Printing Office Washington, DC, USA, 1989.

[4] E.J. Avital, N.D. Sandham, and K.H. Luo. Mach wave radiation by mixing layers. part i: Analysis of the sound field. *Theoretical and Computational Fluid Dynamics*, 12(2):73–90, 1998.

[5] S. Babarutsi and V.H. Chu. Dye-concentration distribution in shallow recirculating flows. *Journal of Hydraulic Engineering*, 117(5):643–659, 1991.

[6] R. Balachandar, S. Ramachandran, and M.F. Tachie. Characteristics of shallow turbulent near wakes at low reynolds numbers. *Journal of fluids engineering*, 122(2):302–308, 2000.

[7] N.J. Balmforth and C. Piccolo. The onset of meandering in a barotropic jet. *Journal of Fluid Mechanics*, 449:85–114, 2001.

[8] R. Betchov and W.O. Criminale Jr. Spatial instability of the inviscid jet and wake. *Physics of Fluids (1958-1988)*, 9(2):359–362, 1966.

[9] D.W. Bogdanoff. Compressibility effects in turbulent shear layers. *AIAA journal*, 21(6):926–927, 1983.

[10] R. Booij. Exchange of mass in harbours. In *Proceedings of the 23rd IAHR Congress*, Ottawa, Canada, 1989.

[11] F. Bouchut, B. Ribstein, and V. Zeitlin. Inertial, barotropic, and baroclinic instabilities of the bickley jet in two-layer rotating shallow water model. *Physics of Fluids (1994-present)*, 23(12):126601, 2011.

[12] S. Bouhairie and V. H. Chu. Heated wake by deferred corrected ultra. In *Computational Fluid Dynamics 2006*, pages 291–296. Springer, 2009.

[13] P. Bradshaw. Compressible turbulent shear layers. *Annual Review of Fluid Mechanics*, 9(1):33–52, 1977.

[14] G. L. Brown and A. Roshko. On density effects and large structure in turbulent mixing layers. *Journal of Fluid Mechanics*, 64(04):775–816, 1974.

[15] G.F. Carrier and H.P. Greenspan. Water waves of finite amplitude on a sloping beach. *Journal of Fluid Mechanics*, 4(01):97–109, 1958.

[16] U. Celik, I. B. Ghia, P. J. Roache, et al. Procedure for estimation and reporting of uncertainty due to discretization in cfd applications. *Journal of fluids Engineering-Transactions of the ASME*, 130(7), 2008.

[17] Pao Y.H. Champagne, F.H. and I.J. Wygnanski. On the two-dimensional mixing region. *Journal of Fluid Mechanics*, 74(02):209–250, 1976.

[18] J. H. Chen, B. J. Cantwell, and N. N. Mansour. Direct numerical simulations of a plane compressible wake: Stability, vorticity dynamics, and topology. Technical report, Stanford Univ., CA (USA). Thermosciences Div., 1989.

[19] J. H. Chen, B. J. Cantwell, and N. N. Mansour. The effect of mach number on the stability of a plane supersonic wake. *Physics of Fluids A: Fluid Dynamics (1989-1993)*, 2(6):984–1004, 1990.

[20] V. H. Chu. Turbulent transport processes across natural streams. *Environmental Fluid Mechanics–Theories and Applications*, pages 127–167, 2002.

[21] V. H. Chu. Instabilities in non-rotating and rotating shallow shear flows. *Environmental Fluid Mechanics*, pages 1–19, 2014.

[22] V. H. Chu, J. H. Wu, and R. E. Khayat. Stability of transverse shear flows in shallow open channels. *Journal of Hydraulic Engineering*, 117(10):1370–1388, 1991.

[23] V.H. Chu. Shear instability, wave and turbulence simulations using the shallow-water equations. *Journal of Hydro-environment Research*, 3(4):173–178, 2010.

[24] G. Constantinescu, A. Sukhodolov, and A. McCoy. Mass exchange in a shallow channel flow with a series of groynes: Les study and comparison with laboratory and field experiments. *Environmental Fluid Mechanics*, 9(6):587–615, 2009.

[25] E. Dick. Introduction to finite volume methods in computational fluid dynamics. von karman institute lecture series, vki, sint-genesius-rode, 2000, 29 pp.

[26] N. Dodd. Numerical model of wave run-up, overtopping, and regeneration. *Journal of Waterway, Port, Coastal, and Ocean Engineering*, 124(2):73–81, 1998.

[27] T.H. Dracos, M. Giger, and G.H. Jirka. Plane turbulent jets in a bounded fluid layer. *Journal of Fluid Mechanics*, 241:587–614, 1992.

[28] L. F. East. Aerodynamically induced resonance in rectangular cavities. *Journal of Sound and Vibration*, 3(3):277–287, 1966.

[29] G.S. Elliott and M. Samimy. Compressibility effects in free shear layers. *Physics of Fluids A: Fluid Dynamics (1989-1993)*, 2(7):1231–1240, 1990.

[30] N. Forestier, L. Jacquin, and P. Geffroy. The mixing layer over a deep cavity at high-subsonic speed. *Journal of Fluid Mechanics*, 475(1):101–145, 2003.

[31] R. H. French. Open-channel hydraulics. 1985.

[32] J.B. Freund, S.K. Lele, and P. Moin. Numerical simulation of a mach 1.92 turbulent jet and its sound field. *AIAA journal*, 38(11):2023–2031, 2000.

[33] S.K. Ghannadi. *Numerical Simulations of Subcritical and Supercritical Flows in Shallow Waters*. PhD thesis, McGill University, 2015.

[34] M.S. Ghidaoui and A.A. Kolyshkin. Linear stability analysis of lateral motions in compound open channels. *Journal of Hydraulic Engineering*, 125(8):871–880, 1999.

[35] M. Giger, T. Dracos, and G.H. Jirka. Entrainment and mixing in plane turbulent jets in shallow water. *Journal of hydraulic research*, 29(5):615–642, 1991.

[36] S.K. Godunov. Reminiscences about numerical schemes. *arXiv preprint arXiv:0810.0649*, 2008.

[37] V. Guinot. *Godunov-type schemes: an introduction for engineers*. Elsevier, 2003.

[38] A. Harten, B. Engquist, S. Osher, and S. R. Chakravarthy. Uniformly high order accurate essentially non-oscillatory schemes, III. *Journal of Computational Physics*, 71(2):231–303, 1987.

[39] F.M. Henderson. Open channel flow. *MacMi1lan, New York*, 1966.

[40] C.W. Hirt. Flow-3d user manual version 10. *Flow Science*, 2011.

[41] G. Jiang and C. W. Shu. Efficient implementation of weighted eno schemes. *Journal OF Computational Physics*, 126:202–228, 1996.

[42] G.H. Jirka. Shallow jets. In *Recent Research Advances in the Fluid Mechanics of Turbulent Jets and Plumes*, pages 155–175. Springer, 1994.

[43] S. Karimpour and V.H. Chu. High-order interpolation schemes for shear instability simulations. *International Journal for Numerical Methods for Heat and Fluid Flow*, 2015.

[44] C. A. Kennedy and J. H. Chen. Mean flow effects on the linear stability of compressible planar jets. *Physics of Fluids (1994-present)*, 10(3):615–626, 1998.

[45] S.C. Kim. New mixing-length model for supersonic shear layers. *AIAA journal*, 28(11):1999–2000, 1990.

[46] D.W. Knight and K. Shiono. Turbulence measurements in a shear layer region of a compound channel. *Journal of Hydraulic Research*, 28(2):175–196, 1990.

[47] A.A. Kolyshkin and M.S. Ghidaoui. Gravitational and shear instabilities in compound and composite channels. *Journal of Hydraulic Engineering*, 128(12):1076–1086, 2002.

[48] M.F. Lambert and R.H.J. Sellin. Discharge prediction in straight compound channels using the mixing length concept. *Journal of Hydraulic Research*, 34(3):381–394, 1996.

[49] S. Lee, S. K. Lele, and P. Moin. Eddy shocklets in decaying compressible turbulence. *Physics of Fluids A: Fluid Dynamics (1989-1993)*, 3(4):657–664, 1991.

[50] B. P. Leonard. A stable and accurate convective modelling procedure based on quadratic upstream interpolation. *Computer methods in applied mechanics and engineering*, 19(1):59–98, 1979.

[51] B.P. Leonard. The quick algorithm-a uniformly third-order finite-difference method for highly convective flows. *Computer methods in fluids*, 1:159–195, 1980.

[52] B.P. Leonard. Simple high-accuracy resolution program for convective modelling of discontinuities. *International Journal for Numerical Methods in Fluids*, 8(10):1291–1318, 1988.

[53] B.P. Leonard and S. Mokhtari. Ultra-sharp nonoscillatory convection schemes for high-speed steady multidimensional flow. 1990.

[54] M. Lessen, J.A. Fox, and H.M. Zien. On the inviscid stability of the laminar mixing of two parallel streams of a compressible fluid. *Journal of Fluid Mechanics*, 23(02):355–367, 1965.

[55] R.J. LeVeque. *Finite volume methods for hyperbolic problems*, volume 31. Cambridge university press, 2002.

[56] J.A. Liggett. Fluid mechanics, 495 pp, 1994.

[57] C.C. Lin. On the stability of the laminar mixing region between two parallel streams in a gas. Technical report, DTIC Document, 1953.

[58] L.M. Mack. On the inviscid acoustic-mode instability of supersonic shear flows. *Theoretical and Computational Fluid Dynamics*, 2(2):97–123, 1990.

[59] S. A. Maslowe. Barotropic instability of the bickley jet. *Journal of Fluid Mechanics*, 229:417–426, 1991.

[60] A. McCoy, G. Constantinescu, and L. Weber. A numerical investigation of coherent structures and mass exchange processes in channel flow with two lateral submerged groynes. *Water Resources Research*, 43(5):5445, 2007.

[61] A. Michalke. On spatially growing disturbances in an inviscid shear layer. *Journal of Fluid Mechanics*, 23(03):521–544, 1965.

[62] C. Pantano and S. Sarkar. A study of compressibility effects in the high-speed turbulent shear layer using direct simulation. *Journal of Fluid Mechanics*, 451:329–371, 2002.

[63] D. Papamoschou and A. Roshko. The compressible turbulent shear layer: an experimental study. *Journal of Fluid Mechanics*, 197:453–477, 1988.

[64] D. Papamoschou and A. Roshko. Observations of supersonic free shear layers. *Sadhana*, 12(1-2):1–14, 1988.

[65] Y. Peltier, S. Erpicum, P. Archambeau, M. Pirotton, and B. Dewals. Experimental investigation of meandering jets in shallow reservoirs. *Environmental Fluid Mechanics*, 14(3):699–710, 2014.

[66] C. E. Pinilla, S. Bouhairie, L-W. Tan, and V.H. Chu. Minimal intervention to simulations of shallow-water equations. *Journal of Hydro-environment Research*, 3(4):201–207, 2010.

[67] C. E. Pinilla and V. H. Chu. Waves and bed-friction effect on stability of transverse sheer flow in shallow waters. *Journal of Coastal Research*, pages 207–214, 2008.

[68] C. E. Pinilla and V. H. Chu. The role of wave radiation on instability of coastal current. In *Proc. 33rd Congress of IAHR, ISBN*, pages 978–90, 2009.

[69] C. E. Pinilla and V. H. Chu. Wave radiation and shear instability in rotating stratified flow. In *ASME 2009 28th International Conference on Ocean, Offshore and Arctic Engineering*, pages 425–432. American Society of Mechanical Engineers, 2009.

[70] P. K. Ray, L. C. Cheung, and S. K. Lele. On the growth and propagation of linear instability waves in compressible turbulent jets. *Physics of Fluids (1994-present)*, 21(5):054106, 2009.

[71] W. Rodi. *Turbulence models and their application in hydraulics*. CRC Press, 1993.

[72] P. L. Roe. Approximate riemann solvers, parameter vectors, and difference schemes. *Journal of computational physics*, 43(2):357–372, 1981.

[73] J. E. Rossiter. Wind-tunnel experiments on the flow over rectangular cavities at subsonic and transonic speeds. Reports and Memoranda 3438, Ministry of Aviation, 1964.

[74] T. Rossmann, M. G. Mungal, and R. K. Hanson. Evolution and growth of large-scale structures in high compressibility mixing layers. *J. Turbulence*, 3(009):1–19, 2002.

[75] N.D. Sandham and W.C. Reynolds. Compressible mixing layer-linear theory and direct simulation. *AIAA journal*, 28(4):618–624, 1990.

[76] N.D. Sandham and W.C. Reynolds. Three-dimensional simulations of large eddies in the compressible mixing layer. *Journal of Fluid Mechanics*, 224:133–158, 1991.

[77] M.C. Shen and R.E. Meyer. Climb of a bore on a beach part 3. run-up. *Journal of Fluid Mechanics*, 16(01):113–125, 1963.

[78] C. W. Shu. Essentially non-oscillatory and weighted essentially non-oscillatory schemes for hyperbolic conservation laws. In *Advanced Numerical Approximation of Nonlinear Hyperbolic Equations*, pages 325–432, 1998. Lecture Notes in Mathematics.

[79] C. W. Shu. High order weighted essentially nonoscillatory schemes for convection dominated problems. *SIAM Review*, 51(1):82–126, 2009.

[80] G.S. Stelling and S.P.A. Duinmeijer. A staggered conservative scheme for every froude number in rapidly varied shallow water flows. *International journal for numerical methods in fluids*, 43(12):1329–1354, 2003.

[81] F. Stern, R. V. Wilson, H. W. Coleman, and E. G. Paterson. Comprehensive approach to verification and validation of cfd simulationspart 1: methodology and procedures. *Journal of fluids engineering*, 123(4):793–802, 2001.

[82] J.J. Stoker. Water waves, pure and applied mathematics, 1957.

[83] C. K. W. Tam and P. J. W. Block. On the tones and pressure oscillations induced by flow over rectangular cavities. *Journal of Fluid Mechanics*, 89(2):373–399, 1978.

[84] N. Tamai, T. Asaeda, and H. Ikeda. Study on generation of periodical large surface eddies in a composite channel flow. *Water Resources Research*, 22(7):1129–1138, 1986.

[85] E. F. Toro. Riemann solvers and numerical methods for fluid dynamics. 1999.

[86] W. S. J. Uijttewaal, D. Lehmann, and A. Mazijk. Exchange processes between a river and its groyne fields: Model experiments. *Journal of Hydraulic Engineering*, 127(11):928–936, 2001.

[87] W.S.J. Uijttewaal and R. Booij. Effects of shallowness on the development of free-surface mixing layers. *Physics of Fluids (1994-present)*, 12(2):392–402, 2000.

[88] B. Van Leer. Towards the ultimate conservative difference scheme. v. a second-order sequel to godunov's method. *Journal of computational Physics*, 32(1):101–136, 1979.

[89] B. C. Van Prooijen, J. A. Battjes, and W. S.J. Uijttewaal. Momentum exchange in straight uniform compound channel flow. *Journal of Hydraulic Engineering*, 2005.

[90] T.C. Ven. Open channel hydraulics. 1959.

[91] A.W. Vreman, N.D. Sandham, and K.H. Luo. Compressible mixing layer growth rate and turbulence characteristics. *Journal of Fluid Mechanics*, 320:235–258, 1996.

[92] T. Wang and V.H. Chu. Manning friction in steep open-channel flow. *Proceedings of The Seventh International Conference on Computational Fluid Dynamics,Big Island, Hawaii,USA*, 2012.

[93] T. Wang and V.H. Chu. Instabilities and nonlinear transition of high-speed shear flow in shallow waters. *Proceedings of The Eighth International Conference on Computational Fluid Dynamics,Chengdu,China*, 2014.

[94] T. Wang, S. Karimpour-Ghannadi, and V. H. Chu. Retention of dye tracer in side basins exchanging with subcritical and supercritical flows. In *River Flow*, volume 2, pages 1775–1782, 2010.

[95] T. Wang, L.W. Tan, and V.H. Chu. Flood-waves simulation by classical method of consistent transport. In *Computational Fluid Dynamics 2010*, pages 287–293. Springer, 2011.

[96] V. Weitbrecht, G. Kühn, and G. H. Jirka. Large scale piv-measurements at the surface of shallow water flows. *Flow Measurement and Instrumentation*, 13(5):237–245, 2002.

[97] V. Weitbrecht, S. A. Socolofsky, and G. H. Jirka. Experiments on mass exchange between groin fields and main stream in rivers. *Journal of Hydraulic Engineering*, 134(2):173–183, 2008.

[98] X. Wu. Mach wave radiation of nonlinearly evolving supersonic instability modes in shear layers. *Journal of Fluid Mechanics*, 523:121–159, 2005.

[99] I. Wygnanski and H.E. Fiedler. The two-dimensional mixing region. *Journal of Fluid Mechanics*, 41(02):327–361, 1970.

[100] G. S. Young and J. Zawislak. An observational study of vortex spacing in island wake vortex streets. *Monthly weather review*, 134(8):2285–2294, 2006.

[101] J.B. Zhang and V.H. Chu. Shallow turbulent flows by video imaging method. *Journal of Engineering Mechanics*, 129(10):1164–1172, 2003.